SPATIAL AND TEMPORAL ANALYSIS OF EVAPOTRANSPIRATION USING SEBAL MODEL IN THE DATA SCARCE MOJO CATCHMENT, ETHIOPIA

MSC THESIS

HIRUT GIRMA

HAWASSA UNIVERSITY

INSTITUTE OF TECHNOLOGY

FEBRUARY, 2024

SPATIAL AND TEMPORAL ANALYSIS OF EVAPOTRANSPIRATION USING SEBAL MODEL IN THE DATA SCARCE MOJO CATCHMENT, ETHIOPIA

HIRUT GIRMA

MAJOR ADVISOR: NIGATU WONDRAD (PhD)

CO-ADVISOR: ABRAHAM WELDEMICHAEL (PhD)

A THESIS SUBMITTED TO DEPARTMENT OF WATER RESOURCE AND IRRIGATION ENGINEERING

HAWASSA UNIVERSITY

INSTITUTE OF TECHNOLOGY

IN PARTIAL FULFILLMENT OF THE REQUIREMENTS FOR THE DEGREE OF MASTER OF SCIENCE IN IRRIGATION AND DRAINAGE ENGINEERING

FEBRUARY, 2024

DECLARATION

I declare that this research thesis entitled ‘‘Spatial and temporal analysis of evapotranspiration using SEBAL model in the data scarce Mojo catchment, Ethiopia’’ is my own work and has not been submitted to any university for similar purpose, The reference used in this research are recognized by proper citation.

Hirut Girma ______________ ________________

Name of student Signature Date

ADVISOR APPROVAL SHEET

OF THE MSc THESIS HAWASSA UNIVERSITY

This is to certify that the thesis entitled with “Spatial and temporal analysis of evapotranspiration using SEBAL model in the data scarce Mojo catchment, Ethiopia” submitted in partial fulfillment of the requirement for the degree of Masters with specialization in Irrigation and Drainage Engineering, the graduate program of the department of Water Resource and Irrigation Engineering, and has carried out by Hirut Girma, Id. No GpIrDrR/0004/14, under my supervision. Therefore, we recommend that the student has fulfilled the requirement and hence hereby can submit the thesis to the department for defense.

Nigatu Wondrad (PhD)	________________	_________
Name of major advisor	Signature	Date
Abraham Weldemichael (PhD)	________________	__________
Name of Co-advisor	Signature	Date

EXAMINERS APPROVAL SHEET

OF THE MSc THESIS HAWASSA UNIVERSITY

As members of the Examining Board of the Final MSc Open Defense, we certify that we have read and evaluated the thesis prepared by Hirut Girma entitled “Spatial and temporal analysis of evapotranspiration using SEBAL model in the data scarce Mojo catchment, Ethiopia” and examined the candidate. This is, therefore, to certify that the thesis has been accepted in partial fulfillment of the requirements for the degree.

____________________________	__________	_____________
Name of Chairman	Signature	Date
____________________________	__________	_____________
Name of Major Advisor	Signature	Date
____________________________	__________	_____________
Name of Internal Examiner	Signature	Date
____________________________	__________	_____________
Name of External Examiner	Signature	Date
____________________________	__________	_____________
SGS Approval	Signature	Date

ACKNOWLEDGEMENTS

I thank all who in my way in completion of this thesis, First, I thank the Almighty God for his courage and grace upon me during my study period and all in my life. I would like to acknowledge give my warmest thanks to my supervisor Dr. Nigatu Wondirad (PhD) and Dr. Abraham Woldemikael (PhD) who made this work possible. Their guidance and advice carried me through all the stage of writing my thesis.

I gratefully acknowledge Ethiopian National Meteorological Agency (ENMA) for providing weather data. My sincere gratitude goes to Tewodros Kassaye from Bahr dar, Ethiopia for his effort and support during the SEBAL model setup and I would like to thank my friend Aschenaki Mekonnen for helping me by professional support, and abundant comments on this work. Also I would like to express my sincere appreciation to my families especially my mother, Mrs. Etagegnehu Tilahun.

Finally, I am very grateful to all those who helped me either materially or through advice during the study.

Contents

DECLARATION ii
ADVISOR APPROVAL SHEET iii
EXAMINERS APPROVAL SHEET........ iv
ACKNOWLEDGEMENTS........ v
LIST OF TABLES........ x
LIST OF FIGURES xi
LIST OF FIGURES IN APPENDICES........ xii
LIST OF TABLES IN APPENDICES xiii
LIST OF ABBREVATIONS & ACRONYMS xiv
ABSTRACT........ xvi
INTRODUCTION 1
1.1 Background 1
1.2 Statement of the Problem 3
1.3 OBJECTIVES 4
1.3.1 General objective........ 4
1.3.2 Specific objectives........ 4
1.4 Research Questions 4
2. LITERATURE REVIEW 5
2.1 Background 5
2.2 Evapotranspiration (ET)........ 5
2.2.1 Evapotranspiration assessment techniques at different scales of observation........ 6
2.3 Reference evapotranspiration (ETo) 7
2.4 Remote sensing application in water balance study........ 7
2.5 Land use land cover 8
2.6 Surface Energy Balance models........ 9
2.6.1 Surface Balance Energy System (SEBS) 9
2.6.2 Simplified Surface Energy Balance Operational (SSEBop) 10
2.6.3 simplified surface energy balance index (SS-SEBI) 10
2.6.4 Mapping Evapotranspiration at high Resolution with Internalized Calibration (METRIC) 10

2.6.5 Surface Energy Balance Algorithm for Land (SEBAL).. 11
2.6.6 Two-Source Models (TSM) 13
2.7 Digital Elevation Model (DEM) Application in hydrology.. 15
2.8 Ground based empirical method of estimating Evapotranspiration............................... 15
2.8.1 Penman-Monteith equation 16
2.8.2 Hargreaves method.. 17
2.8.3 Blaney-Criddle method 17
2.8.4 Thornthwaite method.. 18
2.8.5 FAO-56 Method 18
2.8.6 Priestley-Taylor Method.. 19
2.9 Reference Evapotranspiration (REF-ET)... 19
3. MATERIALS AND METHODS.. 20
3.1 Description of Study Area... 20
3.1.1 Location of study area 20
3.1.2 Soil of the area... 21
3.1.3 Climate of study area.. 21
3.1.4 Topography... 21
3.2 Data collection and preparation 22
3.2.1 ASTER Global Digital Elevation Model... 23
3.2.2 Satellite images data 23
3.2.3 Meteorological data and ground observation data... 24
3.4 Land use land covers classification.. 25
3.4.1 Supervised classification 25
3.4.2 Accuracy assessment for the classified images and calculating Kappa Statistics.... 26
One of the most common means of expressing 3.3 Research design flow chart................. 26
3.5 software packages used for SEBAL model... 27
3.5.1 Geographic Resources Analysis Support System (GRASS GIS)............................ 27
3.6 Surface Energy Balance Algorithm for Land (SEBAL) model 28
3.6.1 Calculation of Surface Radiation elements 29
3.6.2 Vegetation indices 30

3.6.3 Emissivity and land surface temperature 31
3.6.4 Calculation of Solar Radiations Elements and ET 32
3.6.5 Calculation of surface energy budget elements 33
3.7 24-Hour Evapotranspiration (ET24) in SEBAL 36
3.8 Ground based ET calculation 36
3.8.1 REF-ET 37
3.9 Model Comparison and calibration 37
3.9.2 Model calibration 37
3.9 Research design flow chart 38
4. RESULTS AND DISCUSION 40
4.1 Land use land cover (LULC) maps 40
4.1.2 Accuracy assessment for the land use land cover map 41
4.2 Reference evapotranspiration ETr 42
4.2.1 Instantaneous wind speed and ETr calculation 42
4.3 Surface radiation balance 45
4.3.1 Surface albedo 45
4.3.2 Incoming short wave radiation 46
4.3.3 Outgoing longwave radiation 47
4.3.4 incoming long wave radiation (RLI) 49
4.3.5 Net surface radiation 51
4.4 Vegetation indices 52
4.4.1 Normalized difference vegetation index (NDVI) 52
4.4.2 Soil Adjusted Vegetation Index (SAVI) 54
4.4.3 Leave Area Index (LAI) 55
4.5 Surface temperature (TS) 56
4.6 Surface energy balance 58
4.6.1 Soil heat flux (G) 58
4.6.2 Sensible heat flux (H) 59
4.6.3 Latent heat flux (LET) 60
4.7 Instantaneous ET (ETins) and reference ET fraction (ETrF) 62

4.8 24-Hour Evapotranspiration (ET24) 63
4.8.1 Daily Evapotranspiration 64
4.9 Seasonal evapotranspiration 66
4.10 Comparison of ground based evapotranspiration estimation method with SEBAL 67
4.10.1 Comparisons based on Root Mean Square Error 69
4.11 Model Calibration 69
5. CONCLUSIONS AND RECOMENDATIONS 71
5.1 Conclusion 71
5.2 Recommendation 73
6. REFERENCE 74
7. APPENDICES 82

LIST OF TABLES

Table 2. 1 Comparisons of the different remote sensing ET models....................................... 14

Table 3. 1 Sentinel image data characterstics……………………...……………………...**23**
Table 3. 2 Description of the Landsat 8 images used to implement the (SEBAL)....................... 24
Table 3. 3 Sample Meteorological data for 24 January from 2022G.C.. 25
Table 3. 4 Different software with their description and the use for the paper 28
Table 4. 1 Error matrix for LULC in the Mojo Catchment, for the 2022 period……...............41
Table 4. 2 Calculation of Satellite overpass time in local standard time.................................. 42
Table 4. 3 Calculated of reference evapotranspiration, instantaneous evapotranspiration and wind speed values. .... …44
Table 4. 4 Comparison of Eta in SEBAL model and reference evapotranspiration................. 67

LIST OF FIGURES

Figure 3. 1 Location map of the study area 20
Figure 3. 2 Slope map of mojo catchment 22
Figure 3. 3 The conceptual scheme for the research design 39
Figure 3. 4 General schematization of land use land cover classification 26
Figure 4. 1 Land use and land cover map of the Mojo catchment for the 2022 period……….40
Figure 4. 2 Map of surface albedo .... …………….45
Figure 4. 3 Map of incoming short wave radiation........ 47
Figure 4. 4 Map of outgoing longwave radiation 48
Figure 4. 5 Map of Incoming longwave radiation 50
Figure 4. 6 Map of Net Radiation 51
Figure 4. 7 Map of NDVI 53
Figure 4. 8 Map of SAVI 54
Figure 4. 9 Map of LAI........ 56
Figure 4. 10 map of surface temperature 57
Figure 4. 11 Map of soil heat flux 58
Figure 4. 12 Map of Sensible heat flux........ 60
Figure 4. 13 Map of Latent heat flux 61
Figure 4. 14 Map of instantanious Evapotranspiration........ 62
Figure 4. 15 Map of Reference ET Fraction 63
Figure 4. 16 Map of Spatial–temporal distribution of mean daily AET 65
Figure 4. 17 Mean daily AET in the Mojo catchment for different land use types 66
Figure 4. 18 The cumulative map of ET for the selected period (Oct to Mar 2022) of mojo catchment. 67
Figure 4. 19 Caparison of Eta in SEBAL and reference evapotranspiration 68
Figure 4. 20 The scatter plot of ETo with AET of the catchment at daily basis 70

LIST OF FIGURES IN APPENDICES

Image 7. 1 Interface of REF-ET software 83
Image 7. 2Sample Output of ref- et software 84
Image 7. 3Albedo value for deferent land use feature in a given six month (October-march) 88
Image 7. 4 Incoming short wave radiation value for deferent land use feature in a given six month (October-march) 88
Image 7. 5 Outgoing long wave radiation value for deferent land use feature in a given six month (October-march) 89
Image 7. 6 Normalize difference vegetable index value for deferent land use feature in a given six month (October-march) 89
Image 7. 7SAVI Value for deferent land use feature in a given six month (October-march) .. 90
Image 7. 8 LAI value for different land use feature for mojo catchment for the period of 2022 (October- March) 90
Image 7. 9 Surface temperature Value for deferent land use feature in a given six month (October-march) 91
Image 7. 10 Incoming longwave radiation Value for deferent land use feature in a given six month (October-march) 92
Image 7. 11 Net Radiation Value for deferent land use feature in a given six month (October-march) 92
Image 7. 12 Ground heat flux Value for deferent land use feature in a given six month (October-march) 93
Image 7. 13 Sensible heat flux value for deferent land use feature in a given six month (October-march) 93
Image 7. 14 Latent heat flux value for deferent land use feature in a given six month (October-march) 94
Image 7. 15 Monthly AET spatial-temporal distribution of 2022 over mojo catchment 95

LIST OF TABLES IN APPENDICES

Table7. 1 Sample Meteorological data forone day in 24 January from 2022 82
Table7. 2 Calclation of satellite overpass time, instantanious evapotranspiration, and windspped 86
Table7. 3 Mean monthly ETa spatial-temporal distribution of 2022 over mojo catchment..... 95
Table7. 4 Values obtained from SEBAL model of the mojo catchment in 2022 96

LIST OF ABBREVATIONS & ACRONYMS

AWS	Automatic Weather Station
DEM	Digital Elevation Model
DN	Digital Numbers
ET	Evapotranspiration
ETa	Actual Evapotranspiration
ETo	Reference Evapotranspiration
FAO	Food and Agricultural Organization
GIS	Geographic Information System
GRASS	Geographic Reference Analysis Support System
LAI	Leaf Area Index
LULC	Land Use Land Cover
METRIC	Mapping ET with high Resolution with Internalized Calibration
ML	Maximum Likelihood
MODIS	Moderate Resolution Imaging Spectro-radiometer
MTSAT	Multi-Functional Transport Satellite
NASA	National Aeronautics and Space Administration
NDVI	Normalized Difference Vegetation Index
NIR	Near Infrared
NMA	National Meteorological Agency
OLI	Operational Land Imager
QGIS	Quantum Geographical information system
RE	Relative Error
RLI	Incoming Longwave Radiation
RLO	Outgoing Longwave Radiation
RN	Net Radiation
RMSE	Root Mean Square Error
RS	Remote Sensing
RSI	Incoming Shortwave Radiation

SAVI	Soil Adjusted Vegetation Index
SEBAL	Surface Energy Balance Algorithm for Land
SRTM	Shuttle Radar Topographic Mission
S-SEBI	Simplified Surface Energy Balance Index
SSEBop	Operational Simplified Surface Energy Balance
TIRS	Thermal Infrared Sensor
TS	Surface Temprature
UTM	Universal Transverse Mercator
VIS	Visible bands
WGS	World Geodetic system
WMO	World Meteorological Organization

ABSTRACT

Evapotranspiration is essential to the hydrological and energy cycles, as well as to the estimation of irrigation needs and water supplies. For improved water resource planning and management, accurate ET estimation is crucial to the measurement of the water balance at the basin, river basin, and regional scales. Remotely sensed data are good alternatives that support the collection of climate data. The objective of this study was to estimate *Spatial and temporal analysis of evapotranspiration using* surface *energy balance algorithm for the land* (*SEBAL) model in the data scarce Mojo catchment*. *This study used the SEBAL model to assess satellite evapotranspiration from October to March 2022. For this analysis, net radiation, soil heat flow, sensible heat flux, latent heat flux, surface emissivity, surface temperature, surface radiance, surface reflectance, surface albedo, NDVI, and LAI are calculated. The sensible heat flux is calculated by determining the hot and cold pixels under consideration via the atmospheric stability conditions. Finally, evapotranspiration maps are plotted. Consequently, GRASS GIS software and SEBAL Python were used to determine the daily, monthly, and seasonal evapotranspiration in the research area. The findings demonstrated a good degree of agreement between the evapotranspiration values provided by SEBAL and the FAO Penman-Monteith method, with the latter reporting the lowest error (RMSE = 1.14) and the highest correlation (R^2 = 0.96). The estimated ET values for the months of March through October, In March and November, the highest and lowest calculated AET values were 6.43 and 4.2 mm/d, respectively. ET values were computed for emperical methods using REF-ET software. In order to compare the results obtained from the SEBAL approach, the Standard Penman-Monteith value for the weather station was utilized as a reference. The results indicate that, given the SEBAL algorithm's acceptable performance in estimating actual evapotranspiration using Landsat 8 satellite images, it could be a very practical method and play a crucial role in understanding water resource management on various earthly surfaces, which is necessary to achieve sustainable development of water resources in the basin. It is also advised that the SEBAL algorithm be applied in the upper Awash basin's remaining catchment.*

Keywords: Evapotranspiration, GRASS GIS, Mojo Catchment, REF-ET, Remote Sensing, SEBAL.

INTRODUCTION

1.1 Background

Evapotranspiration (ET) plays a crucial role in hydrological and energy cycles, as well as in the assessments of water resources and irrigation demands (Shamloo, Sattari, et al., 2021). It is the second largest term after precipitation in the global terrestrial water. The term evapotranspiration is a combination of evaporation from soil surface and transpiration from plant. It plays a significant role in the water, energy, and carbon cycles on earth as well as the heat and water balance of terrestrial ecosystems. In essence, the reference evapotranspiration (ETo) is determined empirically by utilizing a lysimeter to simplify the water budget equation, or it is computed using standard methods such as the FAO Penman-Monteith, Thornthwaite, Blaney-Criddle, and Hargreaves methods.

A number of techniques have been developed for estimating evapotranspiration, such as empirical equations and direct/field observations. However, ET consists of a complex and nonlinear structure requiring multiple parameters for estimation. This nonlinear and multi-parameter nature makes estimation methods tedious and time-consuming. Even if accurate ET estimates can be obtained for the instrumented sites, these values are not useful at larger scales due to the usual heterogeneity of the landscape and the complexity of the hydrological processes. The meteorological observations do not provide true spatial evapotranspiration of an area (Liu et al., 2011).

Good knowledge of ET can improve the water resources management at different scales; in particular, detailed ET estimations in agricultural areas can improve detection of water stress and help in the irrigation scheduling (French et al., 2015). ET is important in predicting soil water availability, flood forecasting, rainfall forecasting, and projecting changes in occurring heat waves and droughts (Chirouze et al., 2014). Accurate estimation of ET plays an important role in the quantification of the water balance at the level of basin, river basin, and regional scale for better planning and management of water resources. Accurate quantification of ET in irrigated agriculture is crucial to optimize crop production, water distribution planning, irrigation management, assessment of the effects of land-use change on water yields, and assessment of land use and practices of water resources management and environmental quality (Irmak et al., 2007).

In the future, if there is no proper water resources management in the sub basin, demands will outstrip supplies, resources will become scarce and environmental or ecological issues will get serious. Therefore, optimum utilization of the scarce water resource can be made possible through comprehensive study of the temporal and spatial availability of the resource. In order to quantify the resource accurately, quality data should be available (Atanaw, 2009). There are some meteorological and hydrological stations in the catchment; however there exists a lot of missing data in the recorded data sets. Therefore, data acquisition has to be supported by remotely sensed data to fill the gap and assessing the water resources availability could be possible with greater certainty.

Evapotranspiration models based on remote sensing provide relatively accurate estimations of evapotranspiration in large areas with minimal use of terrestrial data (Bastiaanssen et al., 2005). With the use of remote sensing, it is possible to directly derive the water consumed as ET without the need to quantify other complex hydrological processes (Trezza et al., 2013). These techniques allow for filling in the gap in providing the much-needed spatially observed data (Rawat et al., 2019). The advancements in remote sensing techniques in recent years together with the accessibility to satellite images have allowed for alternative and reliable methods for evapotranspiration estimations at regional scales (Mao and Wang 2017).

Numerous remote sensing (RS) based approaches have been regarded as the preferred methods for estimating ET in large area with relative high spatial resolution. Among those the SEBAL model and has proven to estimate evapotranspiration with better accuracy and the result calibrated with penman Monteith method as a reference method. When using the SEBAL it is common to obtain the result at a large scale, such as regional or catchment level. However, the scale difference corrected by considering different approaches' like using Downscaling technique, by comparing the SEBAL model result with ground truth data and by integrating weather data into SEBAL model, we can refine the result to align with the farm scale. SEBAL model is registered accuracies of 85% at a farm-scale while more than 95% accuracy has been recorded on a regional scale (Teuling et al., 2006). The research applied the model to large areas and found that evapotranspiration of wide areas of a plain can be calculated using the SEBAL model.

Upper awash basin is part of the Ethiopian climate mainly controlled by the seasonal migration of the Intertropical Convergence Zone (ITCZ) and associated atmospheric circulations related to its complex topography. The country has a diverse climate ranging from semi-arid desert types in the lowlands to humid and warm (temperate) classes in the southwest. Accordingly, the Awash basin ranges from moist in its upper basin to arid in its lower basin. Mojo is one of the major tributary for the upper Awash basin. The estimation of evapotranspiration using remote sensing-based approach unexplored research in the Mojo catchment (Alemu et al., 2022).

Therefore, to overcome this problem, satellite evapotranspiration estimation was employed in the Mojo catchment. The main objective of this study was, therefore, to estimate satellite evapotranspiration using Surface Energy Balance Algorithm for Land (SEBAL) by using Landsat images using SEBAL-python and GRASS and compare with Peman-Monieth methods. Consequently, it enables us to know the amount of water used by the evapotranspiration process from different land cover types in the Mojo catchment.

1.2 Statement of the Problem

A considerable number of river basins around the world lack sufficient ground observations of hydro-meteorological data for effective water resource assessment and management (Wonde et al., 2023). The prediction of ET for rangeland and natural systems in Mojo was poorly developed for weather-based systems and is severely limited by the sparseness of weather stations. Evapotranspiration is the most important part of the water cycle in moist sub-tropical inland. It plays a crucial role in water cycle research, agricultural water saving, water resource management, and drought monitoring. Emperical measurement techniques provide relatively accurate means to estimate components of energy balance but are essentially point-scale predictions. Such local-scale measurements are inadequate for studying the land surface energy balance at regional or global scales, due in part to the spatial heterogeneity of the land surface parameters and the dynamic nature of the evaporative process.

Mojo is one of the tributaries of the upper Awash basin, a major tributary for the Awash basin, which is the third largest basin in Ethiopia and an important agricultural base (Wendmu, 2021). In the catchment, there is a lack of sufficient weather station data, hindering accurate estimation of evapotranspiration (ET). Previous studies on actual evapotranspiration have primarily centered around examining ET values on an annual and monthly basis (Melesse et al., 2009). However, these studies aim to tackle this challenge by developing a dependable approach for estimating daily, monthly, and seasonal evapotranspiration using alternative data sources. Therefore, there is an urgent need for scientific and quantitative understanding of the watershed water balance items and their spatial distribution and temporal changes. These studies aim to address the challenge by developing a reliable method for evaluating spatial and temporal evapotranspiration using the SEBAL model in the scarce Mojo catchment with climate data and GRASS- Python in the Mojo catchment.

1.3 OBJECTIVES

1.3.1 General objective

The main objective of the study was estimation of spatial and temporal pattern of evapotranspiration estimation by satellite based SEBAL model, in mojo catchment.

1.3.2 Specific objectives

- To evaluate and compute ETa using the satellite based surface energy balance approach.
- To quantify spatial pattern of ETa for different land cover classes in Mojo catchment for the period of 2022.
- To calculate ETa by penman-Monteith method using ground observed data.

1.4 Research Questions

1. Does the SEBAL model estimates acceptable values of evapotranspiration in the remote sensing method?
2. Can SEBAL model properly evaluate the evapotranspiration and its patterns for the spatial and temporal variations of the catchment for different land use?

2. LITERATURE REVIEW

2.1 Background

Satellite based evapotranspiration estimation is decisive in stream flow simulation which is a major concern of hydrological modeling. Evapotranspiration is one of the main components of the water cycle and the importance of its accurate estimation is obvious, however, this is difficult to achieve in practice (Nouri et al., 2017). Because evapotranspiration cannot be measured directly and varies considerably in time and space (Running et al., 2019). For the past decades a number of algorithms have been developed to estimate evapotranspiration from different climatic and meteorological variables. Most of these algorithms are based on merging observation from satellite sensors to obtain global rainfall products with continuous space-time coverage. Some of merged satellite techniques to estimate evapotranspiration are Landsat, Moderate Resolution Imaging Spectro-radiometer (MODIS), and Multi-Functional Transport Satellite (MTSAT) (Liou & Kar, 2014).

The availability of remotely sensed data from different sensors of various platforms with a wide range of spatiotemporal, radiometric and spectral resolutions has made remote sensing the best source of data for large scale applications and study. The application of remote sensing to water resources is increasing through the use of remote sensing software and GIS (geographical information system) tools to manipulate process, store and retrieve such data with an aid of efficient computing system (Verstraeten et al., 2008). These information and hydrological parameters will increase our understanding of the different hydrological processes in quantifying the rate and amount of water and energy fluxes in the basin.

2.2 Evapotranspiration (ET)

Evapotranspiration is the process whereby water is evaporated from wet soil and/ or plant surfaces and from the vegetation to the atmosphere through small openings on the leaf surfaces called stomata (Pereira et al., 2015). ET plays an integral part in agriculture, climatology, and hydrology in estimating crop water requirement, crop stress, surface runoff, irrigation scheduling, drought, and water budget analysis (Aryalekshmi et al., 2021). More than 70% of rainwater returns to the atmosphere through evapotranspiration (Ajami, 2021). Apart from the water availability in the topsoil, the evaporation from a cropped soil is mainly determined by the fraction of the solar radiation reaching the soil surface. This fraction decreases over the growing period as the crop develops and the crop canopy shades more and more of the ground area. When the crop is small, water is predominately lost by soil evaporation, but once the crop is well developed and completely covers the soil, transpiration becomes the main process. Evapotranspiration (ET) is an important hydrological component with high variability in time and space, often required in disciplines of hydrology, meteorology, agriculture and environmental management (Shu et al., 2011).

2.2.1 Evapotranspiration assessment techniques at different scales of observation

As a result of the spatial heterogeneity of soils, vegetation type and cover, soil moisture status and plant water availability vary spatially (Makkeasorn et al., 2006). Furthermore, the dependency of hydrological processes on meteorology and climate makes ET, spatially and temporally variable. The interaction between the spatial and temporal dimension of evaporation processes result in a complex methodology for ET assessment (Bastiaanssen et al., 1998). Estimating evapotranspiration is an important task in hydrology and agricultural science.

The empirical method for estimating evapotranspiration involves the use of the Penman equation as a reference, which serves as a baseline for comparing other estimation methods. Evapotranspiration can be estimated using the Penman equation, which was created by Howard Penman. It is predicated on the idea that temperature and radiation both affect evapotranspiration. In order to determine evapotranspiration, the equation takes into account variables like net radiation, wind speed, air temperature, humidity, and other pertinent parameters. The Penman equation is considered a radiation-based method because it explicitly incorporates the effect of solar radiation on evapotranspiration. Solar radiation is a significant driver of evapotranspiration as it provides the energy required for water to change from a liquid to a water vapor state. In contrast, other estimation methods may be temperature-based, focusing primarily on the influence of air temperature on evapotranspiration. These methods often simplify the calculation by considering temperature as the dominant factor affecting evapotranspiration while neglecting or approximating other variables. Estimating evapotranspiration is an important task in hydrology and agricultural science. (Ravazzani et al., 2012).

2.3 Reference evapotranspiration (ETo)

Reference evapotranspiration defined as “the rate of evapotranspiration from a alfalfa crop with an assumed crop height (0.12 m) and a fixed canopy resistances 70 s m−1d and albedo (0.23) which would closely resemble evapotranspiration from an extensive surface of green grass cover of uniform height, actively growing, completely shading the ground and not short of water” (Trajkovic, 2005). The concept of the reference evapotranspiration was introduced to study the evaporative demand of the atmosphere independently of crop type, crop development and management practices. As water is abundantly available at the reference evaporating surface, soil factors do not affect ET. Relating ET to a specific surface provides a reference to which ET from other surfaces can be related (Kumar et al., 2012). To facilitate the research and calculation, the reference evapotranspiration has been put forward assuming the vegetation condition is under the condition of sufficient water supply. It is also called reference crop evapotranspiration which evaporation and transpiration from short, well-watered grass or open water (Yang et al., 2022). The concept of the reference, ETo can be computed from climatic data and by integrating directly the crop resistance, albedo and air resistance factors in the Penman-Monteith approach (Verstraeten et al., 2008).

2.4 Remote sensing application in water balance study

Remote sensing is the process of acquiring, analyzing, monitoring the physical characteristic of an area by recording the radiation energy that is reflected and emitted without having any physical contact with the object under study. Remote sensing collects data by detecting the energy that is emitted from earth. This sensor can be on satellite or mounted on air craft. It help to provide the latest information as well as help in planning and natural resource management. Remote sensing satellite data have unique advantages such as; large area coverage at a time, a synoptic view of a given area, and consistent coverage of the area at regular intervals (Pramanik, 1993), as well as have disadvantages such as the incapability of the sensors to acquire adequate data and information through the cloud, the same look of different phenomena by the sensor, the coarse resolution of the satellite imagery for detailed mapping (MohanRajan et al., 2020). Despite these disadvantages, remote sensing data play significant role in the management, assessment, monitoring of natural resources include agriculture, forest, water, and geology (Fonji & Taff, 2014). In the last two decades a need to quantify ET at global and or regional scale coupled with current advancements in satellite technology has led to the widespread application of remote sensing ET algorithm with the surface energy balance. Remote sensing technology can quickly access a wide range of real time land surface spatial information and provide an effective way for resource surveys, environmental monitoring and disaster prediction. Several hydrological models and remotely-sensed based surface energy balance models are currently used in ET simulations globally (López et al., 2017). However, the relative accuracy of these models relative to one another should be extensively explored to improve our understanding of the ET estimation from these algorithms; one of the more prominent ones will be evaluated in this study. The surface energy balance algorithms of land (SEBAL), while SEBAL algorithm has been operated by using Landsat 8 image after preprocessing in QGIS and GRASS GIS.

2.5 Land use land cover

The two terminologies; land use and land cover are not similar. Land use is the purpose humans use the land for and it is motivated by production and consumption dynamics including industrial zone, residential areas, and agricultural fields, grazing, and mining among others whereas land cover is the physical state of the terrain surface including forests, cropland, topography, soil, and water (Tena et al., 2019). In history, the rate of land modification by humans to obtain the essentials for their survival was not similar as it is today (Parveen & Ilahi, 2022). Population expansion, economic development, and pressures for land for agriculture are the main drivers for such land changes. Understanding the effect of LULC change plays a critical role in sustainable land and water management (Kiros et al., 2015). Decreased forest lands, shrub lands, and grasslands were accompanied by the drastic expansion of agricultural land which greatly influenced the mean annual streamflow. The global atmospheric circulation, global warming, and variation of streamflow are important indicators of LULC changes (Munoth & Goyal, 2020). The LULC changes are significant in watershed studies. It has a considerable effect on the quantity of streamflow, groundwater recharged, surface runoff, evapotranspiration, infiltration, and base flow (Kumar, Batar et al., 2017). A land-use map is not a requirement for SEBAL but is highly recommended since it is useful in estimating the surface roughness parameter.

2.6 Surface Energy Balance models

Studies comparing a number of SEB model are needed to identify model benefits and inadequacies to help guide future model development (French et al., 2015). There are many studies that compare the performance of SEB model. However most study compares two or three SEB model based on how to sinks or source of energy fluxes are parametrized at the land atmospheric interface (Kustas & Norman, 1996). The basic ideology of the SEB model is that energy is balanced in the vertical direction, while the input and consumption of energy in the horizontal side is negligible. The SEB model estimates the sensible heat flux and soil heat flux, then the latent heat flux can be derived from the residual of the energy balance equation (Sun & Yong, 2019).

$\mathbf{LE = Rn - G - H}$ ……………......………………………………..………..Equation 2.1

$ETa = 3600 \times LE/\lambda$ (2)..……………………………………………………..Equation 2.2

where LE is the latent heat flux (W/m^2), Rn is the net radiation flux (W/m^2), G is the soil heat flux ((W/m^2), H is the sensible heat flux ((W/m^2), λ (kJ/kg) is the latent heat of vaporization and ETa represents the hourly ET value. Rn is the sum of incident shortwave and longwave radiation, which can be calculated from the radiation balances principle, and G is available (Allen et al., 2007).

The process of determining H in each of the four SEB models is described in the following sections. In the last decade , a number of single source surface energy balance model have been proposed for mapping Evapotranspiration (ET) however there is no clear guidance on which model are preferable under different condition. In a single–source SEB model, no distinction is made between vegetation and soil and hence uses a bulk of sensible heat flux (H) formulation, unlike a two-source model, where the components of sensible heat flux (H) are partitioned between the soil and vegetation. The process of determining H in the five single-source SEB models is described in the following sections (Bhattarai et al., 2016).

2.6.1 Surface Balance Energy System (SEBS)

SEBS (Surface Balance Energy System) is a widely used tool in hydrology and land surface modeling. It is a physical based model that simulates the surface energy balance and related process in various nature and agricultural landscape .the model was developed to estimate the partitioning of available energy at the land surface into its different component, including sensible heat flux, latent heat flux and ground heat flux. The SEBS model has proven to be a valuable tool in understanding and quantifying the complex interaction between the land surface and the atmosphere. Its simplicity, versatility, and ability to integrate remote sensing data make it a widely used model in hydrological and climate research, contributing to our understanding of the earth's energy balance and water cycle (Kwast & Jong, 2004).

2.6.2 Simplified Surface Energy Balance Operational (SSEBop)

Unlike the other SEB models, which require an estimation of the aerodynamic temperature scalar, the simplified surface energy balance (SSEB) temperature quantity is derived directly from the maximum ET (Liou & Kar, 2014). It converts land surface temperature into an ET fraction through the hot pixel and cold pixel, where the hot pixel and cold pixel represent no ET and maximum ET, respectively. In general, the hot pixels can be selected from dry and bare areas (low NDVI), whereas the cold pixels are identified from well-vegetated and well-irrigated areas (high NDVI) (Zhuang et al., 2021).

2.6.3 simplified surface energy balance index (SS-SEBI)

The simplified surface energy balance index (SS-SEBI) model is a simplified version of SEBI model which stands for surface energy balance index. The SS-SEBI model is used for estimation actual evapotranspiration from satellite imagery. It is particularly suitable for regions where ground-based metrological data is limited or unavailable. it utilize remote sensing data , such as satellite imagery, along with simplified set or input parameter to estimate Eta . It consider factor like vegetation indices, land surface temperature and reference evapotranspiration to calculate the surface energy balance and subsequently estimate Eta. Its accuracy and ease of implementation make it a practical choice for various application related to water resource and land management. It also estimates LE via an evaporative fraction derived from the linear relationship between surface temperature (Ts) and albedo (α) (Sun & Yong, 2019).

2.6.4 Mapping Evapotranspiration at high Resolution with Internalized Calibration (METRIC)

An energy balancing model called SEBAL was created in the Netherlands. One variation of SEBAL is called Mapping Evapotranspiration at high Resolution with Internalized Calibration

(METRIC). As a byproduct of the energy balance at the Earth's surface, regional ET can also be mapped using this image-processing technology over more intricate surfaces. By integrating with reference ETa was determined using meteorological data gathered from the ground METRIC has expanded upon SEBAL. The basic idea of METRIC is that heat is absorbed by evaporating liquid droplets. to calculate ET using ground-based observations of wind speed and near-surface dew point temperature in conjunction with remotely sensed data in the visible, near-infrared, and thermal infrared spectral areas (Allen et al., 2007). To fix boundary conditions for the energy balance and to internally calibrate the sensible and latent heat flow computation, two anchor conditions are chosen inside an observed scene. An extensive atmospheric adjustment of surface temperature or reflectance (albedo) readings using the radiative transfer model is not necessary with such internal calibration Like SEBAL, the internal calibration lessens the effects of any biases in the surface roughness or aerodynamic stability correction estimation. A hot and a cold pixel are manually selected as part of the calibration process in order to establish the range of vertical temperature gradients (dT) above the surface. A well-irrigated alfalfa field with ET = ETr (reference ET over the standardized 0.5 m tall alfalfa in mm/h) is usually considered the cold condition. Usually, a dry, barren agricultural area with ET = 0 is the hot state (Griffith, 2002).

2.6.5 Surface Energy Balance Algorithm for Land (SEBAL)

The Surface Energy Balance Algorithm for Land is an image-processing model comprised of 25 computational steps that calculate the actual (ETa) and energy exchanges between land and atmosphere (Allen et al., 2002). This model is an intermediate approach using both empirical relationships and physical parameterization. It requires digital imagery data collected by any satellite sensor measuring visible, near-infrared, and thermal infrared radiation, Ts, NDVI, and albedo maps. Latent heat flux (LE) is estimated as a residual of the energy balance equation on a pixel-by-pixel basis. Net radiation (Rn) is computed from the balance of short and longwave radiation. Soil heat flux (G) is calculated utilizing the equation proposed by Noordman, which is applicable to all sorts of vegetation cover and soil type (Bastiaanssen et al., 2005). Under several climatic conditions, this method has been verified at both field and catchment scales with typical accuracy at field scale being 85% and 95% at daily and seasonal scales, respectively, in more than 30 countries worldwide (Du et al., 2013). The estimation of sensible heat flux (H) is required to obtain the parameters that will allow the computation of ET as a residual from the energy balance. In SEBAL, two reference air temperatures are taken. One being an air temperature located at height h1 close to the surface and the other at an upper height h2. To determine the value of dT for each pixel, SEBAL assumes the existence of a linear relationship between dT and the radiometric surface temperature Ts considering homogeneous meteorological and surface conditions:

$\mathrm{dT} = \mathrm{cTs} + \mathrm{d}$……………………...……………………………………………Equation 2.3

where dT is the near-surface air temperature difference, Ts is the radiometric surface temperature, and “c” and “d” are empirical coefficients obtained from the so-called “anchor” pixels (Bastiaanssen et al., 2005), for a given satellite image. Generally, the anchor pixels within the image represent conditions of extreme evaporative behavior. Evaporation is assumed to be consuming most of the available energy (Rn − G) at a “wet (cold)” pixel, which indicates that the sensible heat flux (H), and consequently dT are both assumed to be near zero (dTwet = 0). At a “dry (hot)” pixel where evaporation is near zero, all the available energy is modified essentially into sensible heat.

The main benefits of using SEBAL for estimating land surface fluxes from thermal remote sensing data are that it requires less supplementary ground-based data, that atmospheric effects on surface temperature can be corrected automatically, and that internal calibration is completed within each analyzed image. When calculating ET, SEBAL performs a number of calculations that result in: The surface energy balance model is one of the popular methods (Odusanya et al., 2019). In this study, In specifically, I discuss the widely used single-source SEB model, known as SEBAL model, that unites hot and cold pixel-based fully energy balancing models and forecasts ET for each pixel using thermal-based remote sensing data. Because of this, remote sensing is thought to be a good alternative to ET estimation in the area. The fact that so few studies have looked at remote sensing-based ET predictions throughout the Mojo watershed, despite ET's importance to the region's water budget, is another reason to do this research (Allam et al., 2021).

2.6.6 Two-Source Models (TSM)

Norman proposed a new model named two-source model, also known as duel-source model to improve the accuracy of LE estimates using satellite remote sensing data, especially over sparse surfaces (Kustas & Norman, 1996). The basic principle of this model is to partitioning the composite radiometric surface temperature into soil and vegetation components, and considered sensible and latent heat fluxes are transferred to the atmosphere from both surface components. Dispensability of ground-based information or any priori calibration has made the applicability of duel source model wider without resorting to any additional input data. In the duel source model, satellite-derived surface temperature (Ts) is considered to be a composition of the soil (Tsoil) and canopy temperatures (Tveg), and H and LE are also divided into soil and vegetation contributions, respectively. Canopy latent heat flux is computed using the Priestley-Taylor equation (Nazila, Taghi Sattari et al., 2021). An iterative method is used to obtain the soil (Tsoil) and canopy temperatures (Tveg) from satellite-derived Ts setting an initial value of 1.3 for the Priestley-Taylor parameter α (Laipelt et al., 2020). This nominal choice of α overestimates canopy latent heat flux under moisture-stressed conditions and yield negative soil evaporation (LEsoil) and is regarded as a nonphysical solution during the daytime. The α is therefore iteratively reduced until LEsoil approaches zero to obtain a final α as well as Tsoil and Tveg. The LE and H are then calculated from these estimates. Both the one- and Two-source models are sensitive to their use of the temperature differences to estimate H. Dispensability of precise atmospheric corrections, emissivity estimations and high accuracy in sensor calibration are the main advantages of the duel source method. Coupling of the duel source models with PBL eliminates the need of ground-based measurement of Ta and, thus, is much better suitable to applications over large-scale regions than other algorithms (Kustas & Norman, 1996). Effects of view geometry are normally incorporated, while the empirical corrections for the “excess resistance” are eliminated in the duel-source models.

Table 2. 1 Comparisons of the different remote sensing ET models.

Algorithms	Input Parameters	Main assumptions	Merits	Demerits
SEBS	Tair, ha, v, Ts, Rn, G	(ET)dry limit = 0; (ET)wet limit → takes place at a potential rate	Uncertainty in SEBS from Ts and meteorological parameters can partially be solved; Roughness height for heat transfer is computed explicitly instead of using fixed values	Requires too many parameters; Relatively complex derivation of turbulent heat fluxes
SEBI	pbl, hpbl, v, Ts, Rn, G	(ET)dry limit = 0; (ET)wet limit → evaporates potentially	Relating the effects of Ts and ra directly on LE	Requires ground based measurements
S-SEBI	Ts, αs, Rn, G	$(EF)\alpha = (TH - TS)(TH - TLE)$ $TH = (LEmin)$ $TLE = (LEmax)$	Ground based measurements are not required	Extreme temperatures are location specific
METRIC	v, ha, Ts, VI, Rn, G	(ET)hot pixel = 0 (LE)wet pixel = 1.05ETr	Similar to SEBAL, but surface slope and aspect can be considered Possesses	uncertainties in the determination of anchor pixels
SEBAL	v, ha, Ts, VI, Rn, G	dT = cTs + d (ET)dry pixel = 0; (ET)wet → considered as the surface available energy	Requires minimum Ground based measurements; Equipped with automatic internal calibration; Exact atmospheric corrections are not required	Applied over plain surfaces; Possesses uncertainties in the determination of anchor pixels
TSM	v, ha, Tair, Ts, Tc, Fr or LAI, Rn, G	Component fluxes are parallel to each other; Priestly-Taylor equation is used to compute canopy transpiration	Includes the view geometry Eliminates the need of empirical corrections for the "excess resistance".	Many ground measurements and components are needed

2.7 Digital Elevation Model (DEM) Application in hydrology

DEM is a grid of square cells where each cell represents the elevation value at that location and the elevation value for each cell is an average of overall elevations inside the cell. The size of each cell determines the resolution of the DEM. It is the digital representation of the land surface elevation with respect to any reference datum. It is frequently used to refer any digital representation of a topographic surface and it is the simplest form of digital representation of topography. DEMs are used to determine terrain attributes such as elevation at any point, slope and aspect. Terrain features like drainage basins and channel networks can also be identified from the DEM. Hydrologic applications of the DEM include groundwater modeling, estimation of the volume of proposed reservoirs, determining landslide probability, flood prone area mapping (Haque et al., 2021).

2.8 Ground based empirical method of estimating Evapotranspiration

Empirical methods for estimating evapotranspiration (ET) involve various techniques based on empirical formulas and meteorological data. One widely used approach is the Penman-Monteith equation, which combines the energy balance and aerodynamic components to estimate ET. It requires measurements of meteorological variables such as temperature, humidity, wind speed, and solar radiation. Another commonly employed method is the Blaney-Criddle equation, which is a simpler approach using temperature and monthly pan evaporation data. The Hargreaves equation is another widely used method that estimates ET solely based on temperature data. These empirical methods rely on historical weather data and empirical relationships, making them accessible and applicable in areas with limited data availability. However, they may have limitations in accurately capturing site-specific conditions and the effects of vegetation and soil moisture variations. Advancements in remote sensing and modeling techniques have provided alternative approaches to estimate ET, offering improved accuracy and spatial coverage. ET values were computed by different empirical methods using REF-ET software. The value of Standard P-M for the weather station was used as a reference to compare the values obtained from other emperical methods (Joshi et al., 2015).

2.8.1 Penman-Monteith equation

Penman combined the energy balance with the mass transfer method and derived an equation to compute the evaporation from an open water surface from standard climatological records of sunshine, temperature, humidity and wind speed. This so-called combination method was further developed by many researchers and extended to cropped surfaces by introducing resistance factors. The resistance nomenclature distinguishes between aerodynamic resistance and surface resistance factors The FAO Penman- Monteith method is considered to be the most physical and reliable method. However, it needs four meteorological parameters: air temperature, relative humidity, wind, and sunshine hours, which may not be everywhere available (measured at few weather stations), even in the developed countries. For some locations the required climate data are available but of questionable quality, especially in developing countries (Droogers & Allen, 2002). The FAO-PM method is more accurate and reliable to calibrate other methods. The Penman-Monteith Equation is given by the following equation (Allen, 2016).

$$ETO = \frac{(\mathbf{0.408}\Delta(\boldsymbol{Rn}-\boldsymbol{G})+\boldsymbol{\gamma}(\frac{\mathbf{900}}{T+273})\boldsymbol{u2}(\boldsymbol{es}-\boldsymbol{ea}))}{(\Delta+\boldsymbol{\gamma}(\mathbf{1}+\mathbf{0.34}\boldsymbol{u2}))} \text{………………………………………… Equation 2.4}$$

Where, ETo: reference evapotranspiration [mm day^{-1}], Rn: net radiation at the crop surface [MJ m^{-2} day^{-1}], G: soil heat flux density [MJ m-2 day-1], T:mean daily air temperature at 2 m height [°C], u2: wind speed at 2 m height [m s^{-1}], Es: saturation vapour pressure [kPa], Ea:actual vapour pressure [kPa], es-ea:saturation vapour pressure deficit [kPa], Δ: slope vapour pressure curve [kPa °C^{-1}], γ: psychrometric constant [kPa °C^{-1}].

The FAO-56 Penman–Monteith Method requires numerous weather data: maximum and minimum air temperature, maximum and minimum relative air humidity or the actual vapor pressure, wind speed at 2m height, and solar radiation or sunshine (hours). The basic obstacle to widely using the FAO-56 Penman–Monteith method is the numerous required data that are not available at many weather stations. A serious problem is the quality of the data. Solar radiation data are not always reliable (Zotarelli et al., 2010). Wind speed at 2 m height may be site specific, or of questionable reliability. Measurement of relative humidity by electronic sensors is commonly plagued by errors (Tomar, 2022). Where radiation data are lacking, or are of questionable quality, the difference between the maximum and minimum temperature can be used for the estimation of solar radiation (Moratiel et al., 2019).

2.8.2 Hargreaves method

The Hargreavesi method is a simplified empirical approach for estimating ETo. It uses temperature data and latitude information to estimate potential evapotranspiration. This method is widely used when meteorological data availability is limited.

ETo = 0.0023 * Ra * (Tmax - Tmin) * sqrt(Tavg + 17.8)…………………… Equation 2.5

Where:

ETo = Reference evapotranspiration (mm/day)

Ra = Extraterrestrial radiation ($MJ/m^2/day$)

Tmax = Maximum daily air temperature (°C)

Tmin = Minimum daily air temperature (°C)

Tavg = Average daily air temperature (°C)

2.8.3 Blaney-Criddle method

The Blaney-Criddle method estimates reference evapotranspiration using temperature data and a crop-specific factor. It is a relatively simple method that provides reasonable estimations in areas with limited data availability. However, it may have limitations in areas with high humidity or unusual climatic conditions.

ETo = C * (Tavg - Base)…………………………………………………… Equation 2.6

Where:

ETo = Reference evapotranspiration (mm/day)

C = Crop factor (varies depending on the crop type)

Tavg = Average daily air temperature (°C)

Base = Base temperature (°C)

2.8.4 Thornthwaite method

The Thornthwaite method estimates potential evapotranspiration based on temperature and latitude. It uses a heat index approach, considering the effect of temperature on evapotranspiration. This method is commonly used for long-term water balance studies and regional assessments.

Thornthwaite Method:

The Thornthwaite method estimates potential evapotranspiration (PET) using the following formula:

PET = (0.6 * (10 * Tmean / I)^a) * (12 / 30.4)…………………………………. Equation 2.7

Where:

PET = Potential evapotranspiration (mm/month)

Tmean = Mean monthly air temperature (°C)

I = Heat index, calculated as the sum of the average monthly temperature (°C) raised to the power of 1.514 for each month of the year

a = Empirical coefficient, typically ranging from 1.25 to 1.5

2.8.5 FAO-56 Method

The Food and Agriculture Organization (FAO) developed the FAO-56 method, which provides guidelines for estimating crop evapotranspiration (ETc). It combines the reference evapotranspiration (ETo) estimated by the Penman-Monteith method with crop-specific coefficients (crop coefficient, Kc) that account for crop type, stage, and management practices (Zotarelli et al., 2010). The FAO-56 method calculates crop evapotranspiration (ETc) as the product of reference evapotranspiration (ETo) and a crop coefficient (Kc) specific to the crop and its growth stage:

ETc = ETo * Kc……………………………………………………………… Equation 2.8

Where:

ETc = Crop evapotranspiration (mm/day)

ETo = Reference evapotranspiration (mm/day)

Kc = Crop coefficient (dimensionless)

2.8.6 Priestley-Taylor Method

The Priestley-Taylor method estimates potential evapotranspiration using solar radiation data. It assumes that the ratio of actual evapotranspiration to potential evapotranspiration remains constant under non-water-limited conditions. The Priestley-Taylor method estimates potential evapotranspiration (PET) using the following formula:

$PET = \alpha * \Delta / (\Delta + \gamma) * Rn$………………………………………………………… Equation 2.9

Where:

PET = Potential evapotranspiration (mm/day)

α = Priestley-Taylor coefficient, typically assumed to be 1.26

Δ = Slope vapor pressure curve (kPa/°C)

γ = Psychrometric constant (kPa/°C)

Rn = Net radiation at the crop surface ($MJ/m^2/day$)

2.9 Reference Evapotranspiration (REF-ET)

REF-ET (Reference Evapotranspiration) software is a powerful tool designed for calculating evapotranspiration values. It plays a crucial role in understanding the water needs of crops, estimating irrigation requirements, and managing water resources efficiently (Xp & Allen, 2016). REF-ET's accuracy, standardized approach, integration capability with the SEBAL model, user-friendly interface, and widespread acceptance make it a popular choice for estimating evapotranspiration within the SEBAL framework. Its specialized focus on reference evapotranspiration estimation aligns well with the requirements of the SEBAL model, ensuring reliable and consistent results (Copyright & Allen, 2000).

3. MATERIALS AND METHODS

3.1 Description of Study Area

3.1.1 Location of study area

Mojo River catchment is mainly located in the upper awash basin in Oromia Regional State in Ethiopia. With a geographical location between longitude 38^0 54′to 39^0 17′E and latitudes 08^0 34′to 09^0 06′N and an elevation between 1597 and 3086 meters above sea level (figure 3.1) Mojo River is a perennial river that flows through, the town of Mojo located some 43 km southeast of the capital Addis Ababa. It is a tributary of the Awash River receiving effluents. In addition, extensive agricultural practices and human urban lands have been altering the catchment and riparian zone of the Mojo River. The catchment covers a surface area of 1599.19Km^2 delineated using ArcMap 10.3 with a 30 m x 30 m digital elevation model acquired from the USGS website https://earthexplorer.usgs.gov. Agriculture is the dominant practice in the watershed and the basic source of livelihood.

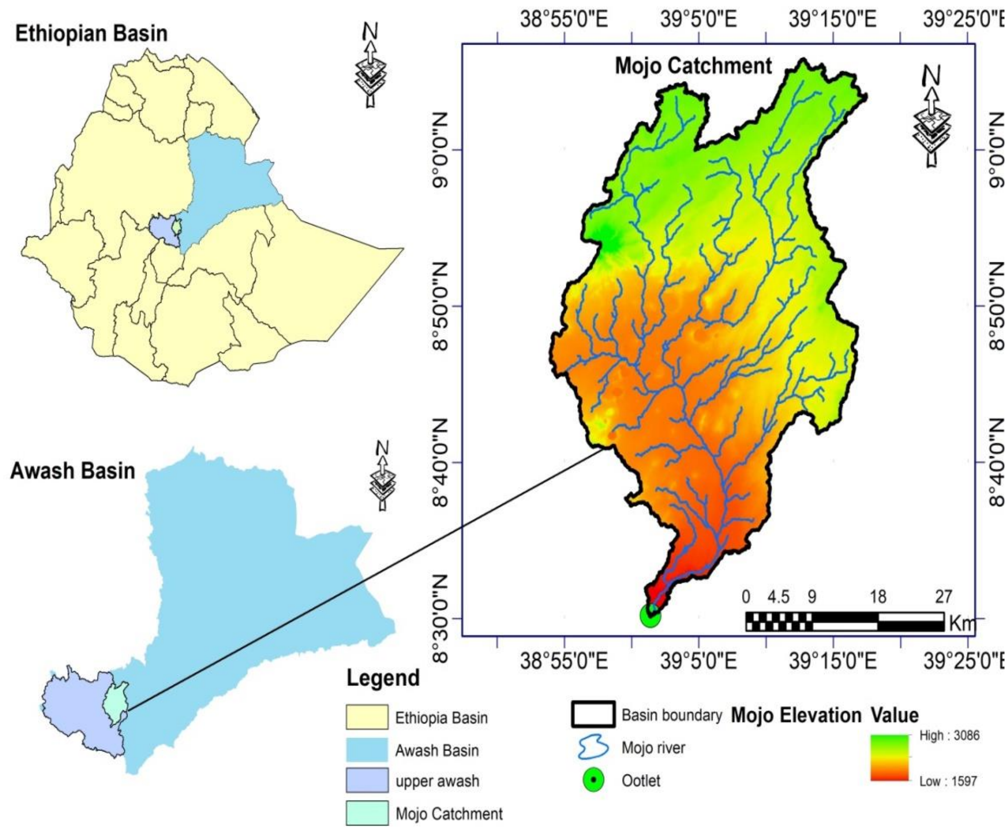

Figure 3. 1 Location map of the study area

3.1.2 Soil of the area

According to the Ethiopian Ministry of Water and Energy the dominant soil types identified in the Mojo catchment includes Eutric Vertisoils, Vertic cambisols, Haplic Luvisols, Luvic Phaeozems, and Lithic Leptosols covers, Chromic lavisols and Mollic Andosols which is extracted from A wash basin soil map. And the dominant land use type in the Mojo catchment is rainfed agricultural land (Biru & Kumar, 2017).

3.1.3 Climate of study area

The majority of the catchment particularly the central and lower part of the catchment has a mono modal rainfall pattern whereas the upper part of the catchment is characterized as bimodal. More than 80% of the annual rainfall is received from June to September (locally known as Kiremt) whereas the short season extends from February/March to May (locally known as Belg) (Biru & Kumar, 2017). and reported exhibiting most rainfall occurring between June and October. The Mojo catchment and its tributaries are a perennial source of water in the study area. The total annual mean flow of the catchment is 214.5 m^3/s (Alemu et al., 2022). Mojo River, which joins Lake Koka from the north, the storage mainly fed during the wet season from June to September. After being released through the dam the Awash descends into the Rift Valley northwest towards Awash Station from where the river follows the valley northwards into Gedebassa Swamp near Hertale (Gudeta, 2010).

3.1.4 Topography

Slope within the basin ranges from 0% to 61.19%. About 40.68% of the area is a flat or nearly level slope land having a slope of 0-3%, about 46.70% of the area is undulating slope with a slope of 3%-8%, 8.58 % of the area is rolling slope of 8%-15%, 3.42% of the area is hilly slope of 15%-30% and 0.62% of the area is steep slope having slope greater than 30%. The slope and aspect were calculated from the DEM using models provided in the ARC GIS software. The coordinate system and the slope map shown in figure 3.2 below.

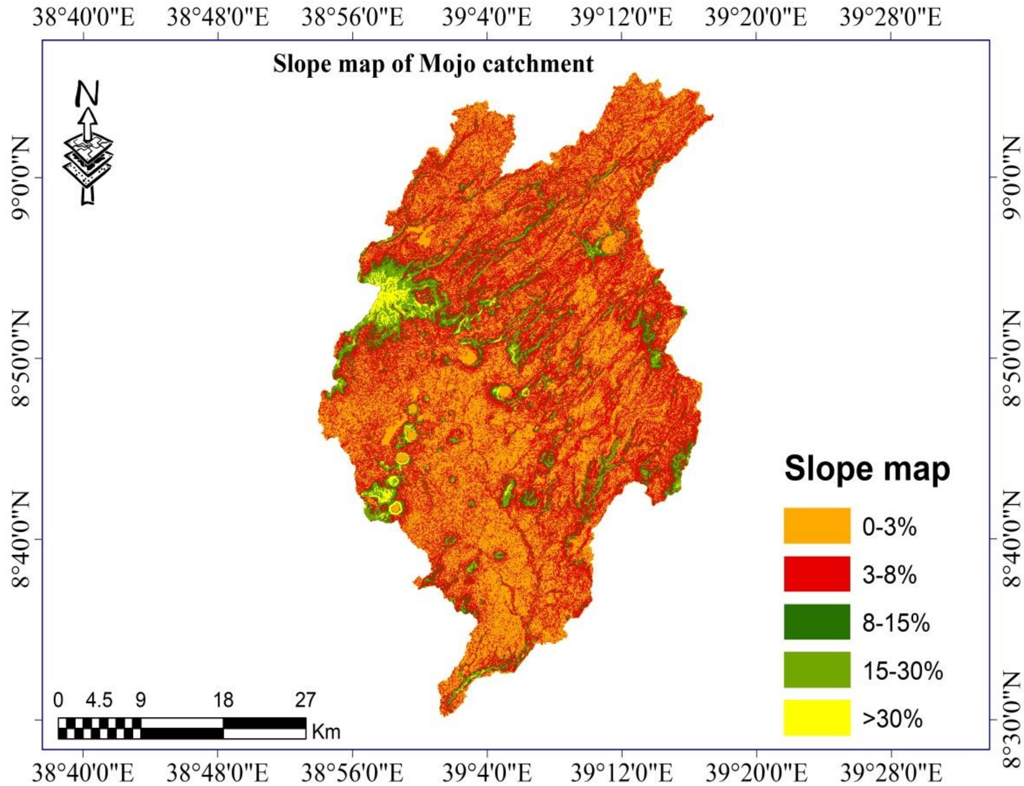

Figure 3. 2 Slope map of mojo catchment

3.2 Data collection and preparation

The research aim to look into the evapotranspiration patterns in an area where there isn't much access to meteorological data. Data from remote sensing and meteorology will be combined and prepared in order to do this. Meteorological data was identified for weather stations in and around the study area for the meteorological data. Meteorological data is an important input to estimate evapotranspiration using both remote sensing and Penman-Monteith approaches From these stations, historical meteorological data has been gathered from Ethiopia national metrological station, including temperature, humidity, wind speed, and sun radiation. Furthermore, reanalysis datasets or data from neighboring weather stations was used to fill in the gaps. For the study area, Landsat 8 satellite imagery has been obtained in terms of remote sensing data. The SEBAL model relies heavily on these imagess for vital inputs such as vegetation indices and land surface temperature data.

3.2.1 ASTER Global Digital Elevation Model

The Advanced Space borne Thermal Emission and Reflection Radiometer, Global digital elevation model (ASTER GDEM) with spatial resolution of 30 meters was used in the study to show elevation in different parts of the catchment. To account for differences in slope, (Allen et al., 2022) aspect, and elevation, a digital elevation model (DEM) was used for the SEBAL mountain model. This data is available in both Arc-Info and ASCII and GeoTiff format to facilitate their ease of use in a variety of image processing and GIS applications and were downloaded from the website (www.earthexplorer.usgs).

3.2.2 Satellite images data

Sentinel Images

In this paper three sentinel image with 10m resolution was downloaded in Copernicus open access hub, and the images composite together to extract the study area ,after extracting the image with mojo catchment the land use land cover classification has been done with ERDAS software 2014.

Table 3. 1 Sentinel image data characterstics

year	Month	date	Sentinel images	Resolution
2022	January	23	S2A_MSIL2A_20220123T074221_N0301_R092_T37PEK_20220123T101229.SAFE	10m
2022	January	23	S2A_MSIL2A_20220123T074221_N9999_R092_T37PEL_20221127T042755.SAFE	10m
2022	February	22	S2A_MSIL2A_20220222T073931_N9999_R092_T37PDK_20221206T023452.SAFE	10m

Landsat images

In this study, Landsat 8 images data (path: 168, row: 54) was selected during the dry season (Oct to Mar) for the period of 2022 used. The images used in this study was downloaded free of charge from U.S. Geological Survey 7 (http://earthexplorer.usgs.gov). The image data projection information is UTM, zone 37 WGS 84 datum. The image with cloud covers free pixels (less than 10% cloud). The Landsat images must be georeferenced so that the final ET “map” is accurately referenced to earth coordinates. It is recommended that the georeferenced image be saved in the GeoTIF format and that nearest neighbor resampling be used during preserve spectral information. Cloud free images were used, however, data gaps in certain images (i.e. October and November) were affected by the cloud. In order to reduce the uncertainty associated with this, cloud were removed and corrected using an advanced interpolation techniques using neighboring pixels or unclouded pixels from the next available and the previous image. Quantum GIS (QGIS) software was used to produce a layered spectral band image necessary for the SEBAL procedure. Once a layered image is produced, the study area image can be made if a smaller area of interest is desired.

Table 3. 2 Description of the Landsat 8 images used to implement the Surface Energy Balance Algorithm for Land (SEBAL)

Year	Month	DOY	DOM	Landsat
2022	January	24	24	LC08_L1TP_168054_20220124_20220128_02_T1.tar
2022	February	40	09	LC08_L1TP_168054_20220225_20220303_02_T1.tar
2022	March	72	13	LC08_L1TP_168054_20220313_20220321_02_T1.tar
2022	October	296	23	LC08_L1TP_168054_20221023_20221101_02_T1.tar
2022	November	328	08	LC08_L1TP_168054_20221108_20221115_02_T1.tar
2022	December	344	10	LC08_L1TP_168054_20221210_20221219_02_T1.tar

DOY: Day of the year DOM: Day of the Month

3.2.3 Meteorological data and ground observation data

SEBAL requires a satellite image and some weather data. Meteorological data were collected from National Meteorological Agency (NMA) of Ethiopia. The daily climate data from in and close to study area ware used. Automatic weather station data within hourly data were recommended for the process of SEBAL model includes: minimum and maximum temperature, average wind speed (required, hourly data is preferred), Precipitation (hourly data are recommended for the dry season prior to the image). In addition to wind speed data, Solar radiation (hourly is preferred), Air Temperature (hourly is preferred) for calculating instantaneous value of reference evapotranspiration, and daily value of reference evapotranspiration (Semaw et al., 2019). In this study, one years of hourly weather station data (2022) collected from Nazret Automatic weather station located near to mojo catchment was used. The sampe data obtain in (Table 7.1 in appendices).

3.4 Land use land covers classification

It is the technique of classifying the image's picture elements (pixels) according to certain spectrum information. Sentinel photos were designated for categorization. In order to classify the land cover and land use in the area, a sentinel picture of a comparable study area was downloaded from the Copernicus Open Access Hub. A satellite called Sentinel has a spatial resolution of 10, 20, and 60 meters. The period between each satellite revisit and the spatial resolution is ten days. Bands 2, 3, 4, and 8 stacks together in these study land use and land cover classification, making it a superior choice for the selection process. Only 10m resolution was used. To isolate the research region, three image compilations were combined as well. A crucial factor in determining the LULC map's accuracy is sample size. The categorized map's correctness was confirmed using a variety of methods, including ERDAS Imagine and Google Earth. The classification process consists of the following basic stages: downloading and selecting Sentinel photos with a 10m resolution, preprocessing the images, supervised classification, and accuracy evaluation.

3.4.1 Supervised classification

The supervised classification is an image processing technique that allows for the identification of materials in an image, according to their spectral signatures. The choice of the algorithm depends on the purpose of the classification & the characteristics of the image and training data. In this study, the Maximum Likelihood Classification (ML) algorithm has been selected to undertake supervised classification. The ML has been the most popular parametric classifier used for remote sensing data classification (Bushira, 2019) and unlike other classifiers it considers the spectral variation within each category and the overlap covering the different classes (Tena et al., 2019). ML also allows the operator to define a threshold distance by defining a maximum probability value. The object of image classification is the categorization of all pixels of an image into land cover classes.

The Sentinel images have been processed using ERDAS IMAGINE software. In order to extract the study area, three images had to be downloaded. Once the reference image had been corrected to a specific map projection, registration had to be completed for the same study area to be assigned for the same object that was seen in each image. 278 training sample(polygon) have been used for the use of supervised classification.

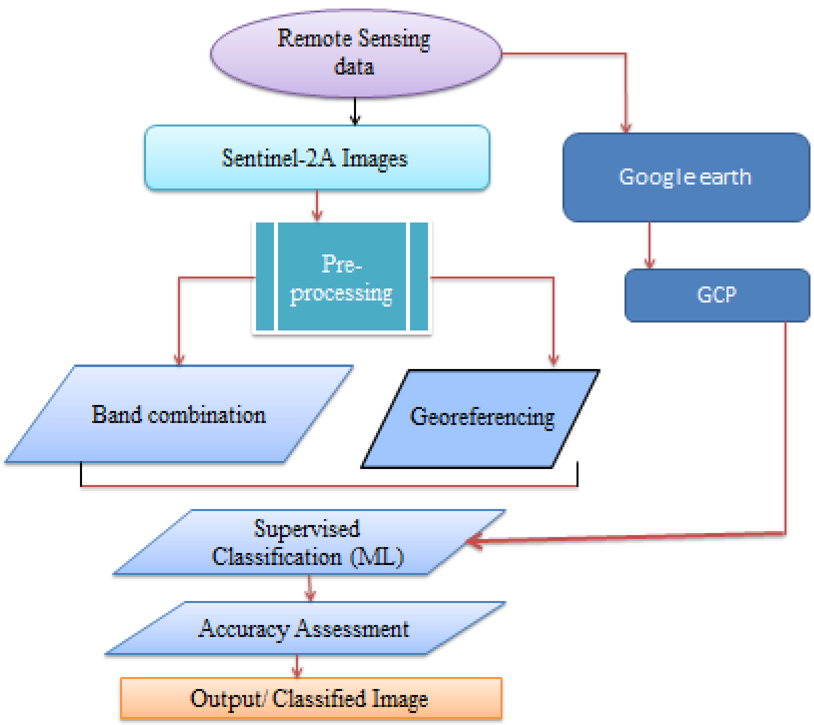

Figure 3. 3 General schematization of land use land cover classification

3.4.2 Accuracy assessment for the classified images and calculating Kappa Statistics

One of the most common means of expressing 3.3 Research design flow chart

The main phases of this study include: Downloading sentinel image, and by referring this image with Sentinel image we can classify the land use land cover. Landsat 8 preprocessing, supervised classification, accuracy assessment, pre-and post- processing for SEBAL model. From figure 3.3 below rah represent aerodynamics resistance to heat resistance, a, and b slope and intercept respectively for the relationship between surface temperature and vapor pressure (Goble & Minch, 2018).

classification accuracy is the preparation of a classification error matrix (confusion matrix or contingency table). To prepare an error matrix first task is to locate ground reference test pixels or sample collection, based on which an error matrix is formed. The individual accuracy of the LULC types can be estimated using two approaches the producer's accuracy and user's accuracy in a similar manner. Producer's accuracy is a measure of the accuracy of a classification scheme and shows the percentage of a particular ground class that is correctly classified. It is calculated by dividing each of the diagonal elements in a confusion matrix by the total of each column respectively. The percentage of overall accuracy was calculated using accuracy assessment. 203 ground control point taken from google earth for the purpose of accuracy assessment.

Kappa Statistics

Kappa coefficient is another measurement used in this study. It is a discrete multivariate method of use in accuracy assessment. In classification process, where pixels are randomly assigns to classes will produce a percentage correct value (Tena et al., 2019). Obviously, pixels are not assigned randomly during image classification, but there are statistical measures that attempt to account for the contribution of random chance when evaluating the accuracy of a classification. The resulting Kappa measure compensates for chance agreement in the classification and provides a measure of how much better the classification performed in comparison to the probability of random assigning of pixels to their correct categories.

3.5 Tools used for SEBAL model

3.5.1 Geographic Resources Analysis Support System (GRASS GIS)

GRASS GIS and ArcGIS are both popular geographic information system (GIS) software packages used for spatial analysis and modeling. These unique features of GRASS GIS make it a powerful and flexible platform for estimating evapotranspiration using the SEBAL model, particularly when working with remote sensing data and conducting advanced spatial and temporal analysis.

Table 3. 3 Different software packages

No	Software tool	Description
1	ARC GIS 10.3	Calculating catchment areas, drawing slope maps, and defining watersheds.
2	ERDAS	a software package with raster architecture created especially for information extraction from images.
3	EXCEL	Spreadsheet editor software program, a powerful data visualization and analysis tool.
4	GRASS GIS	A free geographic information system (GIS) software used for geospatial data management and analysis image processing, producing graphics and maps, spatial and temporal modeling, and visualizing. It comes with a temporal framework for advanced time serious processing and Python API for rapid geospatial programming.
5	QGIS	Is free and open-source cross-platform desktop geographic information system application that support viewing, editing, and analysis of geospatial data
6	REF-ET	The REF-ET program provides standardized calculations of reference evapotranspiration1 (ET) by fifteen of the more common methods.

3.6 Surface Energy Balance Algorithm for Land (SEBAL) model

With the use of limited ground meteorological data and satellite spectral measurements, SEBAL calculates the spatial variation of hydro-meteorological parameters of LULC kinds. The surface energy balance terms, which control how heat and moisture are redistributed in soil and the atmosphere, are evaluated using these factors. Actual evapotranspiration (AET) is estimated by SEBAL as a residual term of the surface energy balance at the moment of satellite overhead. In this work, surface albedo, leaf area index, surface temperature, NDVI, SAVI, and evapotranspiration are among the hydrological parameters that SEBAL is utilized to predict. The basic requirements of this model is cloud-free Landsat 8 scene (LS8 -

OLI/TIRS) including MTL file for the year of 2022 and reflectance of each band and reproject all images including Digital Elevation Model (DEM) from ASTER UTM format. SEBAL consists of a set of tools for determining the land surface physical parameters, such as surface albedo, emissivity, surface temperature and vegetation index from spectral reflectance and radiance measurements. The SEBAL is method which assumes that temperature difference between the land surface and air-surface temperature varies linearly with land surface temperature and derives this relationship based on two pixels. The energy balance equation was used to calculate the level of evapotranspiration (Sun & Yong, 2019).

The net radiation (Rn) represents the actual radiant energy available at the surface. It was computed by subtracting all outgoing radiant fluxes from all incoming radiant fluxes. The first step in the SEBAL procedure is to compute the net surface radiation flux (Rn) using the surface radiation balance equation (Sattari, et al., 2021).

$Rn = (1-\alpha)RS\downarrow + RL\downarrow - RL\uparrow - (1-\varepsilon_o)RL\downarrow$ ……………………………..…………..…Equation 3.1

Where: $RS\downarrow$ is the incoming shortwave radiation (W/m^2), α is the surface albedo (dimensionless), $RL\downarrow$ is the incoming longwave radiation (W/m^2), $RL\uparrow$ is the outgoing longwave radiation (W/m^2), and ε_o is the surface thermal emissivity (dimensionless).

3.6.1 Calculation of Surface Radiation elements

The computer model number used for each computation is given along with the variable name. The two terms $RS\downarrow$ and $RL\downarrow$ are computed with a spreadsheet or a calculator rather than the Model Maker tool.

Surface Albedo (α)

Surface albedo is defined as the ratio of the reflected radiation to the incident shortwave radiation (Semaw et al., 2019). It is computed in SEBAL through the following steps:

$\alpha = \frac{\alpha TOA - \alpha path\_radiance}{\tau sw2}$ …..….....…………………………………………………….....Equation 3.2

Where; $\alpha_{path\_radiance}$ is the average portion of the incoming solar radiation across all bands that is backscattered to the satellite before it reaches the earth's surface, and ranged from 0.025 to

0.04 in SEBAL and 0.03 is recommended (Semaw et al., 2019). τ_{sw} is shortwave atmospheric transmissivity and calculated using the equation

$$\boldsymbol{\tau sw = 0.75 + 2 * 10^{-5} * Z} \text{……....………………...…….………………………. Equation 3.3}$$

Where z is an elevation of an area defined by ASTER GDEM Data (MDT_Sebal)

3.6.2 Vegetation indices

NDVI, LAI, and SAVI, are three widely used vegetative indices, are calculated using GRASS-SEBAL's reflectivity measurements. These indices are utilized as a function of land surface emissivity and surface temperature to determine the outgoing longwave radiation. Using visible and near-infrared bands, the Normalized Difference Vegetation Index (NDVI) and Leaf Area Index (LAI) will be computed. NDVI is a sensitive measure of the quantity and quality of green vegetation for Landsat-8. Negative NDVI values (-1 to 0) typically indicate water bodies or clouds, low NDVI values (0 to 0.1): NDVI values close to zero often represent barren or sparsely vegetated areas, such as deserts, bare soil, or rocky surfaces, Moderate NDVI values (0.1 to 0.5): NDVI values in this range typically represent areas with some vegetation cover, including grasslands, shrub lands, and agricultural fields, high NDVI values (0.6 and above): NDVI values above 0.6 usually indicate dense and healthy vegetation, such as forests or areas with thick vegetation cover (Yang et al., 2022).

$$\mathbf{NDVI} = [\frac{\mathbf{NIR-RED}}{\mathbf{NIR+RED}}] \text{ …..………………………………………………….……… Equation 3.4}$$

Where, RED= The red portion of the electromagnetic spectrum (0.6-0.7mm) and NIR=the near infrared portion of electromagnetic spectrum (0.75-1.5mm).

Soil adjustment Vegetation Index (SAVI) is an index that attempts to “subtract” the effects of background soil from NDVI so that impacts of soil wetness are reduced in the index (Ghosh, 2018). It is computed as:

$$\mathbf{SAVI} = [\frac{\mathbf{(1+L)(NIR-RED)}}{\mathbf{L+NIR+RED}}] \text{..…………………………………………….…………. ……Equation 3.5}$$

Where; L is a constant for SAVI. If L is zero, SAVI becomes equal to NDVI. A value of 0.5 frequently appears in the literature for L (Waters et al., 2002). Leaf Area Index (LAI), the ratio of the total area of all leaves on a plant to the ground area represented by the plant, was computed following the empirical equation by (Weng et al., 2004).

$$\mathbf{LAI} = -\mathbf{ln}\,\frac{\mathbf{(0.69 - SAVI)/0.59}}{\mathbf{0.91}} \text{ ……………………………….………………….Equation 3.6}$$

3.6.3 Emissivity and land surface temperature

Both surface emissivity (broadband and narrowband) were used for the calculation of the total longwave radiation emitted from the surface and surface temperature respectively (Waters et al., 2002). The values of emissivity were estimated from NDVI and LAI as follows:

$$\boldsymbol{\epsilon} = \mathbf{1.009} + \mathbf{0.047} * \mathbf{ln(NDVI)} \text{ ………………………….…….……..………….Equation 3.7}$$

Emissivity values range from 0 to 1, where 0 represents a perfectly reflective surface and 1 represents a perfectly emitting surface. The emissivity value for vegetation can be lower compared to non-vegetated surfaces.

$$\boldsymbol{\varepsilon}\mathbf{NB} = \mathbf{0.97} + \mathbf{0.0033} * \mathbf{LIA} \text{ …..……………………………..……..……………Equation 3.8}$$

$$\varepsilon 0 = 0.95 + 0.01 \times LAI \text{ ………………………………..…………..……………Equation 3.9}$$

Where LAI < 3, When LAI >= 3; ε (emissivity) = 0.98 (Taghi Sattari, et al., 2021)

For water, NDVI < 0 and surface albedo < 0.47, ε0 = 0.985 and εNB = 0.99 (Waters et al., 2002) for snow, NDVI < 0 and surface albedo >= 0.47, ε0 = 0.985 and εNB = 0.99(Waters et al., 2002)

For this calculation, NDVI, LAI, and surface albedo are input parameters to compute emissivity in both cases. Hence, computation is done using GRASS GIS & python. The black body temperature which means idealized object that absorb all incident radiation without reflecting or transmitting any of it was corrected with respect to the surface emissivity (ε) values to compute the land surface temperature (Ts) using the formula given by (Weng et al., 2004).

$$\mathrm{Ts} = \frac{\mathrm{tb}}{1+\left(\lambda+\frac{\mathrm{tb}}{\gamma}\right)*\ln\varepsilon\mathrm{NB}}] \text{ ……………….…………………………………….……………Equation 3.10}$$

Where: λ is the average of limiting wavelengths of band 10 of Landsat8-TIRS (central wave length of approximatly10.8micrometers)

The choice of band 10 in SEBAL is based on the fact that it corresponds to the atmospheric window in the thermal infrared spectrum.

$\gamma = h \times c / a(0.01438m.K)$ …….…………….……………………..……………Equation 3.11

$\gamma = 14380$

a = Boltzmann constant ($1.38x10^{-23}$j.k)

h = Plank's constant ($6.626x10^{-34}$ J.s)

c = velocity of light (2.998×10^{8} m/s)

3.6.4 Calculation of Solar Radiations Elements and ET

The solar radiation and ET were computed following the procedure set by (Bastiaanssen et al., 2005). Incoming shortwave radiation (RS↓) (W/m^2) will be calculated using the available climatic parameters (sunshine hours, relative humidity, minimum and maximum temperature, and geographic location), the solar constant, the solar incidence angle, a relative earth-sun distance, and the calculated atmospheric transmissivity. It is calculated, assuming clear sky conditions, as a constant for the image time Sattari, et al., 2021).

$Rs \downarrow = G_{Sc} * \cos\theta * d_r * \tau_{sw}$ ……………………………………………………………………………..…Equation 3.12

Here, dr stands for the inverse squared relative earth-sun distance, θ is the solar incidence angle, = sun elevation angle, and τ_{sw} is the atmospheric transmissivity. GSc is the solar constant (1,367 W/m^2).

The outgoing longwave radiation (RL↑) was computed at each pixel using the Stefan-Boltzmann equation (W/m^2) (Eq. 18) with a calculated surface emissivity and surface temperature (Waters et al., 2002). This calculation is done using GRASS-GIS SEBAL Python.

$\boldsymbol{RL\uparrow = \epsilon 0} * \sigma * \boldsymbol{Ts^4}$……………………..……………………………………….………Equation 3.13

Where ε_0 is the broadband surface emissivity, σ is Stefan-Boltzmann constant (5.67×10^{-8} $W/m^2 / K^4$) and Ts is surface temperature in K.

Choosing the "Hot" and "Cold" Pixels

Two "anchor" pixels are used by the SEBAL procedure to set boundary constraints for the energy balance. These pixels are situated in the area of interest and are referred to as "hot" and "cold." A wet, well-irrigated crop area with complete ground cover by vegetation is designated as the "cold" pixel. At this pixel, it is believed that the surface temperature and the air temperature close to the surface are similar. An arid, barren agricultural field with ET set to zero is chosen as the "hot" pixel. Net radiation flow was computed using surface albedo (α), outgoing longwave radiation (RL↑), broadband surface emissivity (ε0), incoming shortwave radiation (RS↓), and incoming longwave radiation (RL↓).

3.6.5 Calculation of surface energy budget elements

Soil heat flux (G) and sensible heat flux (H) were computed in SEBAL using the surface energy budget equation.

Soil heat flux (G)

Earth's subsurface is heated by radiant radiation, which is its primary application. Conduction is the process by which heat moves from the surface downward. Heat transfer requires the presence of a temperature difference between the surface and the subsurface, much like in the case of sensible heat transfer. When the surface is warmer than the subsurface, heat is transmitted downward (positive ground heat flux). Heat moves upward when the subsurface temperature is higher than the surface temperature (negative ground heat flux). It is the rate at which heat is stored in the soil as a result of the temperature differential between the soil's surface and its upper underlying layers (W/m^2) (Laipelt et al., 2020). It is calculated using the equation given below:

$$\mathbf{G/Rn = Ts/\alpha(0.0038\alpha + 0.0074\alpha^2)(1 - 0.98NDVI)} \text{……….……………Equation 3.15}$$

Where Ts = the surface temperature (^{0}C), α = the surface albedo (Eq. 7), NDVI = the Normalized Difference Vegetation Index, G is then readily calculated by multiplying G/Rn by the value for Rn computed in the above equation.

The ratio of G/Rn was assigned equal to 0.5 for the condition of NDVI < 0; Ts< 4 ^{0}C and α > 0.45. The resulting image was converted to soil heat flux (G) in W/m^2 by multiplying the ratio G/Rn by Rn (Waters et al., 2002).

Sensible Heat Flux (H)

Sensible heat flux is the amount of heat energy that is transported from the air to the surface when their temperatures differ, allowing for surface heating without the loss of liquid. Positive sensible heat transfer occurs when heat is transmitted upward into the air from a surface that is warmer than the air above. Heat transmission causes the surface to cool but the air to rise in temperature. Heat is transmitted from the air to the surface if the air is warmer than the surface, resulting in a negative sensible heat transfer. The air cools and the surface warms if heat is lost from the air. When the sun sets and no longer emits sunlight, this scenario could occur at night. The air just above the surface is warmer at this moment, and the earth is cooling as a result of long wave emission. It is the speed at which heat is lost to the air as a result of temperature gradients through convection and conduction (Laipelt et al., 2020). It was computed using the following equation

$H = (\rho \times c_p \times dT)/r_{\alpha h}$ .... Equation 3.16

Where:

H = sensible heat flux,

ρ = air density (kg/m^3),

Cp = air specific heat (1004 J/kg/K),

dT = near surface temperature differences (T1-T2) in K between two heights (Z1 & Z2) above the zero plane displacement

rah = aerodynamic resistance to heat transport (s/m).

Latent heat flux (λET)

The process via which a liquid phase turns into a gas is called evaporation. It is designated as "latent" because the water molecules are reserving it for when condensation occurs. We cannot sense or experience latent heat since it does not increase the temperature of the water The residual technique can be used to estimate E if the second order reliance of r a on this gradient is ignored. This suggests that ET is linearly related to the surface air temperature differential at the time of Ts measurement. It is the speed at which latent heat is released from the surface due to evapotranspiration (Sun & Yong, 2019). It will be computed for each pixel using Equation 21.

$$\lambda ET = Rn - G - H \quad \text{……………………………………………………………Equation 3.17}$$

Where: λ ET is an instantaneous value for the time of the satellite overpass (W/m^2). Instantaneous value of ET in equivalent evaporation depth was computed as:

$$\mathbf{ETins = 3600\frac{\lambda ET}{\lambda}} \quad \text{……………………………………………………….Equation 3.18}$$

Where: ET_{inst} is the instantaneous ET (mm/hr), 3600 is the time conversion from seconds to hours, and λ is the latent heat of vaporization or the heat absorbed when a kilogram of water evaporates (J/kg)

The Reference ET Fraction (ETrF) is defined as the ratio of the computed instantaneous ET (ETinst) for each pixel to the reference ET (ETr) computed from weather data (Sattari, et al., 2021).

$$\mathbf{ETrF = \frac{ETinst}{ETr}} \quad \text{…………………………………………………………...Equation 3.19}$$

where; ETinst is from Equation (mm/hr) and ETr is the reference ET at the time of the image from the REF-ET software (mm/hr). ETrF is similar to the well-known crop coefficient, Kc. ETrF is used to extrapolate ET from the image time to 24-hour or longer periods.

ETr was used in SEBAL to estimate the ET at the "cold" pixel and to calculate the reference ET fraction (ETrF) and ETr was computed for a given weather station using the REF-ET software (Copyright & Allen, 2000).

3.7 24-Hour Evapotranspiration (ET24) in SEBAL

SEBAL computes the ET24 by assuming that the instantaneous ETrF computed in model is the same as the 24-hour average. Daily values of ET (ET24) were often more useful than instantaneous ET (Semaw et al., 2019). Finally, the ET24 (mm/day) can be computed as:

$$ET24 = ETrF \times ETr_{24} \quad \text{Equation 3.20}$$

where; ETr-24 is the cumulative 24-hour ETr for the day of the image. This is calculated by adding the hourly ETr values over the day of the image.

The evapotranspiration map that covers a season/month of full growth was derived from the 24-hour evapotranspiration data by extrapolating the ET24 proportionally to the reference evapotranspiration (ETr). To compute the cumulative ET for each period as follows:

$$\mathbf{ETperiod} = \mathbf{ETrFperiod} \sum \mathbf{n}\ \mathbf{ETr}\ \mathbf{24} \quad \text{Equation 3.21}$$

where; ETrFperiod is the representative ETrF for the period, ETr-24 is the daily ETr, and n is the number of days in the period. W/m^2 for ETperiod will be in mm when ETr-24 is in mm/day. The next step is to compute the seasonal ET by summing all of the ETperiod values for the entire year as well as length of the season.

3.8 Ground based ET calculation

The United Nations Food and Agriculture Organization (FAO) method (Odusanya et al., 2019) defines reference evapotranspiration (ETo) as the evapotranspiration from a reference crop with crop height of 0.12 m, which is actively growing and adequately watered. It has a surface roughness of 70 (s m-1) and an albedo of 0.23. The latent heat flux of this reference surface is estimated according to the Penman–Monteith equation. The data include elevation, latitude and longitude of the station, total monthly rain, maximum and minimum air temperature, relative humidity, wind speed at 2 m height, and daily sunshine hour. The ETo values were calculated using weather dataset using the Penman-Monteith equation by using REF-ET software mentioned in the previous section (Bastiaanssen et al., 2005).

3.8.1 REF-ET

REF-ET requires accurate and reliable meteorological data, including temperature, humidity, solar radiation, wind speed, and atmospheric pressure. The data prepare in excel and saved in comma delimited format. The altitude, the anemometer height, longitude and latitude of the study area was input for the software.Interface and theoutput present in figure 7.1 and 7.2 in Appendices. These parameters are crucial for calculating evapotranspiration. High-quality meteorological data from reliable sources, such as weather stations, is essential to ensure accurate estimations (Allen, 2016).

3.9 Model Comparison and calibration

Root Mean Squared Error (RMSE)

RMSE measures the square root of residuals and measures the accuracy of PET estimates:

$RMSE = \sum((Si- Ri)^2/n)^{1/2}$ ……………………………..…………….……....Equation 3.22

Where:

S_i represents the observed or actual values.

R_i represents the predicted values.

Σ represents the sum of the squared differences between observed and predicted values.

n represents the total number of observations.

3.9.2 Model calibration

The present study aims to calibrate the model by satellite-based products of evapotranspiration. Calibration and validation could be done because the RS-derived ET could not be evaluated by station-observed data directly because the difference of the scale. Linear regression method Regression analysis is conducted to examine the relationships of the monthly evapotranspiration extracted from RS with the monthly values calculated by the FAO-PM method (López et al., 2017). By using daily evapotranspiration from the estimated SEBAL output and the daily evapotranspiration calculated from Penman-Monteith equation we compute regressions equation.

Regression analysis was conducted to examine the relationships of the monthly evapotranspiration estimates from the three empirical equations with the monthly values calculated by the FAO-PM method (Biru & Kumar, 2017). The linear regression equation is given by

ETopm = mETosebal + C……………………………………….…………..Equation 3.23

Where; ETopm computed by FAO-PM, ETosebal is ETa estimated from SEBAL model, m and c = constants representing the slope and intercept of the regression equation, respectively.

Coefficient of determination R^2 and standard error were determined in the analysis. The coefficient of determination R^2 is a measure of accuracy or the degree to which the measured and predicted values agree. Here the regression method measures the degree of relationships existing between the FAO-PM ETa estimates and the SEBAL model.

3.9 Research design flow chart

The main phases of this study include: Downloading sentinel image, and by referring this image with Sentinel image we can classify the land use land cover. Landsat 8 preprocessing, supervised classification, accuracy assessment, pre-and post- processing for SEBAL model. From figure 3.3 below rah represent aerodynamics resistance to heat resistance, a, and b slope and intercept respectively for the relationship between surface temperature and vapor pressure.

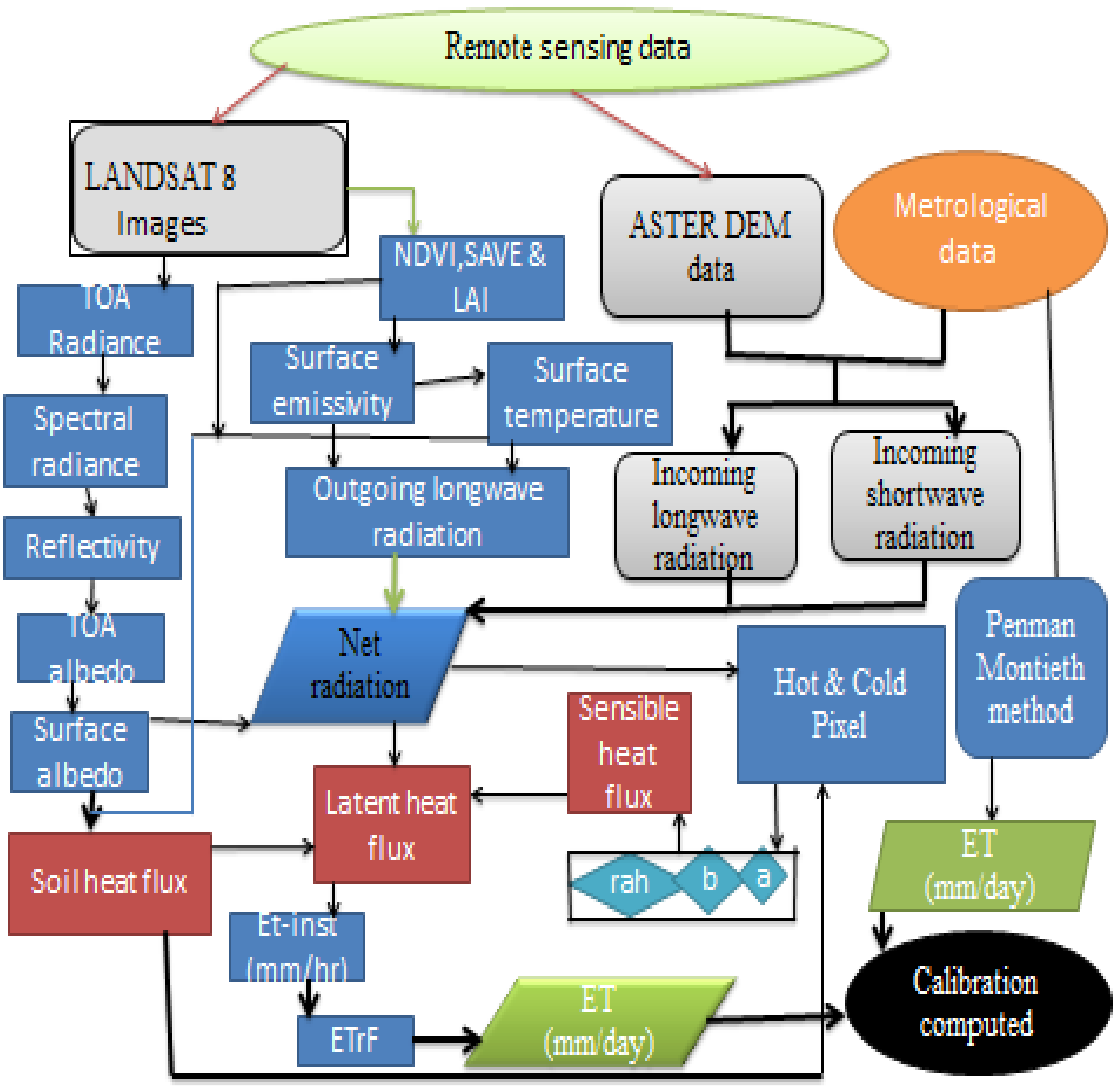

Figure 3. 4 The conceptual scheme for the research design

4. RESULTS AND DISCUSION

4.1 Land use land cover (LULC) maps

Satellite images were classified with the help of a supervised classification method and land use and land cover maps were produced for the Mojo watershed for the years 2022. (Figure 4.1). 278 training sample(polygon) have been used for the use of supervised classification.

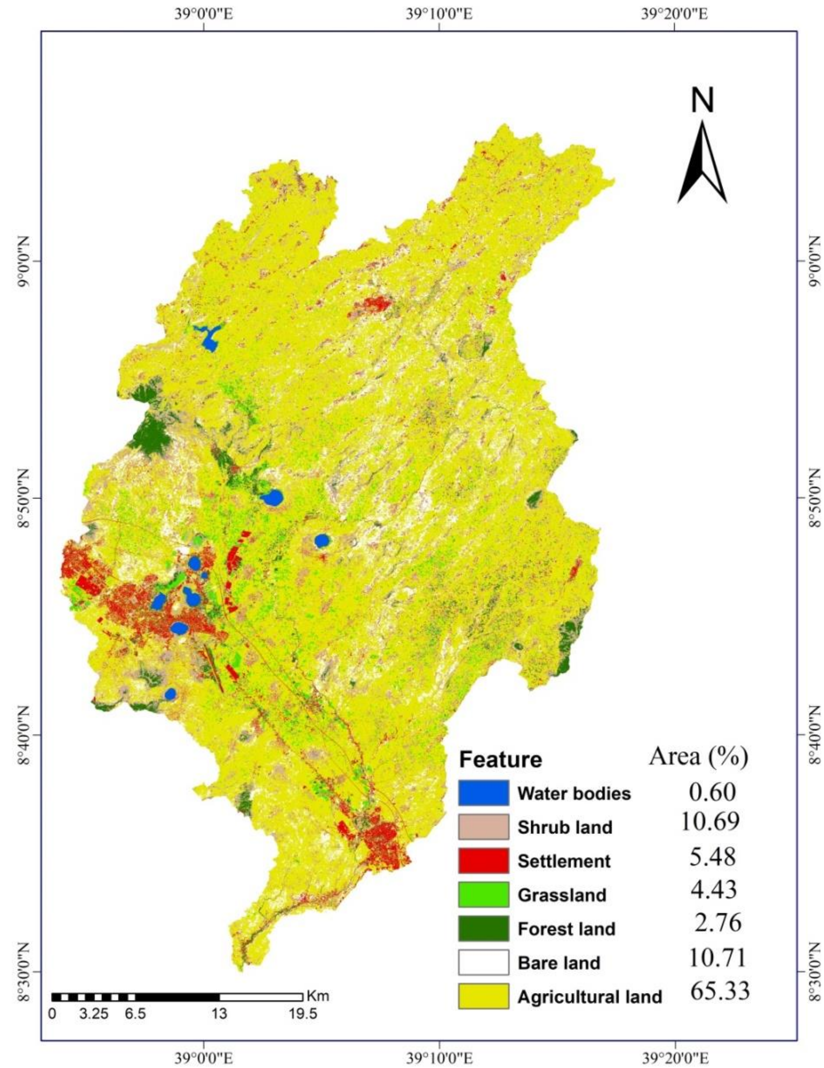

Figure 4. 1 Land use and land cover map of the Mojo catchment for the 2022 period

The classification yielded seven land cover classes and the area covered by agricultural land was 1044.77 km^2, accounting for 65.33% of the total catchment area, urban land covered an area of 87.578 km^2, representing 5.48% of the catchment, shrub land occupied 170.91 km^2, accounting for 10.69% of the total area, grassland occupied 70.9078 km^2, making up 4.43% of the total area, bare land occupied 171.2019 km^2, representing 10.71% of the total area., Water bodies covered 9.6548 km^2, which accounted for 0.60% of the land and forest land Forest land covered 44.1801 km^2, which accounted for 2.76% of the catchment. Note that the water bodies' cover is considerable low in mojo catchment

4.1.2 Accuracy assessment for the land use land cover map

The output of accuracy assessment suggest that the land-use land-cover map for the Mojo catchment demonstrated a high level of accuracy & and attained by the previous studies. For instance (Kiros et al., 2015). For accuracy assessment from google earth 203 reference point (placement) have been used for the used.

Table 4. 1 Error matrix for LULC in the Mojo Catchment, for the 2022 period

	Reference data								
Classified data	Water bodies	Urban land	Shrub land	Agricultural land	Bare land	Forest land	Grass land	Total	User accuracy
Water bodies	17	0	1	1	0	0	0	20	85%
Urban land	0	27	0	2	1	0	0	30	90%
Shrub land	0	1	17	0	0	3	0	21	81%
Agricultural land	0	0	0	56	2	0	2	60	93%
Bare land	0	0	0	6	24	0	0	30	80%
Forest land	0	0	4	0	0	18	0	22	82%
Grass land	0	0	0	2	1	0	17	20	85%
Total	17	28	22	67	28	21	19	203	
Producer's accuracy	100%	96%	77%	84%	86%	86%	89%		
Overall Classification Accuracy = 86.7%									
Overall Kappa Statistics = 84%									

Grassland category achieved a producer's accuracy of 89%, indicating that the majority of grassland areas were correctly identified on the map. Water bodies attained a perfect producer's accuracy of 100%, indicating accurate identification of all water bodies in the catchment. The bare land category exhibited a producer's accuracy of 86%, suggesting a good level of accuracy in identifying bare land areas. shrub land achieved and 77% producer's accuracy, indicating that most shrub land areas were correctly classified. Forest land demonstrated perfect accuracy, with a producer's accuracy of 86%, implying good identification for most forested areas. urban land attained a producer's accuracy of 96%, suggesting a relatively high level of accuracy in identifying urbanized areas. agricultural Land, the largest category, achieved a producer's accuracy of 84%, indicating accurate identification of the majority of agricultural land parcels.

The overall classification accuracy of 86.7% implies that the land-use land-cover map as a whole was highly accurate. This means that, on average, 86.7% of the land-use and land-cover classes were correctly classified. The value of 13.3% represents the proportion of misclassified land-use land-cover classes in the overall classification. This high level of accuracy is further supported by the overall kappa statistics of 0.84, which indicates a substantial agreement between the classified map and the reference data. K values greater than 0.8 represent strong agreement, K values which range from 0.61 to 0.80 represents moderate agreement, between 0.21 and 0.40 suggest slight or weak agreement, K values less than 0.2 indicate poor agreement or no agreement. The overall kappa coefficient achieved for this study was 0.84, which represent a strong agreement (i.e. greater than 0.8) between the classified LULC.

4.2 Reference evapotranspiration ETr

4.2.1 Instantaneous wind speed and ETr calculation

timage (Local Time) = GMT + Correction…………………………………….….Equation 4.1

Table 4. 2 Calculation of Satellite overpass time in local standard time

No	Image Overpass Date	Image Overpass Time	Correction	t image Local time (hour min sec)	t image Local time (Hour)

1	24/1/2022	07:40:34 GMT	+3	10:40:34 AM	10.67 hr
2	9/2/2022	07:40:25 GMT	+3	10:40:25 AM	10.67 hr
3	13/3/2022	07:40:21 GMT	+3	10:40:21 AM	10.67 hr
5	23/10/2022	07:40:59 GMT	+3	10:40:59 AM	10.68 hr
6	08/11/2022	07:41:01 GMT	+3	10:41:01 AM	10.68 hr
7	10/12/2022	07:40:56 GMT	+3	10:40:56 AM	10.68 hr

Determine the weather time periods to use for interpolation. Quite likely, the weather parameter for the instantaneous image time will need to be interpolated from averages representing two time periods. A general formula to determine which time periods to use in the interpolation is the following (Waters et al., 2002).

$$\boldsymbol{t_1} = \mathbf{int}\left[\frac{\mathbf{t_{image(Local\ time)}}}{\Delta \mathbf{t}} + \frac{\mathbf{1}}{\mathbf{2}} - \mathbf{Flag_{Period}}\right]\Delta \mathbf{t} + \mathbf{Flag_{DST}} \quad \text{Equation 4.2}$$

$$\mathbf{t_2} = \mathbf{t_1} + \Delta \mathbf{t} \quad \text{Equation 4.3}$$

where; t1 = time identifier for the first weather period in hours t2 = time identifier for the second weather period in hours Δt = length of weather period in consistent with t1 and t2 in hour, t_{image} (local time) = the satellite image time (local time, with no adjustment for daylight savings)

$Flag_{period}$ = a flag for the way that the weather data period is represented by its "time label". $Flag_{period}$ = 0 if the time label is the endpoint of the weather data period; = 1 if the time label is the beginning of the weather data period; = 0.5 if the time label represents the midpoint of the weather data period.

$Flag_{DST}$ = a flag for use of DST in the weather data set. $Flag_{DST}$ = 0 if no DST is used and $Flag_{DST}$ = 1 hour if DST is used in the weather data set.

Estimate the instantaneous wind speed applying a simple linear interpolation assumption. For interpolation of data we assume that the averages for the periods represent measurements occurring at the midpoints of the periods. A general interpolation formula based on the t1 and t2 period identifiers from Eq. 31 & 32.

$$\mathbf{Data_{image}} = \mathbf{data1} + \frac{(\mathbf{Data_{t2}} - \mathbf{Data_{t1}})}{\Delta \mathbf{t}} \left[\mathbf{t_{image\ (Local\ time)}} - \left(\mathbf{t1} - \mathbf{Flag_{Period}} + \Delta \mathbf{tFlag_{Period}} - \frac{\Delta \mathbf{t}}{\mathbf{2}} \right) \right] \quad \text{Equation 4.4}$$

where; Datat1 = the average value for the specific data parameter (i.e., wind or ETr) for the t1 time period , Datat2 = the average value for the specific data parameter (i.e., wind or ETr) for the t2 time period. For this weather data, DST was not applied and the time identifier (label) for the weather data represented the midpoint of the data period ($Flag_{DST}$ = 0, $Flag_{period}$ = 0.5). Δt = 1 hour. Therefore, t1 and t2 are calculated as:

Table 4. 3 Calculated of reference evapotranspiration, instantaneous evapotranspiration and wind speed values.

Month	Time1	Time2	EToi(mm/hr)	ETo(mm/day)	ETr(mm/day)	Wind speed(m/s)
January	10	11	0.38	3.73	5.01	2.98
February	10	11	0.35	4.42	5.91	2.17
March	10	11	0.36	4.7	6.43	2.80
October	10	11	0.34	3.65	4.99	2.51
November	10	11	0.32	3.27	4.26	2.40
December	10	11	0.34	3.45	4.63	2.72

The Mojo catchment's surface albedo values for the six-month period (Oct-Mar) ranged from 0.02 to 0.97. High albedos reflect more solar radiation, reducing energy absorption and resulting in lower surface temperatures. This can affect evapotranspiration. The values reveal the reflectivity of different land cover types, revealing the region's energy balance and climate dynamics during that period. In October, the albedo values for grassland ranged from 0.02 to 0.51, with a mean of 0.16 and a standard deviation of 0.04. Water bodies had a range of 0.03 to 0.47, with a mean of 0.12. In November, the albedo values for grassland slightly increased, with a range of 0.88.

4.3 Surface radiation balance

4.3.1 Surface albedo

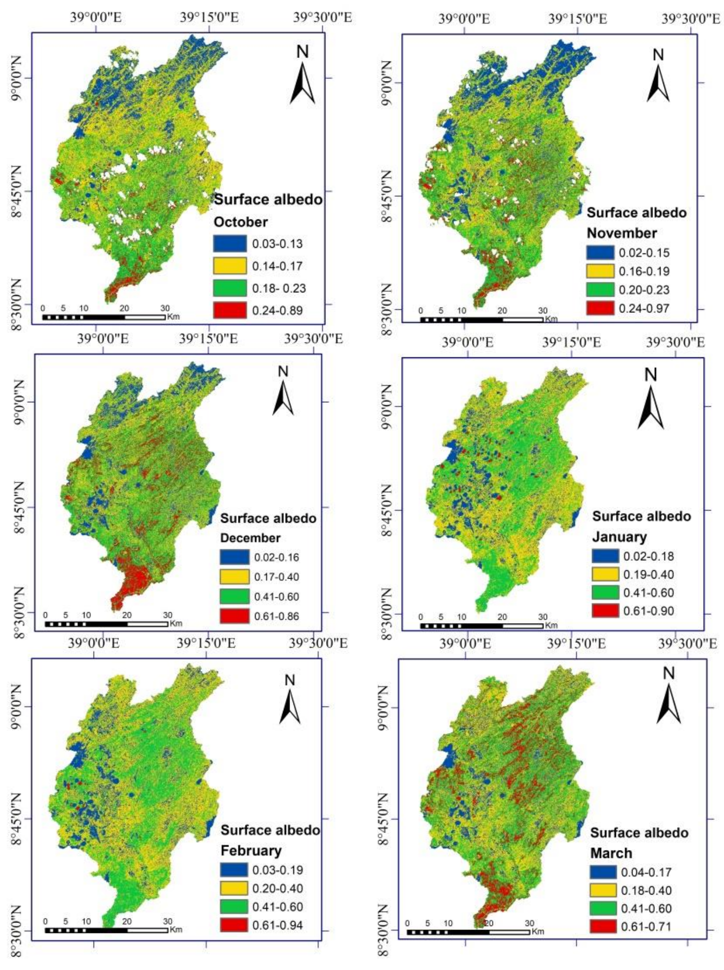

Figure 4. 2 Map of surface albedo

The albedo values of water bodies and grassland were similar in January and February, with slight variations. In December, the albedo values for grassland reached a maximum of 0.49, while water bodies had a range of 0.35. By March, the albedo values for grassland reached a minimum of 0.51, while water bodies had a range of 0.37. The other land-use land-cover classes showed similar trends see figure 7.3 in appendixces. The albedo values of various land-use land-cover classes fluctuated over a six-month period, influenced by changes in vegetation cover, surface conditions, and solar radiation, which aids in understanding the catchment area's energy balance and climate dynamics.

4.3.2 Incoming short wave radiation

The images show the incoming short wave radiation (RSI) for the Mojo catchment from October to March. This energy, also known as solar radiation, is crucial for evapotranspiration, the process of water evaporation from the land surface and transpiration by plants. The RSI values can range from 200 to 1000 W/m^2, depending on the time and location of the image (Teshome et al., 2015). The RSI values in October, November, December, January, February, and March were recorded. The minimum RSI was 849.60 w/m^2, the maximum was 976.14 w/m^2.. In January, the range narrowed to 849.60 and 881.96 w/m^2, while in February, it slightly increased to 908.68 w/m^2. In March, it fluctuated between 934.72 and 970.32 w/m^2. Short wave radiation variations are influenced by factors like latitude, time of year, cloud cover, and atmospheric conditions. As longitude increases, the RSI pattern gradually increases, suggesting higher levels of radiation in locations with higher longitudes. Shortwave radiation values remain consistent across different land classes and months, likely due to similar solar angles and weather conditions (Figure 7.4 in Appendices). The consistency in seasonality leads to similar shortwave radiation values across different land classes. Geographic locations with similar latitudes experience similar solar radiation patterns, with regions receiving similar amounts and patterns throughout the six-month period.

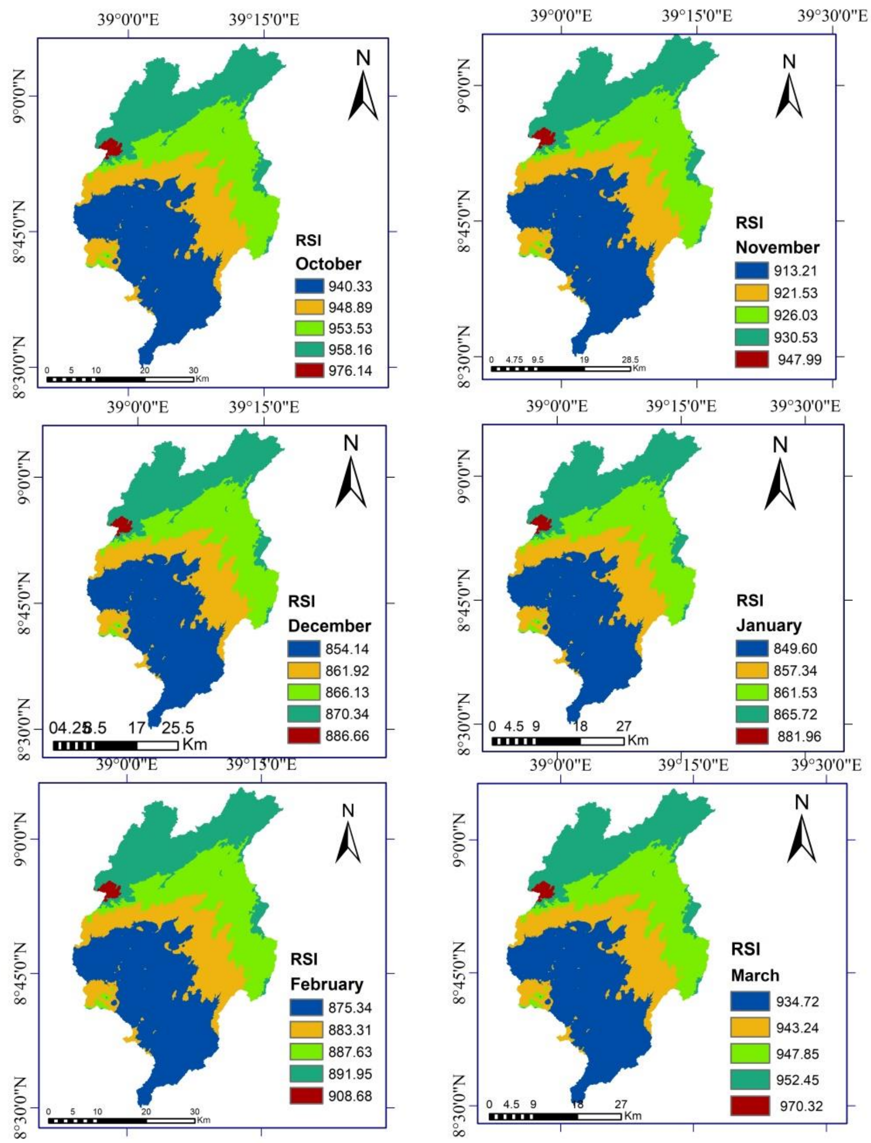

Figure 4. 3 Map of incoming short wave radiation

4.3.3 Outgoing longwave radiation

Outgoing long wave radiation (RLO) is the energy emitted by Earth's surface and atmosphere in the form of infrared radiation, crucial for the Earth's energy balance. Higher surface temperatures result in greater RLO, with values ranging from 200-700 W/m^2 depending on the location and time of the image (Hashem et al., 2020). The Mojo catchment experiences varying levels of RLO during different months, with some months experiencing lower levels and others experiencing higher levels. The Mojo catchment's outgoing long wave radiation (RLO) values from October to March showed a decrease in the minimum value of 361.77

w/m^2 in October and a maximum of 512.1 w/m^2 in March. This indicates a lower amount of radiation from Earth's surface and atmosphere, with a higher peak in October.

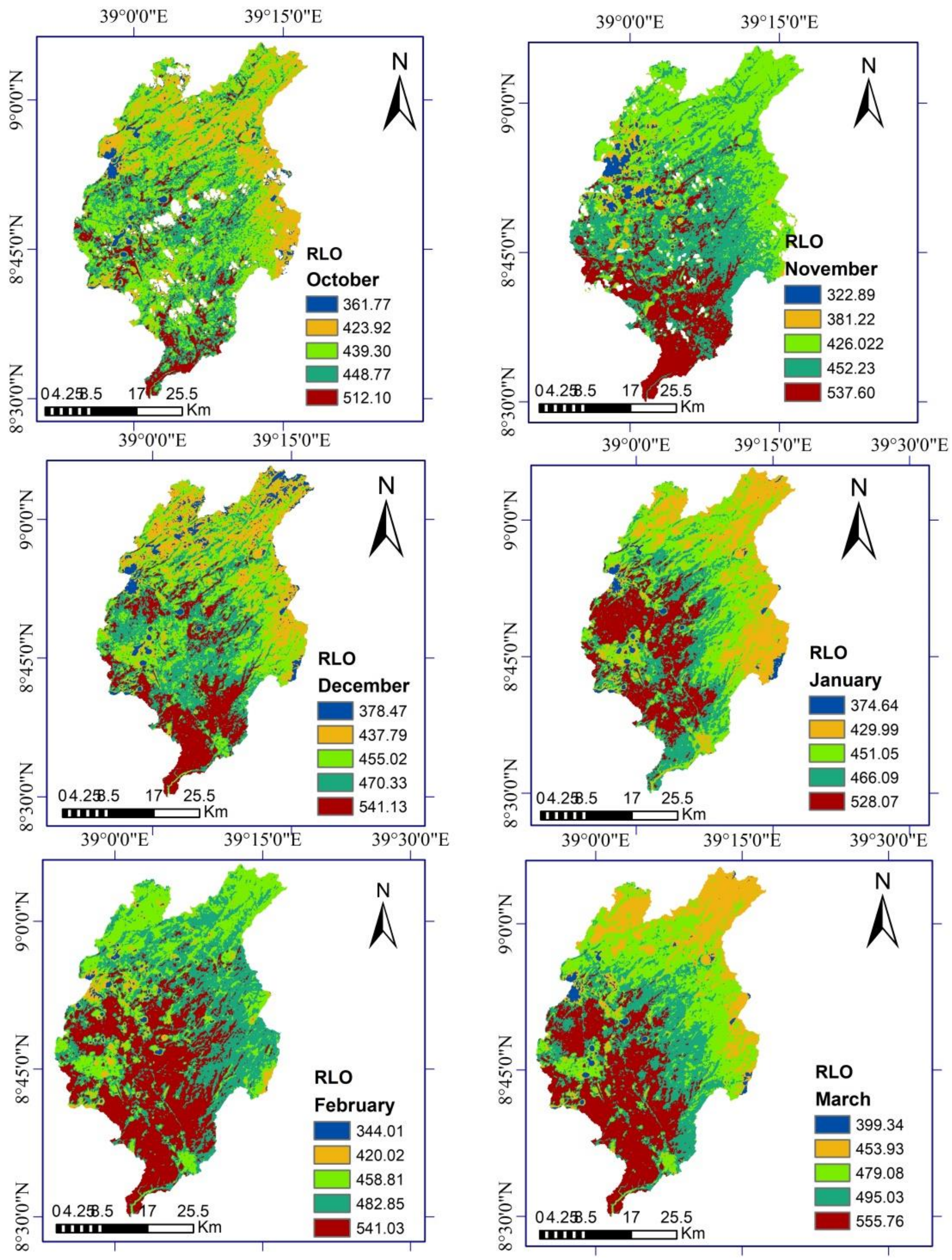

Figure 4. 4 Map of outgoing longwave radiation

In November, the minimum value decreased to 322.89 w/m^2, indicating a decrease in long wave radiation emissions. The maximum Rlo value in December increased significantly to 537.6 w/m^2, indicating higher radiation levels. December saw an increase in both minimum and maximum Rlo values, with the minimum reaching 378.47 w/m^2 and the maximum reaching 541.13 w/m^2, indicating a higher peak of radiation. January's Rlo values remained consistent, with the minimum at 374.64 w/m^2 and the maximum at 528.07 w/m^2. The data shows a stable emission of long wave radiation from January to March. In February, the minimum Rlo was 344.01 w/m^2, indicating a slight reduction in radiation. The maximum Rlo was 541.03 w/m^2, remaining consistent. In March, the minimum Rlo increased to 399.34 w/m^2, indicating a higher level of radiation. The maximum Rlo reached 555.76 w/m^2, indicating a higher peak. The values of RLo vary with different land use features (figure 7.5 in Appendices).

4.3.4 incoming long wave radiation (RLI)

The images provides the minimum and maximum values of incoming long wave radiation (RLI) for the Mojo catchment from October to March. Incoming long wave radiation (RLI) refers to the energy received by the Earth's surface and atmosphere in the form of long wave (infrared) radiation from various sources, including the atmosphere itself and the Earth's surface. The relationship between incoming longwave radiation (RLI) and evapotranspiration is indirect but interconnected through the surface energy balance and atmospheric processes. Values for RLI can range from 200 – 500 W/m^2, depending on the location and time of image (Waters et al., 2002). The Mojo catchment experienced a minimum and maximum RLI of 337.92 w/m^2 in October, indicating a lower amount of long wave radiation from the atmosphere and Earth's surface. The maximum RLI of 342.97 w/m^2 indicates a slightly higher peak of radiation, indicating a The maximum RLI of 342.97 w/m^2 indicates a slightly higher peak of radiation, indicating a.greater amount of infrared energy being received.

In November, the RLI values decreased compared to October, with a minimum of 326.84w/m^2 and a maximum of 331.7w/m^2. December saw an increase in both minimum and maximum RLI values, with a minimum of 342.65w/m^2 and a maximum of 347.77w/m^2, indicating a

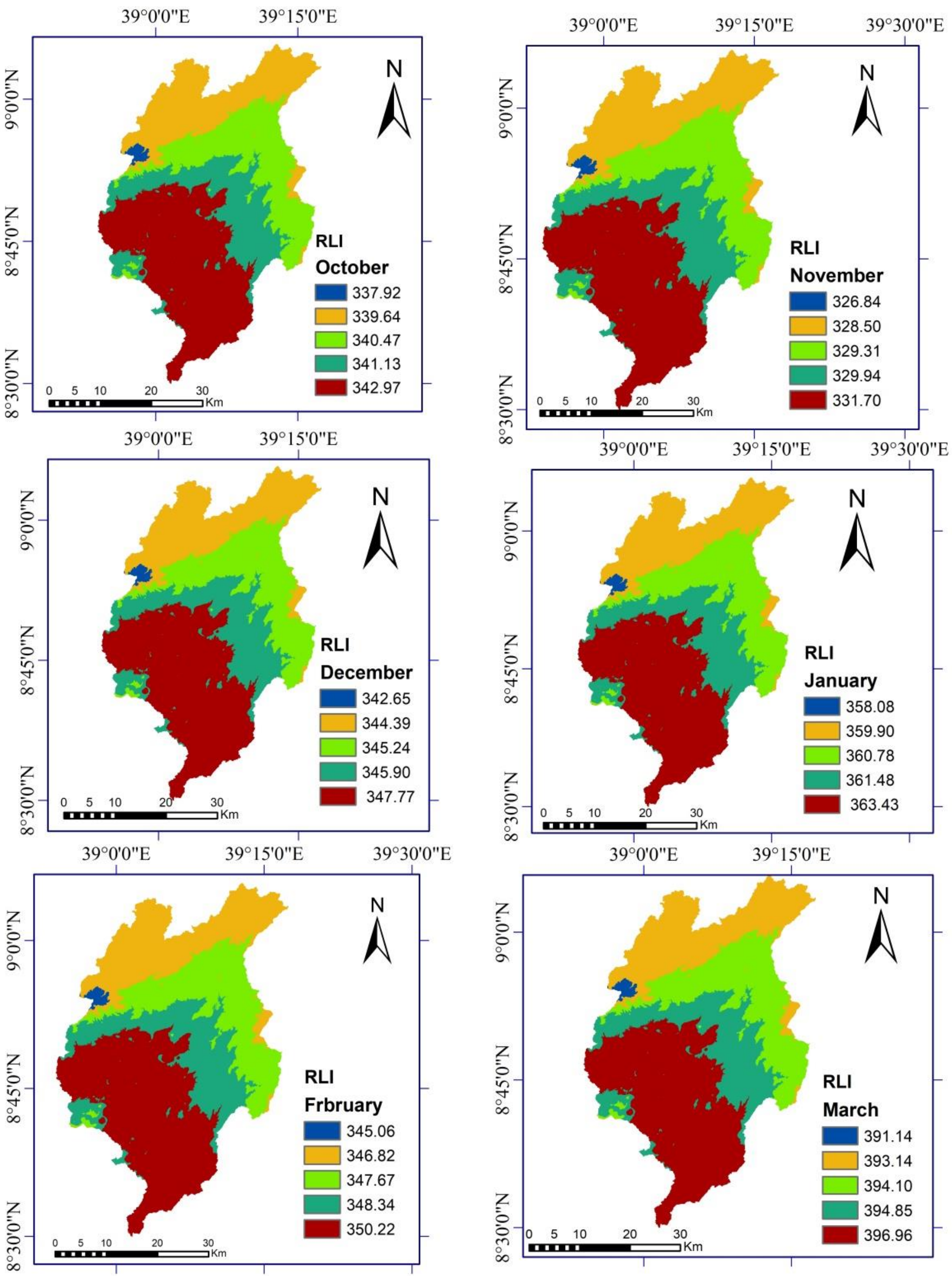

Figure 4. 5 Map of Incoming longwave radiation

higher level of radiation. In January, the RLI values continued to increase, with a minimum of 358.08 w/m^2 and a maximum of 363.43 w/m^2. The RLI values showed a rise in long wave radiation during the period. In February, the minimum RLI was 345.06 w/m^2, while the maximum reached 350.22 w/m^2. In March, the minimum RLI rose to 391.14 w/m^2, and the maximum reached 396.94 w/m^2, indicating a higher peak of radiation due to high temperatures. The values of RLI varied with different land use features (figure 7.12 in Appendices).

4.3.5 Net surface radiation

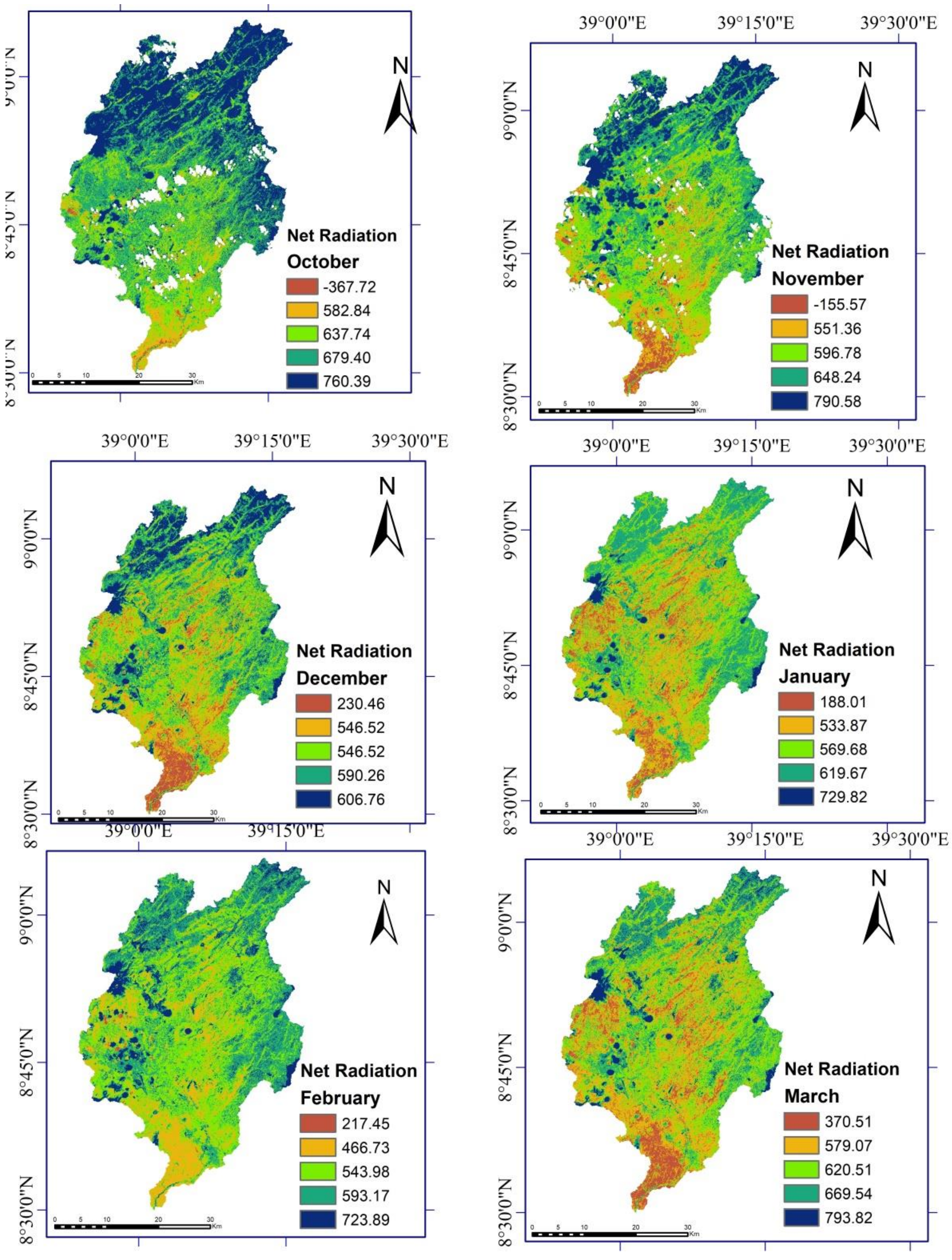

Figure 4. 6 Map of Net Radiation

The provided images present net radiation values for the Mojo Catchment from October to March, a crucial part of the Earth's energy budget. Higher values indicating greater energy input and higher evapotranspiration rates. In October, the minimum net radiation value was --367.72 w/m^2, indicating a net loss, while the maximum was 760.39 w/m^2, indicating a net gain. The mean net radiation for October was 677.3 w/m^2. In November, values ranged from -155.57 to 790.58 w/m^2, with a mean of 618.88 w/m^2. In December, values varied from 20.46 to 606.76 w/m^2. In January, the range was from -11.01 to 729.82 w/m^2, with a mean of 569.54 w/m^2. In February 217.54 to 723.89 w/m^2. In March, the range was between 370.51 and 79.82 w/m^2. The net radiation values over a six-month period. The mean net radiation provides an average monthly energy balance, while negative values in some months suggest a cooling effect. The value of net radiation varies with different land use features. have been discribed in (figure 7.8 in Appendices).

4.4 Vegetation indices

4.4.1 Normalized difference vegetation index (NDVI)

The NDVI values for images from October to March showed spatial variation ranging from -0.61 to 0.86. These values are used to assess vegetation density and health, with higher values indicating higher potential evapotranspiration rates. In October, the NDVI values were -0.52 to 0.86, with negative values indicating little or no vegetation and positive values indicating vegetation presence. See figure 4.7 below. The NDVI values in the catchment showed a diverse vegetation condition, with some areas having sparse or unhealthy vegetation and others exhibiting denser and healthier vegetation. In November, NDVI value was 0.61-0.85 the range was narrower, indicating a more consistent vegetation condition. In December, the range narrowed, indicating a convergence of vegetation conditions, with positive values dominating, indicating the presence of vegetation in most areas (Semaw et al., 2019). The areas along with the river (water body) represent a low vegetation index of ranges from 0.14 to 0.22 whereas, forest areas showing high vegetation density recognized by higher average values of NDVI ranges from 0.6 to 0.65 (Jane et al., 2016). The NDVI values in January, February, and March showed varying levels of vegetation presence. In January, the range was -0.49 to 0.83, with most areas showing positive values. In February, the range was -0.36 to 0.76, with -0.36 indicating non-vegetated areas and 0.76 indicating dense vegetation. In

March, the range was -0.26 to 0.79, indicating stable vegetation conditions. NDVI value for different land use feature have been discribed in (figure 7.6 in Appendices).

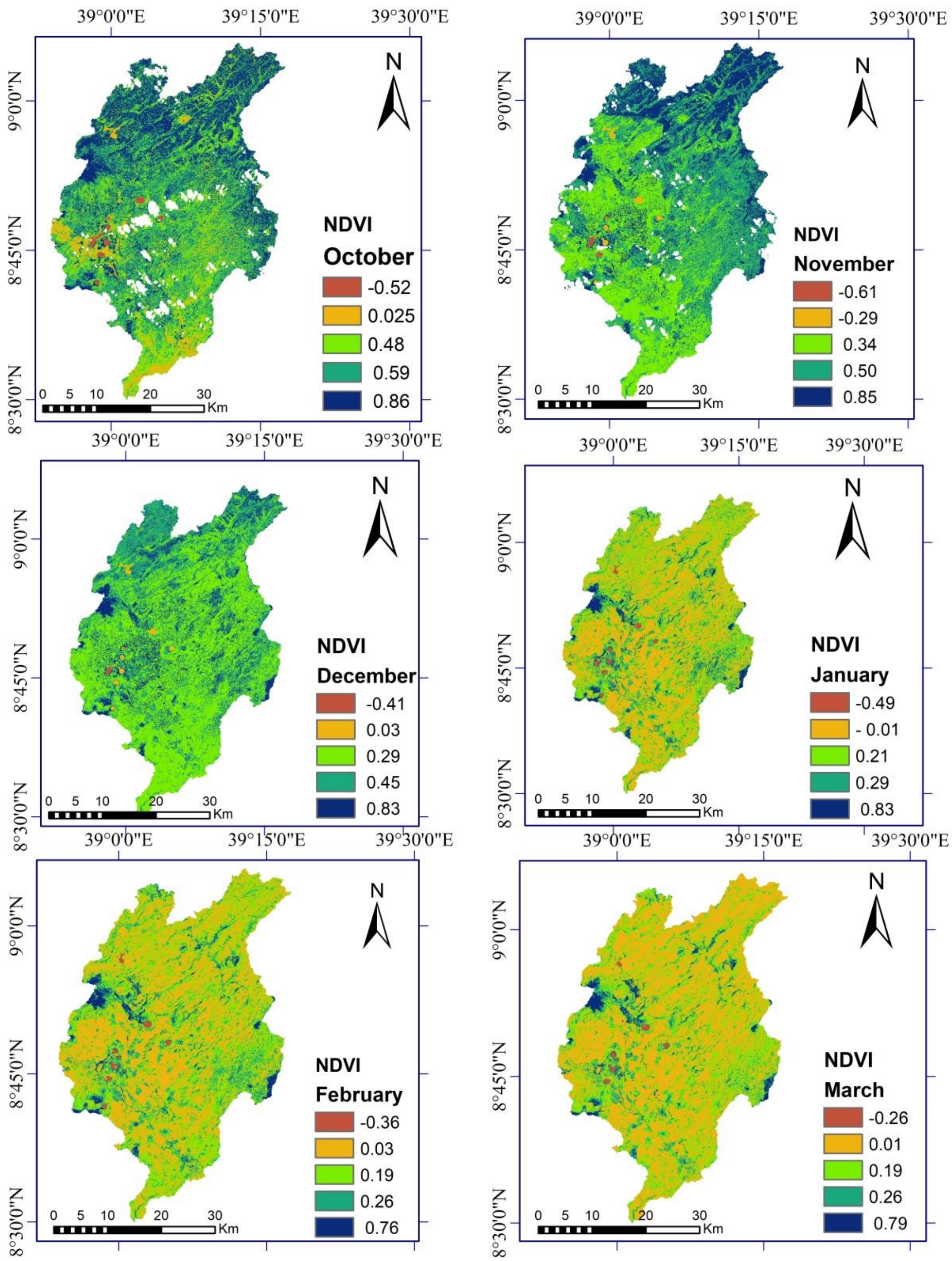

Figure 4. 7 Map of NDVI

4.4.2 Soil Adjusted Vegetation Index (SAVI)

The image shows the Soil Adjusted Vegetation Index (SAVI) values for a catchment from October to March, assessing vegetation health and density. A negative SAVI value indicates vegetation stress severity (figure 4.8). The SAVI (Stress and Vegetation Index) values in October SAVI range from -0.23-0.72 indicate a diverse range of vegetation conditions within the catchment.

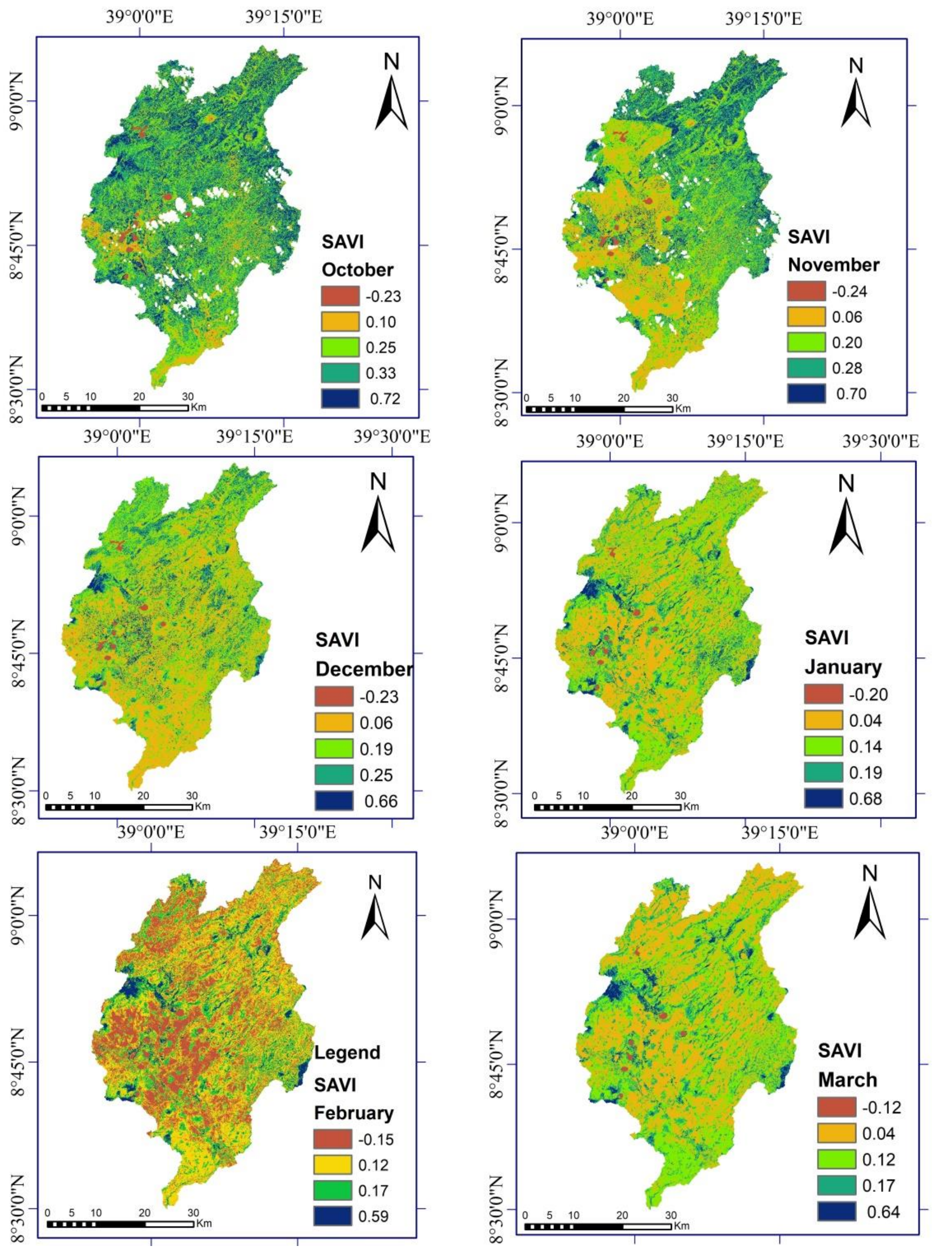

Figure 4. 8 Map of SAVI

Values closer to -1 indicate more stress or lower vegetation density, while higher values correspond to regions with more active vegetation and higher potential evapotranspiration rates. In November, values ranged from -0.24 to 0.7, indicating a range of vegetation health. The SAVI values for vegetation in the catchment have shown a narrower range compared to October, indicating a more consistent vegetation condition. In December, the range was from -0.23 to 0.66, indicating a convergence of vegetation health. In January, the range was from -0.20 to 0.68, with a maximum value of 0.68 indicating improved dense and healthy vegetation. In February, the range was from -0.15 to 0.59, with a narrower range indicating a relatively good vegetation condition. The range remained relatively consistent with the previous month, suggesting a stable vegetation health within the catchment. The value of SAVI with different land use feature have been discribed in (figure 7.7 in Appendices).

4.4.3 Leave Area Index (LAI)

The LAI is a measure of biomass and canopy resistance, indicating the ratio of a plant's total leaf area to its ground area. It's dimensionless and doesn't directly provide information about leaf size. LAI values can vary significantly based on vegetation type, plant species, and environmental conditions. Higher LAI values indicate greater evapotranspiration potential due to more leaves available for transpiration. In October, LAI values ranged from 0.18 to 3.35, suggesting a consistent vegetation density across catchments. The leaf area index (LAI) values for a catchment from October to March showed a narrow range, indicating a convergence of vegetation density. In January, LAI values ranged from 0.08 to 4.33, while in February, they ranged from 0.06 to 1.97. The image provides the LAI values for a given catchment from October to March, assessing vegetation density and canopy cover. The study reveals significant variation in vegetation density within the catchment, with some areas having low leaf area and others having dense canopy cover (Semaw et al., 2019). The LAI values ranged from 0.21 to 6, with a narrower range in November and March, indicating a variety of vegetation types. The value of LAI varies with different land use features, indicating a diverse range of vegetation types across the catchment (figure 7.8 in Appendices).

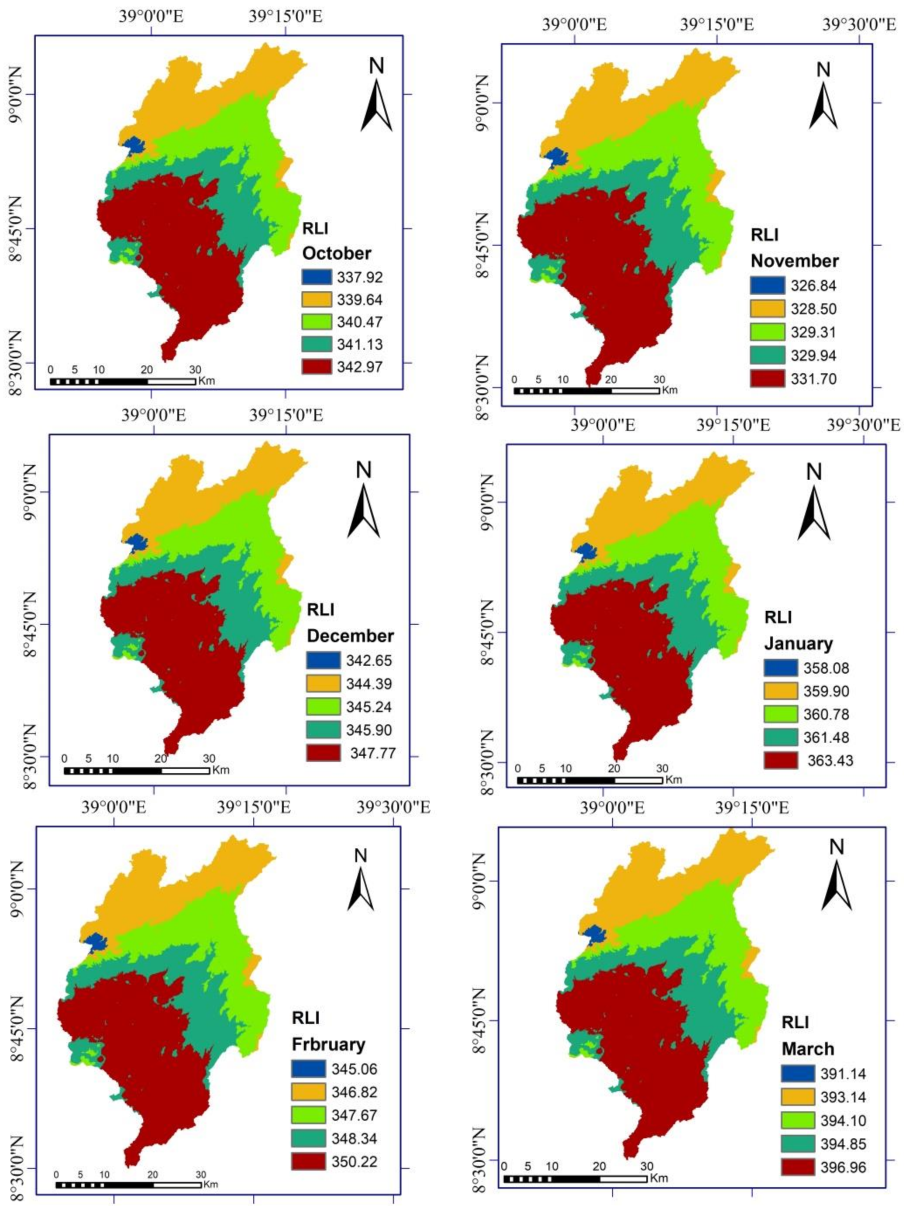

Figure 4. 9 Map of LAI

4.5 Surface temperature (TS)

The image shows surface temperature (TS) values for the Mojo catchment in different months, indicating a range of temperatures within the catchment. In October, the temperature ranged from 23^0C to 39^0C, with higher evapotranspiration rates contributing to lower temperatures. In November, the temperature ranged from 15^0C to 41^0C, with a slightly wider range, indicating greater temperature variation across the catchment. This indicates a range of temperatures within the catchment. The study reveals variations in surface temperature within the Mojo catchment over a six-month period, indicating changes in heat energy emitted by the Earth's surface. In December, with varying ranges in January and February at 25^0C to 41^0C. In March, the temperature ranged from 29^0C to 45^0C, with a wider range indicating greater variation across the catchment. The analysis shows variations in surface temperature over the six-month period, indicating changes in heat energy emitted by the Earth's surface within the Mojo catchment. The values of TS with different land use features are depicted in (figure.7.9 in Appendices).

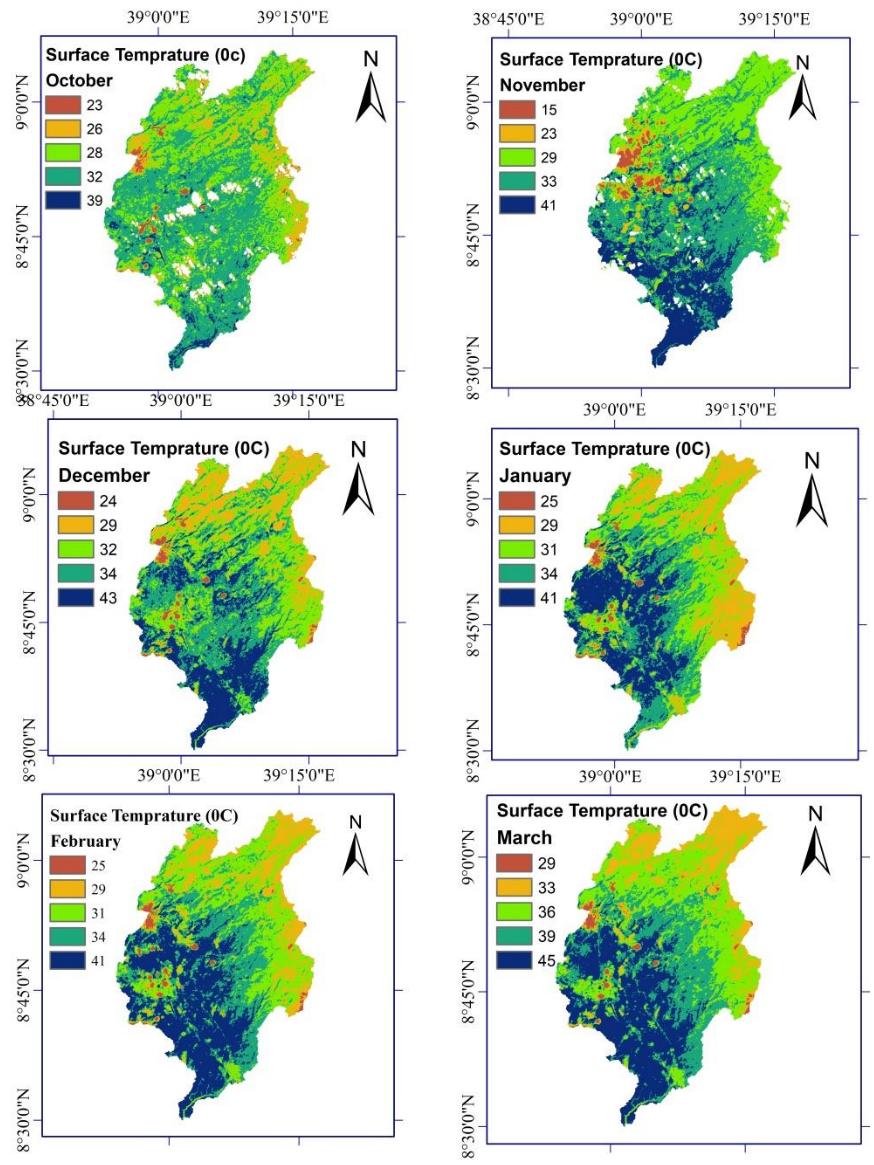

Figure 4. 10 map of surface temperature

4.6 Surface energy balance

4.6.1 Soil heat flux (G)

Soil heat flux is a crucial factor in understanding Earth's surface energy dynamics, indicating the amount of heat energy transferred per unit area and time.

High soil heat flux increases soil surface temperature, while low flux results in cooler temperatures.

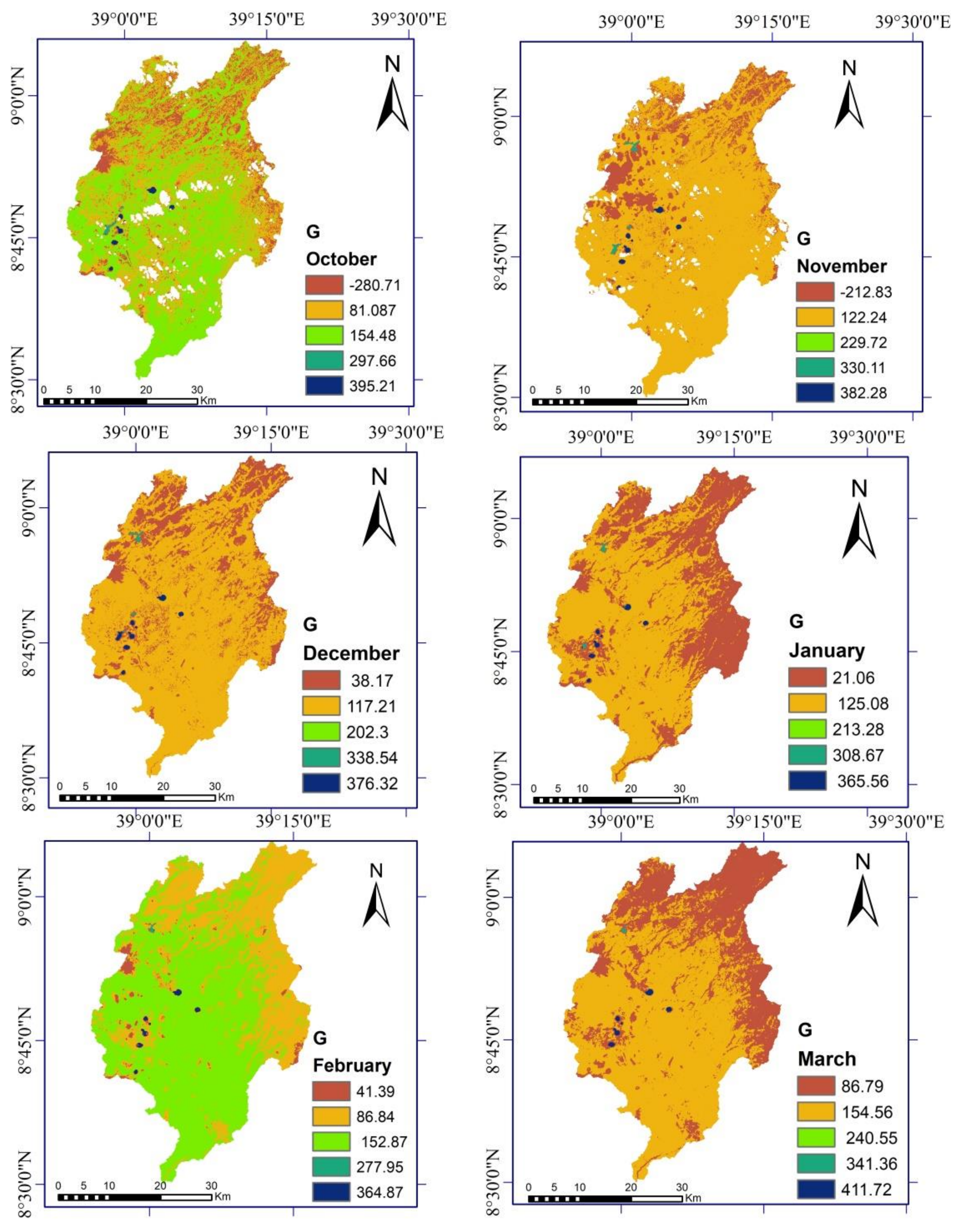

Figure 4. 11 Map of soil heat flux

Soil temperature influences evapotranspiration rates, affecting vapor pressure deficit and water evaporation rate. The Mojo Catchment images show the range of soil heat flux observed over a six-month period. The increasing trend in soil heat flux from October to March suggests a seasonal variation in heat transfer. See figure 4.11 below. The study reveals that analyzing soil heat flux values in Mojo Catchment, along with other environmental data like air temperature, precipitation, and vegetation dynamics, can provide valuable insights into the energy balance and hydrological processes, highlighting seasonal and temporal variations in heat transfer through the soil. Soil heat flux for different land use feature have been discribed in (figure 7.12 in Appendices).

4.6.2 Sensible heat flux (H)

The Mojo Catchment's sensible heat flux values from October to March were recorded, indicating the transfer of heat energy due to temperature differences between land and atmosphere. This is crucial for evapotranspiration. In October, the minimum sensible heat flux was -16.32 w/m^2, while the maximum reached 1659.82 w/m^2. In November, the minimum and maximum values increased to -18.85 and 785.89 w/m^2, respectively. In December, the values increased to 1500.90 w/m^2. The sensible heat flux increased significantly in January, which is minimum sensible flux 20.77 and a maximum of 8455.80 w/m^2. In February, the minimum sensible heat flux was -17.08, while the maximum reached 914.47 w/m^2 , and March, the minimum value was 118.81and maximum 11841.56 w/m^2. The study reveals significant variations in sensible heat flux over a six-month period, with an increasing trend from October to March indicating a seasonal pattern in heat exchange between land and atmosphere. The rising values suggest intensified heat transfer, possibly influenced by factors like solar radiation, air temperature, and land surface characteristics. The exceptionally high maximum values in October and March suggest periods of intense heat exchange, possibly linked to extreme weather events or local environmental factors. The sensible heat flux with different land use feature have been discribed in (figure 7.13 in Appendices).

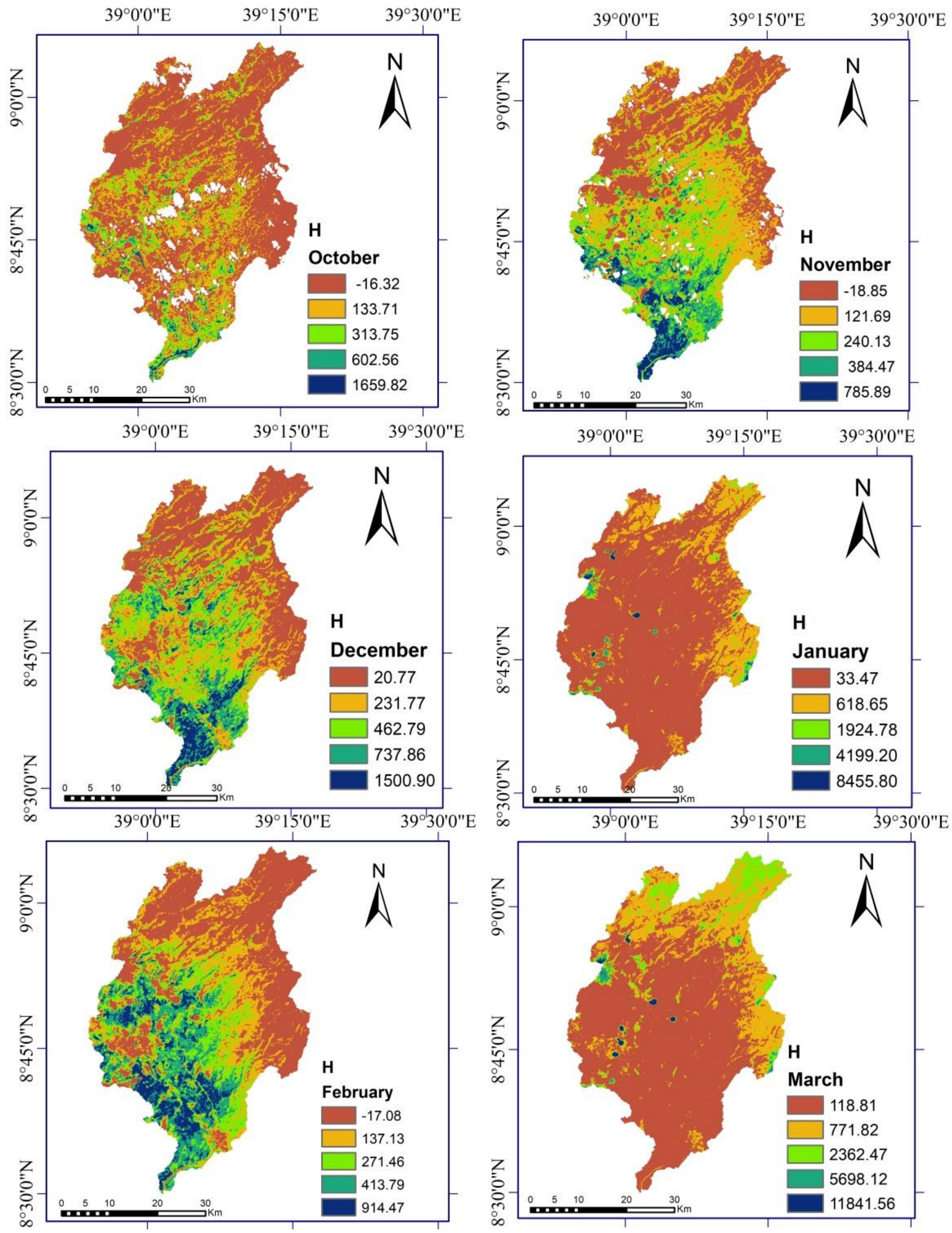

Figure 4. 12 Map of Sensible heat flux

4.6.3 Latent heat flux (LET)

The images show latent heat flux values for the Mojo Catchment from October to March. Latent heat flux is the energy transfer from water vapor evaporation or condensation, a significant part of evapotranspiration. In October, the minimum was -1143.32 w/m^2, indicating a loss of heat energy due to evaporation, while the maximum was 714.12 w/m^2, indicating a net gain. In November, the minimum and maximum values were -396.13 w/m^2 and 730.11 w/m^2, respectively, In December, the values ranged from -1172.12 to 595.11w/m^2. In January,

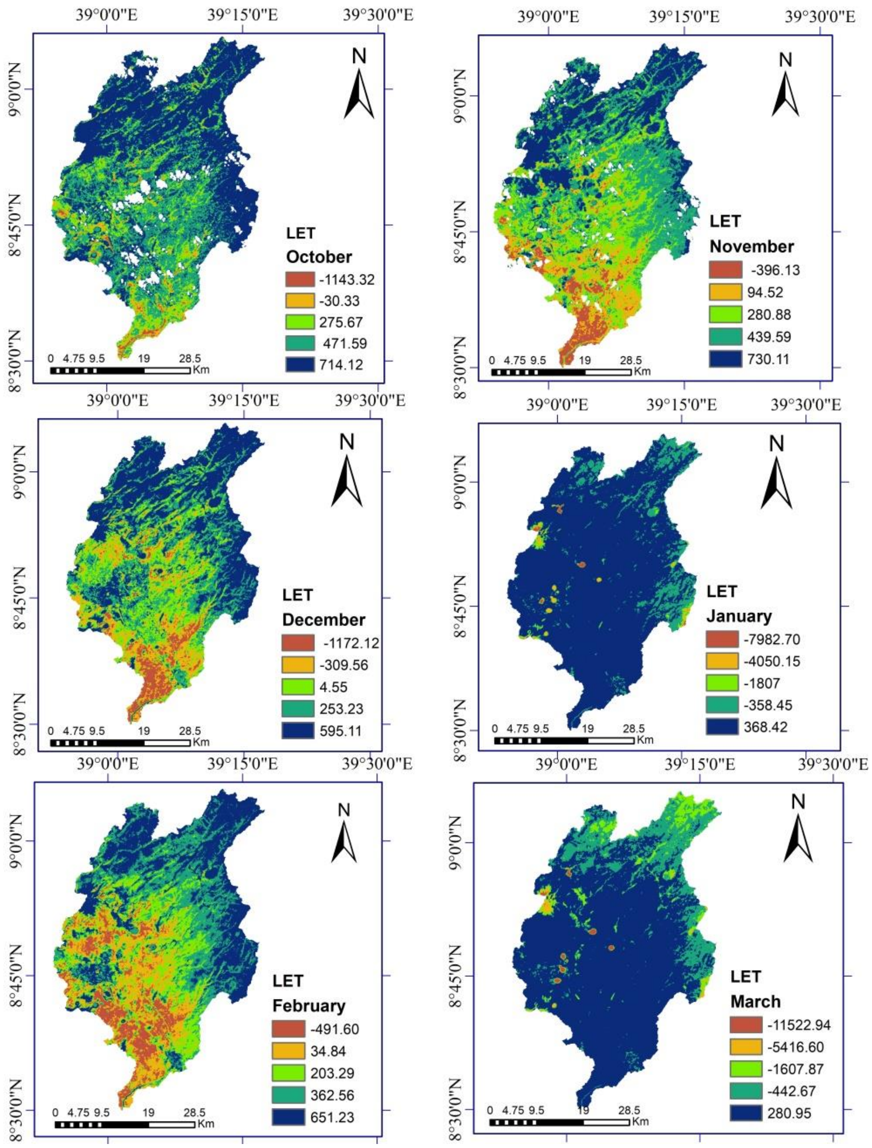

Figure 4. 13 Map of Latent heat flux

the latent heat flux varied significantly, with a minimum of -7982.7 w/m^2 indicating a significant loss of heat energy through evaporation and a maximum of 368.42 w/m^2, indicating a gain through condensation or evaporation. In February, values ranged from -491.6 to 651.23 w/m^2, and in March, they varied between -11522.94 and 280.95 w/m^2, indicating significant variations in heat flux over six months. Latent heat flux fluctuations can be influenced by air temperature, humidity, and water sources for evaporation or condensation. Extreme negative values in January and March indicate high evaporation rates, causing significant heat energy loss. Conversely, positive values indicate periods of condensation or evaporation, releasing or gaining heat energy through water vapor phase changes, balancing water and energy in catchment areas. Latent heat flux values vary with land use features (figure 7.14 in Appendices).

4.7 Instantaneous ET (ETins) and reference ET fraction (ETrF).

Instantaneous ET (ETins)

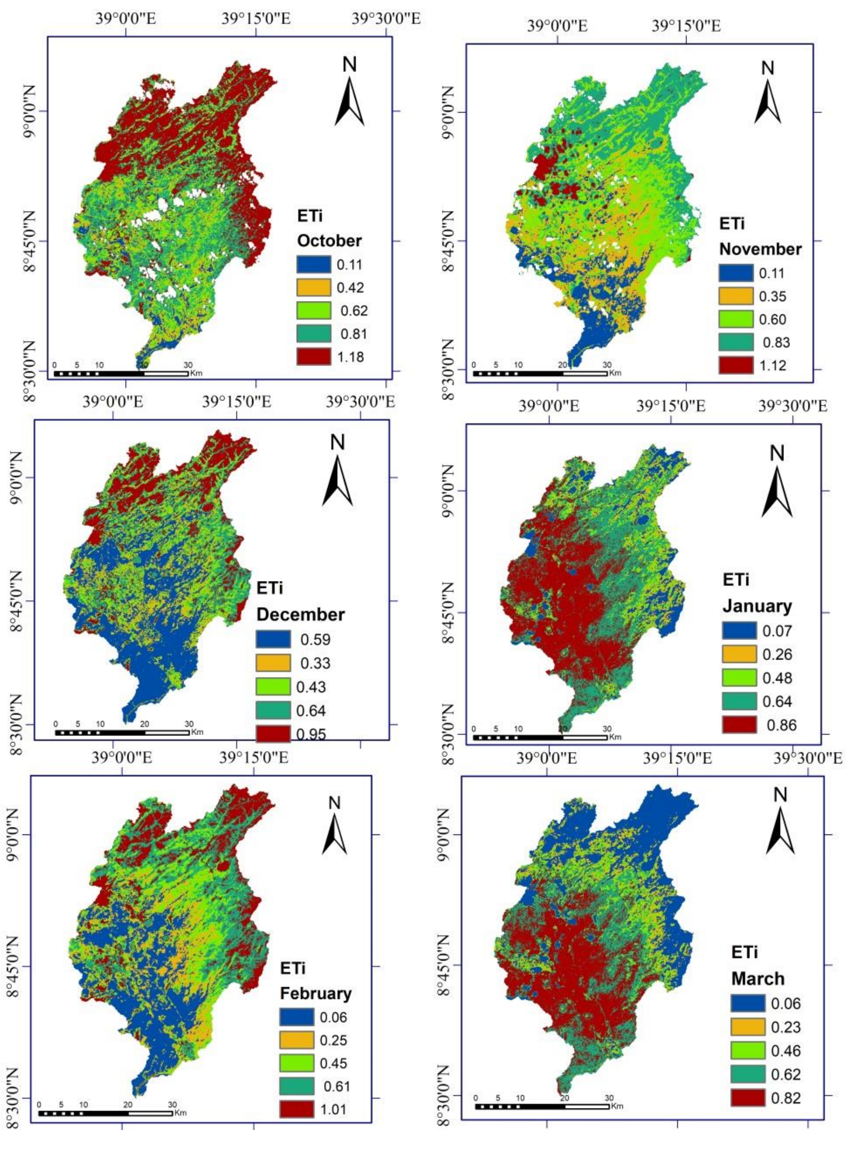

Figure 4. 14 Map of instantanious Evapotranspiration

Instantaneous evapotranspiration (ET) values, refers the evapotranspiration rate at a specific moment in time. Instantaneous ET values provide information about the current rate of water loss from the land surface through evaporation and transpiration. These values can be influenced by various factors such as solar radiation, temperature, humidity, wind speed, and vegetation characteristics.

Reference ET fraction (ETrF)

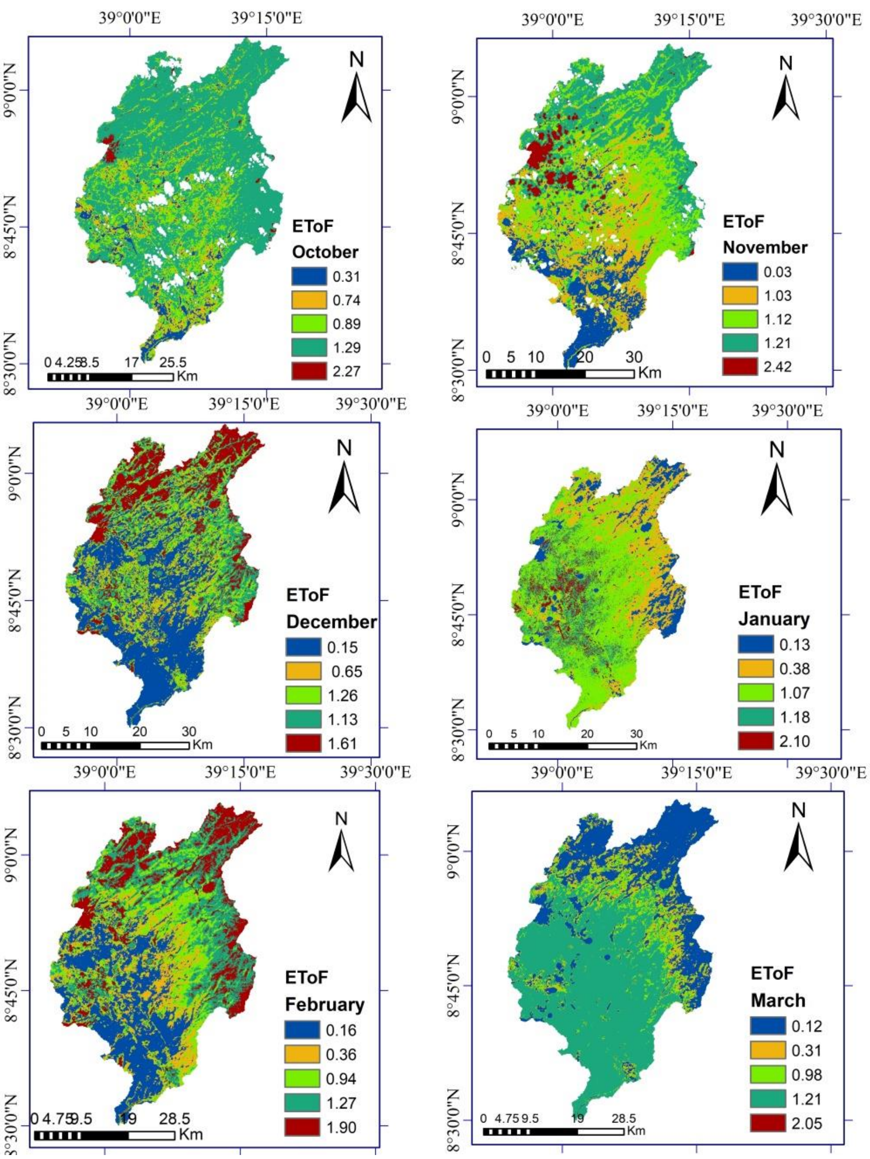

Figure 4. 15 Map of Reference ET Fraction

The Reference ET Fraction (ETrF) is defined as the ratio of the computed instantaneous ET (ETinst) for each pixel to the reference ET (ETr) computed from weather data. Reference crop ET, termed ETr, is the ET rate expected from a well-defined surface of full-cover alfalfa or clipped grass and is computed in the SEBAL process using ground weather data. In some pixel the value of ETrF is greater than one these was due to different reason like cloud cover , the seson that the image data is extracted and it might be the software problem.

4.8 24-Hour Evapotranspiration (ET24)

4.8.1 Daily Evapotranspiration

The temporal variability has been influenced by both vegetation pattern and the climatic conditions throughout the year (Goble & Minch, 2018). In October, the highest mean evapotranspiration value was observed in the Forest land class, with a mean value of 9.15 mm and a standard deviation of 2.13 mm. Agricultural land had the largest area coverage at 65.28%. Moving to November, the mean evapotranspiration values decreased across all land cover classes compared to October. Forest land still had the highest mean value at 8.12 mm, while urban land had the lowest mean value at 4.68 mm. The standard deviation increased for most land cover classes, indicating greater variability in evapotranspiration values. In December, there was a further decrease in mean evapotranspiration values for all land cover classes. Forest land had the highest mean value at.64 mm, while urban land had the lowest mean value at 3.86 mm. The standard deviation remained relatively consistent compared to November. In January and February, the mean evapotranspiration values continued to decrease across all land cover classes 7. Forest land still had the highest mean value in both months. January had the lowest mean evapotranspiration values overall, with Water bodies class having the lowest mean value at 0.79 mm. In March, the mean evapotranspiration values increased slightly compared to the previous two months, but they remained lower than the values in October and November.

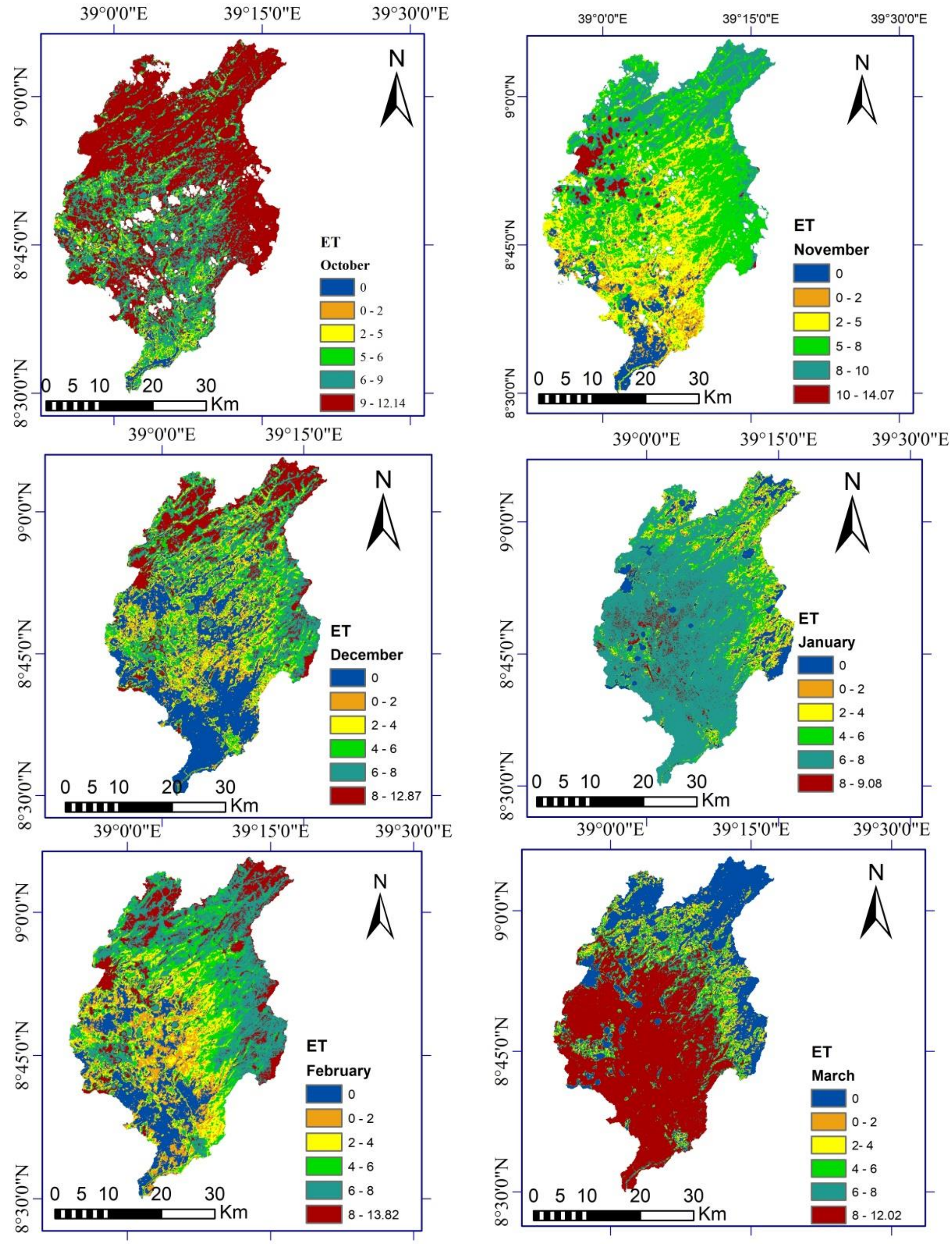

Figure 4. 16 Map of Spatial–temporal distribution of mean daily ETA

Grassland had the highest mean value at 7.83 mm, while Water bodies had the lowest mean value at 1.64 mm. The standard deviation was highest in the Grassland class, indicating greater variability in evapotranspiration values for that land cover class.

The overall analysis shows a general variation in mean evapotranspiration values from October to March, with some variations across different land cover classes. Forest land consistently had the highest mean evapotranspiration values, while Water bodies and Urban land had the lowest values (Semaw et al., 2019). The standard deviation varied across the months and land cover classes, suggesting differences in the variability of evapotranspiration within each category.

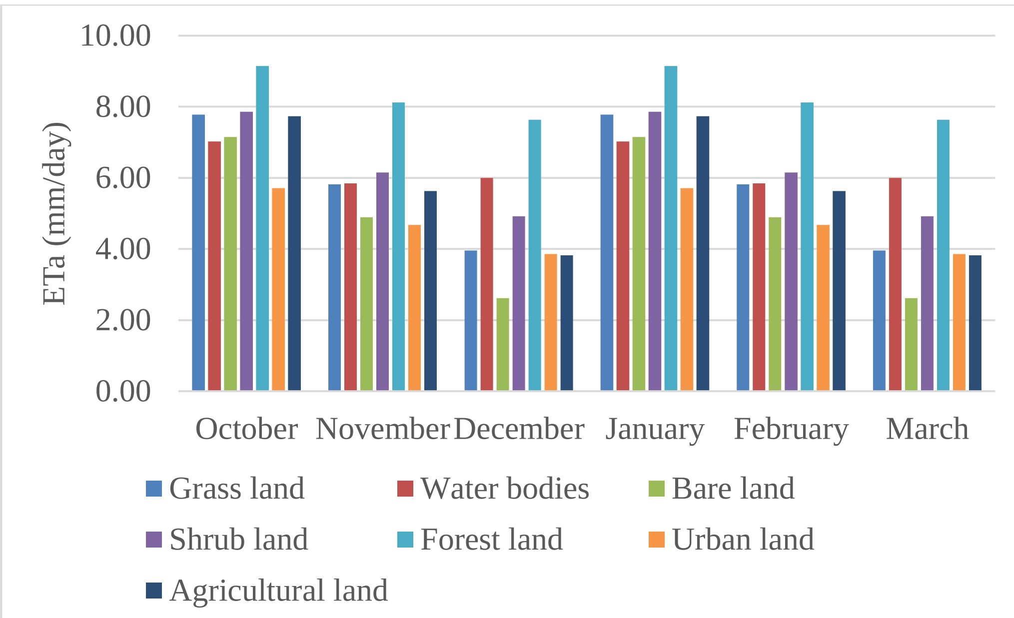

Figure 4. 17 Mean daily ETA in the Mojo catchment for different land use types

4.9 Seasonal evapotranspiration

This can be derived from the 24-hour evapotranspiration data by extrapolating the ET24 proportionally to the reference evapotranspiration (ETr). We assume that the ET for the entire area of interest changes in proportion to the change in the ETr at the weather station. ETr is computed for a specific location and therefore does not represent the actual condition at each pixel.There is over estimation in some pixel in SEBAL model estimation of the ETa for most land use feature.

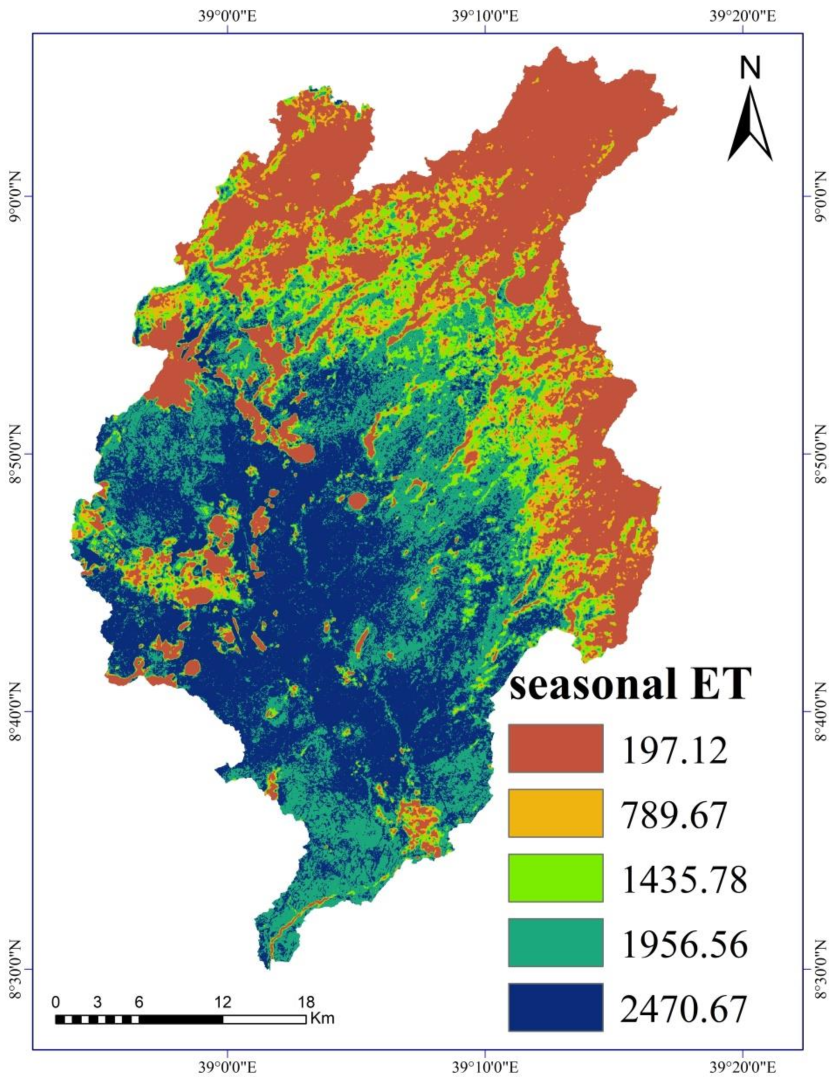

Figure 4. 18 The cumulative map of ET for the selected period (Oct to Mar 2022) of mojo catchment.

4.10 Comparison of ground based evapotranspiration estimation method with SEBAL

The comparison of actual evapotranspiration to reference evapotranspiration is done. The daily actual evapotranspiration results of SEBAL are compared with the FAO Penman reference evapotranspiration for the Mojo catchment with point to pixel value and with the spatial average of daily ETa for the catchment as shown in Table number 4.6.

Table 4. 4 Comparison of Eta in SEBAL model and reference evapotranspiration

Month	ETa in SEBAL	Eta in PM
October	4.99	3.30
November	4.26	2.94
December	4.63	3.12
January	5.01	3.35
February	5.91	3.66
march	6.43	4.23

Eta in sebal is calculated by taking average Kc value 0.9 for different dominant crop type in mojo catchment and by considering the growing season.The SEBAL model is a remote sensing based approach that uses satellite imagery to estimate Eta by considering factors such as land surface temperature, vegetation index, and metrological data The SEBAL model Eta values consistently exceed the observed ETo values from October to march. The actual evapotranspiration, as estimated by the SEBAL model, consistently surpassed the reference evapotranspiration derived from ground observed data during this period.

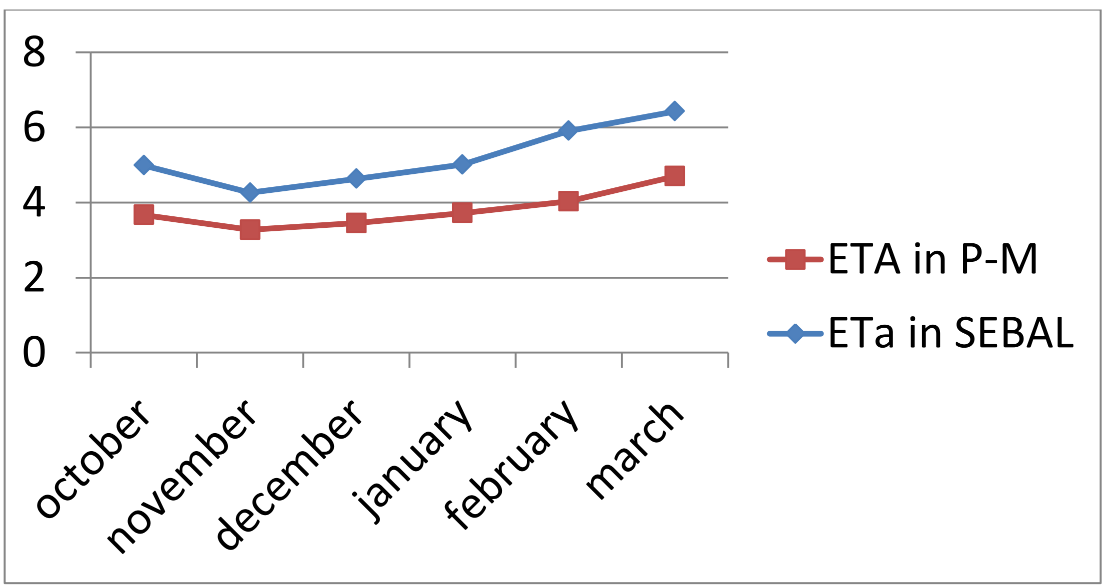

Figure 4. 19 Comparison of Eta in SEBAL and reference evapotranspiration

The higher ET value could be attributing to various factors (SEBAL) model takes in to account specific land surface and vegetation characteristic's that may not be fully captured by the reference evapotranspiration data obtained from ground observation. Additionally the SEBAL model incorporates satellite-derived data .which provide a border spatial coverage and can capture variation In Eta across different areas See Figure 4.19 above.

4.10.1 Comparisons based on Root Mean Square Error

RMSE stands for Root Mean Square Error, which is a commonly used metric to measure the difference between observed and predicted values in various fields, including statistics, machine learning, and data analysis. By using the formula in Equation 3.23 the value of RMSE is equal to 1.14 these indicate The estimation have lower error and acceptable correlation with other comparative methods (Shamloo et al., 2021).

4.11 Model Calibration

The regression value of 0.96 indicates a strong positive correlation between actual evapotranspiration (ETa) estimated by e\the SEBAL model and the reference evapotranspiration (ETa) observed by using penman Monteith formula. these means the SEBAL model is able to accurately capture and predict the evapotranspiration process , as evidenced by the high coefficient of determination R^2 value. Approximately 96.03 of the variability in the ETo can be explained by the variation in the Eta estimated by the SEBAL model , in the other word the SEBAL model demonstrate a high level of accuracy in estimating evapotranspiration, making it a reliable tool for assessing water loss through evapotranspiration processes based on the observed data. The model estimates closely align with the actual evapotranspiration value measured based on ground observed data.This is a significant finding because evapotranspiration plays a crucial role in the water cycle and is an essential component in various environmental and agricultural studies (Wonde et al., 2023).

In summary the regression value of 0.96 reflect a strong correlation between the SEBAL models estimated Eta and the observed ETo. The high R^2 value indicates the model reliability, accuracy, and potential for practical application in various field related to water resource and environmental management.

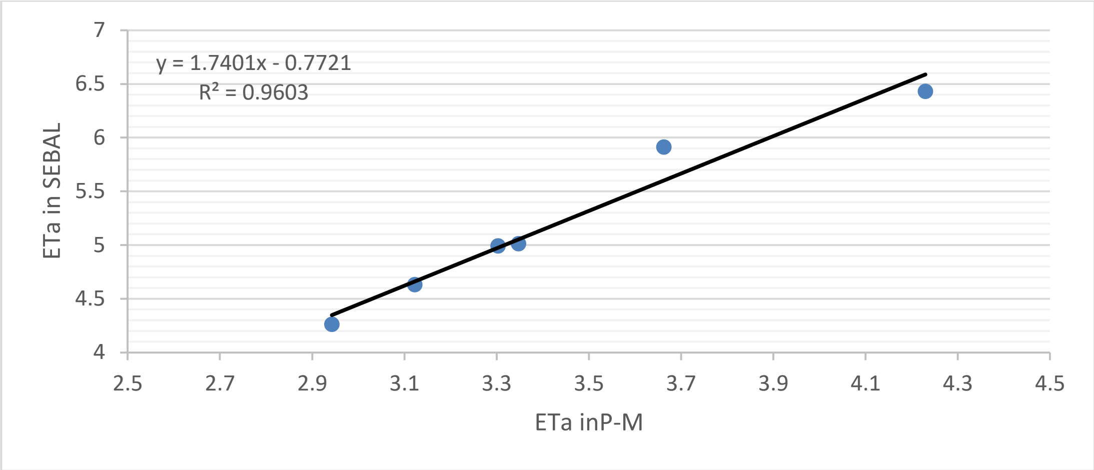

Figure 4. 20 The scatter plot of ETa with P-M and ETa with SEBAL of the catchment at daily basis

Table 4. 5 Adjested value of evapotranspiration for penman by SEBAL output evapotranspiration

Months	Eta in P-M	adjested Eta in P-M
October	3.303	3.31
November	2.943	2.89
December	3.123	3.10
January	3.348	3.32
February	3.663	3.84
March	4.23	4.14

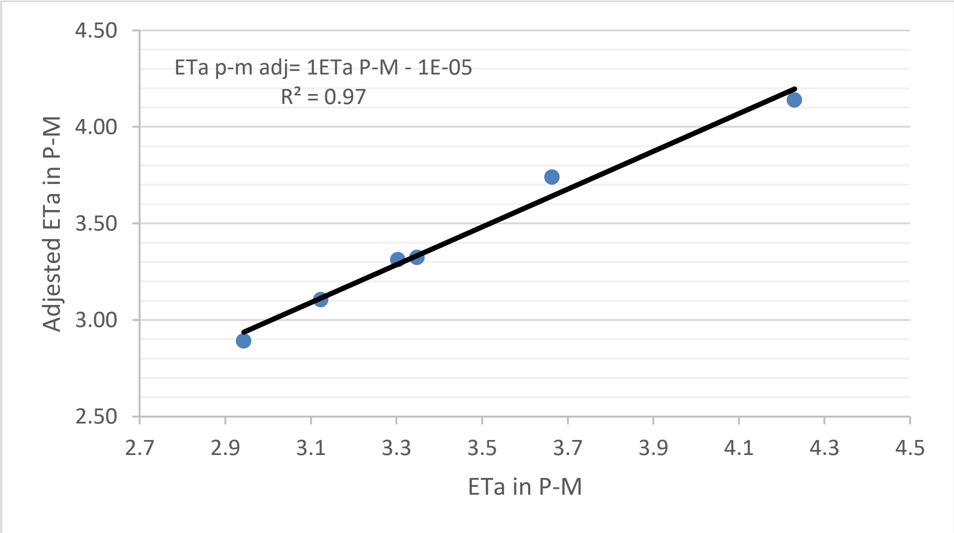

Figure 4. 21 The scatter plot of ETa with P-M and adgested ETa

5. CONCLUSIONS AND RECOMENDATIONS

5.1 Conclusion

This study's primary objective was to estimate satellite evapotranspiration across the Mojo catchment using the SEBAL model and compare it to the Penman-Monteith model. After that, using the surface parameters, the relationship between each energy flux was determined. When the crop coefficients produced by the FAO technique and the SEBAL algorithm were compared, they agreed, showing a very low root-mean-square error value (RMSE=1.14) and a strong correlation coefficient (R^2 = 0.96). Given the high accuracy and low error, the crop coefficient may be appropriately estimated on a regional scale within the appropriate time period using the SEBAL approach. The results obtained from the SEBAL method assisted in understanding the spatial and temporal changes in different stages of plant growth. According to the study, the SEBAL model might be used at local, regional, and global scales in comparable data-poor locations to estimate the actual ET from irrigated agriculture and other land uses. By using this connection in the SEBAL model, the sensible heat flux the most challenging part of the SEBAL calculations was eliminated, and the resulting evapotranspiration was comparable to that obtained using the SEBAL approach.

One method of estimating evapotranspiration in a data-scarce environment where estimation by water balance models is challenging is through SEBAL employing remote sensing data. Real evapotranspiration in the Mojo Catchment might be computed more quickly and easily with a modified version of SEBAL by utilizing the current study's approach and cutting down on the number of calculation stages. Therefore, the relationship may be generalized or adjusted and a modified generic method for calculating the evapotranspiration might be obtained for different locations by adopting the SEBAL model in any other region. The method's drawbacks, however, are as follows: it is only suitable for estimating sensible heat flux (H), which is greatly influenced by errors in surface-air temperature differences or surface temperature measurements; it is not suitable for estimating ET on a daily basis, possibly because ETrF is used to extrapolate instantaneous ET to daily values; it is not suitable for estimating hot/dry and wet/cool pixels within the image; it is not available for cloud-free images. The actual surface ET retrieved based on the SEBAL model correlated highly with the sur1face water ET. This indicating that the SEBAL model that is used to retrieve surface ET in the catchment of mojo.

To estimate evapotranspiration, a variety of remote sensing models have been created thus far; yet, model uncertainties still need to be taken into account. Future research can benefit from the effectiveness of integrating deep learning and hybrid techniques with remote sensing. This would make it possible to create crop coefficient maps of various places and measure evapotranspiration rates with greater accuracy. Better and more effective management of agricultural water and plant health would be made possible by this accurate estimate of plant water requirements.

5.2 Recommendation

In this paper, the SEBAL model and Landsat 8 product are used to classify and estimate spatial temporal evapotranspiration of the Mojo catchment. The spatial and temporal distribution characteristics of surface parameters, radiation, and latent heat flux, sensible heat flux, and soil heat flux and evapotranspiration has been analyzed, for the future the following aspect need to be evaluated :

- The surface energy balance (SEBAL), which was used to predict ETa, has simply been compared to potential evapotranspiration estimations rather than being confirmed using field experiment procedures for the region. Ethiopia lacks ground-based ETA data collection instruments.
- Various temporal and geographical scales Regional and worldwide ETs are required for numerous related fields. Acquiring high temporal and spatial resolution imagery simultaneously is quite difficult, though, because satellites that offer high spatial resolution typically have lower temporal frequencies.

6. REFERENCE

Ajami, H. (2021). Geohydrology: Global Hydrological Cycle. In Encyclopedia of Geology: Volume 1-6, Second Edition (2nd ed., Vol. 6, Issue 3). Elsevier Inc. https://doi.org/10.1016/B978-0-12-409548-9.12387-5

Alemu, M. G., Wubneh, M. A., & Worku, T. A. (2022). Impact of climate change on hydrological response of Mojo river catchment, Awash river basin, Ethiopia. Geocarto International, 0(0). https://doi.org/10.1080/10106049.2022.2152497

Allam, M., Mhawej, M., Meng, Q., Faour, G., Abunnasr, Y., Fadel, A., & Xinli, H. (2021). Monthly 10-m evapotranspiration rates retrieved by SEBALI with Sentinel-2 and MODIS LST data. Agricultural Water Management, 243, 106432.

Allen, R. G. (n.d.). FAO Irrigation and Drainage Paper Crop by. 56.

Allen, R. G., Tasumi, M., & Trezza, R. (2007). Satellite-Based Energy Balance for Mapping Evapotranspiration with Internalized Calibration „ METRIC … — Model. August, 380–394.

Allen, R. G., Tasumi, M., Trezza, R., Waters, R., & Bastiaanssen, W. (2002). SEBAL (surface energy balance algorithms for land). Advance Training and Users Manual–Idaho Implementation, Version, 1, 97.

Aryalekshmi, B. N., Biradar, R. C., Chandrasekar, K., & Ahamed, J. M. (2021). Analysis of various surface energy balance models for evapotranspiration estimation using satellite data. The Egyptian Journal of Remote Sensing and Space Science, 24(3), 1119–1126.

Atanaw, F. (2009). USING REMOTE S E N S I N G PRODUCTS IN THE U P P E R B L U E 36 /) I J · 2tJ D ° J. August.

Bastiaanssen, W. G. M., Menenti, M., Feddes, R. A., & Holtslag, A. A. M. (1998). A remote sensing surface energy balance algorithm for land (SEBAL). 1. Formulation. Journal of Hydrology, 212, 198–212.

Bastiaanssen, W. G. M., Noordman, E. J. M., Pelgrum, H., Davids, G., Thoreson, B. P., &

Allen, R. G. (2005). SEBAL Model with Remotely Sensed Data to Improve Water-Resources Management under Actual Field Conditions. Journal of Irrigation and Drainage Engineering, 131(1), 85–93. https://doi.org/10.1061/(asce)0733-9437(2005)131:1(85)

Biru, Z., & Kumar, D. (2017). Calibration and validation of SWAT model using stream flow and sediment load for Mojo watershed , Ethiopia. https://doi.org/10.1007/s40899-017-0189-1

Bushira, K. M. (2019). Unsupervised Classification and Recode in Erdas Imagine. https://agualabs.edublogs.org/2019/01/24/unsupervised-classification-and-recode-in-erdas-imagine/

Chirouze, J., Boulet, G., Jarlan, L., Fieuzal, R., Rodriguez, J. C., Ezzahar, J., Bigeard, G., & Merlin, O. (2014). Intercomparison of four remote-sensing-based energy balance methods to retrieve surface evapotranspiration and water stress of irrigated fields in semi-arid climate. 1165–1188. https://doi.org/10.5194/hess-18-1165-2014

Copyright, N. T., & Allen, R. G. (2000). REF-ET : REFERENCE EVAPOTRANSPIRATION CALCULATION SOFTWARE for FAO and ASCE Standardized Equations.

Droogers, P., & Allen, R. G. (2002). Estimating reference evapotranspiration under inaccurate data conditions. Irrigation and Drainage Systems, 16, 33–45.

Du, J., Song, K., Wang, Z., Zhang, B., & Liu, D. (2013). Evapotranspiration estimation based on MODIS products and surface energy balance algorithms for land (SEBAL) model in Sanjiang Plain, Northeast China. Chinese Geographical Science, 23, 73–91.

Fonji and Taff, MohanRajan, S. N., Loganathan, A., & Manoharan, P. (2020). Survey on Land Use/Land Cover (LU/LC) change analysis in remote sensing and GIS environment: Techniques and Challenges. Environmental Science and Pollution Research, 27(24), 29900–29926. https://doi.org/10.1007/s11356-020-09091-7

Fonji, S. F., & Taff, G. N. (2014). Using satellite data to monitor land-use land-cover change in North-eastern Latvia. SpringerPlus, 3(1), 1–15. https://doi.org/10.1186/2193-1801-3-

61

French, A. N., Hunsaker, D. J., & Thorp, K. R. (2015). Remote Sensing of Environment Remote sensing of evapotranspiration over cotton using the TSEB and METRIC energy balance models ☆. Remote Sensing of Environment, 158, 281–294. https://doi.org/10.1016/j.rse.2014.11.003

G, A. M., A, W. M., & A, W. T. (2022). ce pt us cr t. Geocarto International, 0(0), 000. https://doi.org/10.1080/10106049.2022.2152497

Ghosh, P. (2018). ASSESSING CROP MONITORING POTENTIAL OF SENTINEL-2 IN A SPATIO-TEMPORAL SCALE. XLII(November), 20–23.

Ghosh, T., Chakraborty, D., Das, B., Sehgal, V. K., Mukherjee, J., Roy, D., Rathore, P., & Dhakar, R. (2023). Evaluation of satellite remote sensing-based crop evapotranspiration models over a semi-arid irrigated agricultural farm.

Goble, L. L., & Minch, A. (2018). Evaluation of Spatio-Temporal Pattern of Actual Evapotranspiration Using Sebal Model Over Kilti Watershed , Ethiopia Evaluation of Spatio-Temporal Pattern of Actual Evapotranspiration Using Sebal Model Over Kilti.

Griffith, J. A. (2002). Geographic techniques and recent applications of remote sensing to landscape-water quality studies. Water, Air, and Soil Pollution, 138, 181–197.

Haque, M. N., Siddika, S., Sresto, M. A., Saroar, M. M., & Shabab, K. R. (2021). Geo-spatial analysis for flash flood susceptibility mapping in the North-East Haor (Wetland) Region in Bangladesh. Earth Systems and Environment, 5(2), 365–384.

Hashem, A. A., Engel, B. A., Bralts, V. F., Marek, G. W., Moorhead, J. E., Rashad, M., Radwan, S., & Gowda, P. H. (2020). Landsat Hourly Evapotranspiration Flux Assessment Using Lysimeters for the Texas High Plains. 1–14.

Irmak, A., Irmak, S., & Martin, D. L. (2007). Satellite remote sensing based estimation of land surface evapotranspiration in great plains. World Environmental and Water Resources Congress 2007: Restoring Our Natural Habitat, 1–10.

Joshi, S., Arindom, R., Dikshit, T., Anish, B., Deep, A. G., & Pallav, P. (2015). Conceptual paper on factors affecting the attitude of senior citizens towards purchase of smartphones. Indian Journal of Science and Technology, 8(12), 83–89. https://doi.org/10.17485/ijst/2015/v8i

Journal of Geophysical Research : Atmospheres. (2017). https://doi.org/10.1002/2016JD026065

Kiros, G., Shetty, A., & Nandagiri, L. (2015). Performance Evaluation of SWAT Model for Land Use and Land Cover Changes under different Climatic Conditions: A Review. Journal of Waste Water Treatment & Analysis, 06(03). https://doi.org/10.4172/2157-7587.1000216

Kumar, Batar, A., Watanabe, T., & Kumar, A. (2017). Assessment of land-use/land-cover change and forest fragmentation in the Garhwal Himalayan Region of India. Environments, 4(2), 34.

Kumar, R., Jat, M. K., & Shankar, V. (2012). Methods to estimate irrigated reference crop evapotranspiration–a review. Water Science and Technology, 66(3), 525–535.

Kustas, W. P., & Norman, J. M. (1996). Utilisation de la télédétection pour le suivi de l'évapotranspiration sur les terres. Hydrological Sciences Journal, 41(4), 495–516. https://doi.org/10.1080/02626669609491522

Kwast, H. Van Der, & Jong, S. De. (2004). MODELLING EVAPOTRANSPIRATION USING THE SURFACE ENERGY BALANCE SYSTEM (SEBS) AND LANDSAT TM DATA (RABAT REGION ,. 1–11.

Laipelt, L., Ruhoff, A. L., Fleischmann, A. S., Bloedow Kayser, R. H., Kich, E. de M., Rocha, H. R. da, & Usher Neale, C. M. (2020). Assessment of an automated calibration of the SEBAL Algorithm to estimate dry-season surface-energy partitioning in a Forest-Savanna Transition in Brazil. Remote Sensing, 12(7). https://doi.org/10.3390/rs12071108

Liou, Y., & Kar, S. K. (2014). Evapotranspiration Estimation with Remote Sensing and Various Surface Energy Balance Algorithms—A Review. 2821–2849.

https://doi.org/10.3390/en7052821

Liu, C., Lu, N., McNulty, S. G., & Miao, H. (2011). A general predictive model for estimating monthly ecosystem evapotranspiration. Ecohydrology, 4(2), 245–255.

López, P. L., Sutanudjaja, E. H., Schellekens, J., Sterk, G., & Bierkens, M. F. P. (2017). Calibration of a large-scale hydrological model using satellite-based soil moisture and evapotranspiration products. Hydrology and Earth System Sciences, 21(6), 3125–3144. https://doi.org/10.5194/hess-21-3125-2017

Makkeasorn, A., Chang, N., Beaman, M., Wyatt, C., & Slater, C. (2006). Soil moisture estimation in a semiarid watershed using RADARSAT-1 satellite imagery and genetic programming. Water Resources Research, 42(9).

Melesse, A. M., Abtew, W., & Dessalegne, T. (2009). Evaporation estimation of Rift Valley Lakes: comparison of models. Sensors, 9(12), 9603–9615.

Moratiel, R., Bravo, R., Saa, A., Tarquis, A. M., & Almorox, J. (2019). Estimation of evapotranspiration by FAO Penman-Monteith Temperature and Hargreaves-Samani models under temporal and spatial criteria. A case study in Duero Basin (Spain). Nat. Hazards Earth Syst. Sci, 20(3), 859–875.

Munoth, P., & Goyal, R. (2020). Impacts of land use land cover change on runoff and sediment yield of Upper Tapi River Sub-Basin, India. International Journal of River Basin Management, 18(2), 177–189.

Nazila, Taghi Sattari, M., Apaydin, H., Valizadeh Kamran, K., & Prasad, R. (2021). Evapotranspiration estimation using SEBAL algorithm integrated with remote sensing and experimental methods. International Journal of Digital Earth, 14(11), 1638–1658.

Nouri, H., Faramarzi, M., Sobhani, B., & Sadeghi, S. H. (2017). Estimation of evapotranspiration based on surface energy balance algorithm for land (SEBAL) using Landsat 8 and modis images. Applied Ecology and Environmental Research, 15(4), 1971–1982. https://doi.org/10.15666/aeer/1504_19711982

October 2021. (2021). October.

Odusanya, A. E., Mehdi, B., Schürz, C., Oke, A. O., Awokola, O. S., Awomeso, J. A., Adejuwon, J. O., & Schulz, K. (2019). Multi-site calibration and validation of SWAT with satellite-based evapotranspiration in a data-sparse catchment in southwestern Nigeria. Hydrology and Earth System Sciences, 23(2), 1113–1144. https://doi.org/10.5194/hess-23-1113-2019

Parveen, M. T., & Ilahi, R. A. (2022). Assessment of land-use change and its impact on the environment using GIS techniques: a case of Kolkata Municipal Corporation, West Bengal, India. GeoJournal, 87(s4), 551–566. https://doi.org/10.1007/s10708-022-10581-z

Pereira, L. S., Allen, R. G., Smith, M., & Raes, D. (2015). Crop evapotranspiration estimation with FAO56: Past and future. Agricultural Water Management, 147, 4–20.

Pramanik. (1993). Satellite remote sensing of river inundation area, stage, and discharge: A review. Hydrological Processes, 11(10), 1427–1439. https://doi.org/10.1002/(sici)1099-1085(199708)11:10<1427::aid-hyp473>3.0.co;2-s

Ravazzani, G., Corbari, C., Morella, S., Gianoli, P., & Mancini, M. (2012). Modified Hargreaves-Samani Equation for the Assessment of Reference Evapotranspiration in Alpine River Basins. Journal of Irrigation and Drainage Engineering, 138(7), 592–599. https://doi.org/10.1061/(asce)ir.1943-4774.0000453

Running, S. W., Mu, Q., Zhao, M., & Moreno, A. (2019). MODIS Global Terrestrial Evapotranspiration (ET) Product (MOD16A2/A3 and Year-end Gap-filled MOD16A2GF/A3GF) NASA Earth Observing System MODIS Land Algorithm. NASA EOSDIS Land Processes DAAC, 1–37. https://doi.org/10.5067/MODIS/MOD16A3GF.006

Semaw, T. K., Tekleab, S., & Napoli, M. (2019). Surface Energy Balance Algorithm for Land (SEBAL) based Evapotranspiration Estimation in Lower Gilgel Abay Catchment Lake Tana Sub-Basin , Ethiopia. 7(1), 11–27.

Shamloo, N., Sattari, M. T., Apaydin, H., Valizadeh, K., & Prasad, R. (2021).

Evapotranspiration estimation using SEBAL algorithm integrated with remote sensing and experimental methods Evapotranspiration estimation using SEBAL algorithm integrated with remote sensing and experimental methods. https://doi.org/10.1080/17538947.2021.1962996

Shamloo, N., Taghi Sattari, M., Apaydin, H., Valizadeh Kamran, K., & Prasad, R. (2021). Evapotranspiration estimation using SEBAL algorithm integrated with remote sensing and experimental methods. International Journal of Digital Earth, 14(11), 1638–1658. https://doi.org/10.1080/17538947.2021.1962996

Shu, Y., Stisen, S., Jensen, K. H., & Sandholt, I. (2011). Estimation of regional evapotranspiration over the North China Plain using geostationary satellite data. International Journal of Applied Earth Observation and Geoinformation, 13(2), 192–206. https://doi.org/10.1016/j.jag.2010.11.002

Sun, H., & Yong, Y. (2019). Improving Estimation of Cropland Evapotranspiration by the Bayesian Model Averaging Method with Surface Energy Balance Models. March 2022. https://doi.org/10.3390/atmos10040188

Tena, T. M., Mwaanga, P., & Nguvulu, A. (2019). Impact of land use/land cover change on hydrological components in Chongwe River Catchment. Sustainability (Switzerland), 11(22). https://doi.org/10.3390/su11226415

Teshome, D. S., Leta, M. K., Taddese, H., Moshe, A., Tolessa, T., Ayele, G. T., & You, S. (2015). Watershed Hydrological Responses to Land Cover Changes at Muger Watershed, Upper Blue Nile River Basin, Ethiopia. Water, 15(14), 2533.

Teuling, A. J., Seneviratne, S. I., Williams, C., & Troch, P. A. (2006). Observed timescales of evapotranspiration response to soil moisture. 33(October), 1–5. https://doi.org/10.1029/2006GL028178

Tomar, A. S. (2022). Evaluating the Performance of Calibrated Temperature-based Equations as Compared to Standard FAO-56 Penman Monteith Equation in Humid Climatic Condition of Dehradun (India). Journal of Agricultural Engineering, 59(4), 386–403.

Trajkovic, S. (2005). Temperature-Based Approaches for Estimating Reference Evapotranspiration. Journal of Irrigation and Drainage Engineering, 131(4), 316–323. https://doi.org/10.1061/(asce)0733-9437(2005)131:4(316)

Trezza, R., Allen, R. G., & Tasumi, M. (2013). Estimation of Actual Evapotranspiration along the Middle Rio Grande of New Mexico Using MODIS and Landsat Imagery with the METRIC Model. 5397–5423. https://doi.org/10.3390/rs5105397

VerstrETaen, W. W., Veroustaete, F., & Feyen, J. (2008). Assessment of evapotranspiration and soil moisture content across different scales of observation. Sensors, 8(1), 70–117. https://doi.org/10.3390/s8010070

Waters, R., Allen, R., Tasumi, M., Trezza, R., & Bastiaanssen, W. (2002). Surface Energy Balance Algorithms for Land (SEBAL). Advanced Training and Users Manual, 1–97.

Wonde, D., Tewodros, M., Abdu, T. A., & Sisay, Y. Y. (2023). A remote sensing approach to estimate variable crop coefficient and evapotranspiration for improved water productivity in the Ethiopian highlands. Applied Water Science, 13(8), 1–15. https://doi.org/10.1007/s13201-023-01968-5

Xp, W., & Allen, R. G. (2016). REF-ET : REFERENCE EVAPOTRANSPIRATION CALCULATION SOFTWARE for FAO and ASCE Standardized Equations.

Yang, L., Li, J., Sun, Z., Liu, J., Yang, Y., & Li, T. (2022). Daily actual evapotranspiration estimation of different land use types based on SEBAL model in the agro-pastoral ecotone of northwest China. PLoS ONE, 17(3 March), 1–18. https://doi.org/10.1371/journal.pone.0265138

Zhuang, Q., Shi, Y., Shao, H., Zhao, G., & Chen, D. (2021). Evaluating the SSEBop and RSPMPT models for irrigated fields daily evapotranspiration mapping with MODIS and CMADS data. Agriculture, 11(5), 424.

Zotarelli, L., Dukes, M. D., Romero, C. C., Migliaccio, K. W., & Morgan, K. T. (2010). Step by step calculation of the Penman-Monteith Evapotranspiration (FAO-56 Method). Institute of Food and Agricultural Sciences. University of Florida, 8.

7. APPENDICES

Table7. 1 Sample Meteorological data forone day in 24 January from 2022

Year	Month	Date	Time	RF (mm)	Global Radiation (RS) (W/m²)	Relative Humidity (% RH)	Temperature (°C)	Wind Direction (°)	Wind Speed (m/s)
2022	Jan	24	0	0	0.6	57.325	15.85	33.1	0.55
2022	Jan	24	1	0	0.6	58.525	15.525	52.4	0.825
2022	Jan	24	2	0	0.6	58.125	15.575	38.5	1.125
2022	Jan	24	3	0	0.6	59.15	15.025	34.625	0.55
2022	Jan	24	4	0	0.6	59.7	14.8	159.25	0.8
2022	Jan	24	5	0	0.55	61.2	14.575	122.45	1.025
2022	Jan	24	6	0	2.875	67.825	14.425	112.48	1.35
2022	Jan	24	7	0	58.525	65.6	16.5	59.875	1.75
2022	Jan	24	8	0	172.075	60.125	18.775	81.85	2.475
2022	Jan	24	9	0	298.375	57.1	20.7	127.9	2.225
2022	Jan	24	10	0	400.875	51.425	22.05	48.875	2.975
2022	Jan	24	11	0	468.525	45.75	23.3	63.45	2.975
2022	Jan	24	12	0	489.15	41.6	24.275	62.75	3
2022	Jan	24	13	0	482.325	38.425	25.4	136.48	2.75
2022	Jan	24	14	0	433.725	32.925	25.925	32.025	2.525
2022	Jan	24	15	0	346.675	31.725	26.275	55.625	3.275
2022	Jan	24	16	0	224.95	31.7	25.9	63.925	3.475
2022	Jan	24	17	0	72.675	35.325	24.5	46.2	3.525
2022	Jan	24	18	0	4.7	40.875	22.525	61.425	2.675
2022	Jan	24	19	0	0.575	47.925	21.05	25.25	2.4
2022	Jan	24	20	0	0.55	49.2	20.325	40.525	2.3
2022	Jan	24	21	0	0.6	52.25	19.55	40.75	1.8
2022	Jan	24	22	0	0.6	53.925	19.2	29.5	2.2
2022	Jan	24	23	0	0.6	53.925	19.2	29.5	2.2

Image 7. 1 Interface of REF-ET software

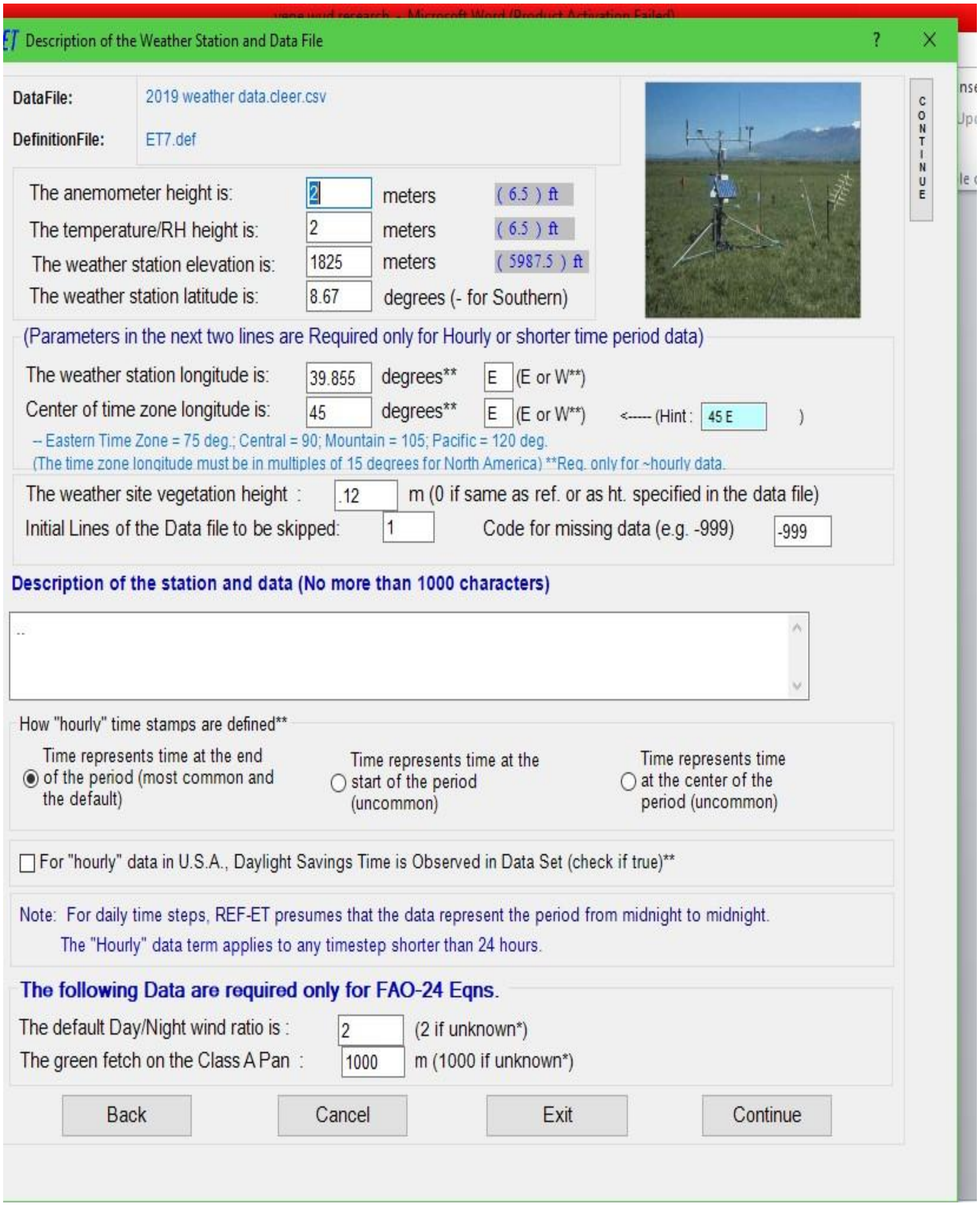

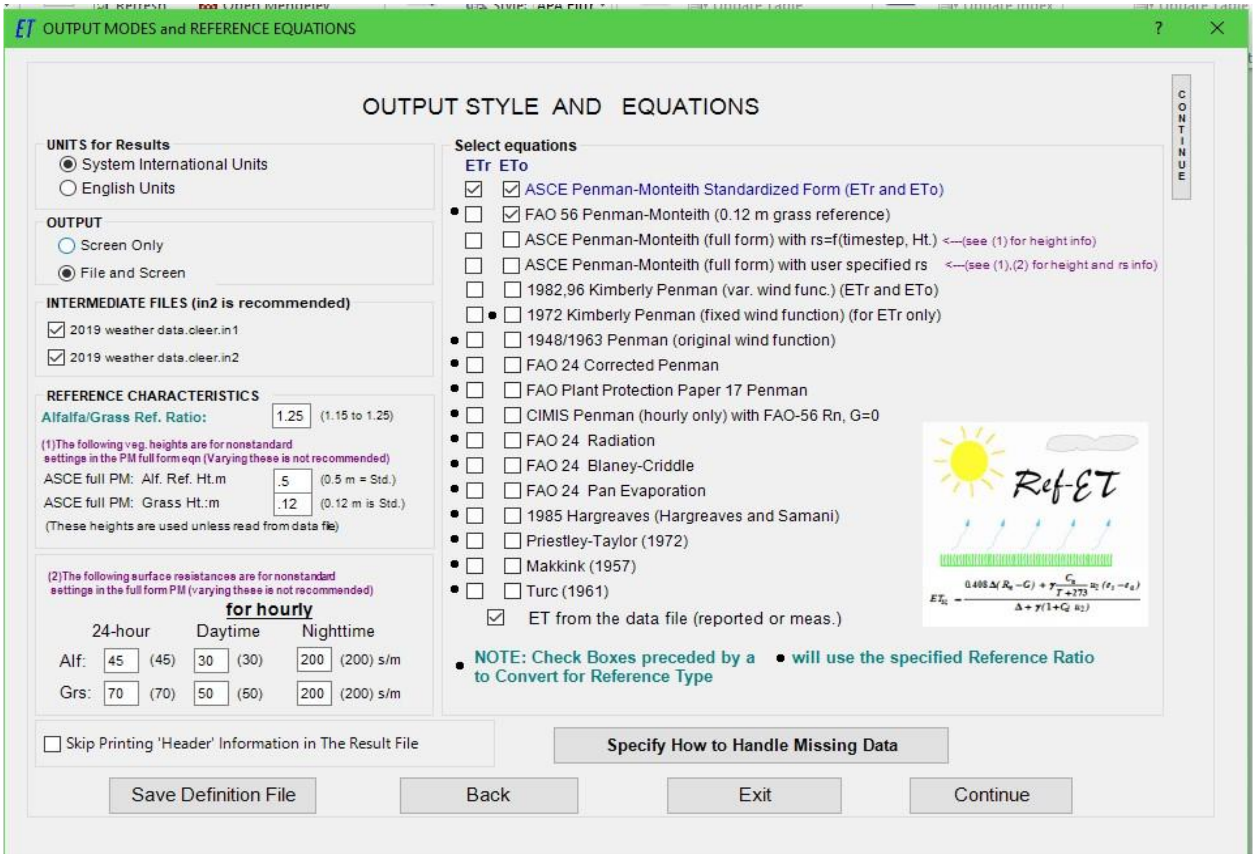

Image 7. 2Sample Output of ref- et software

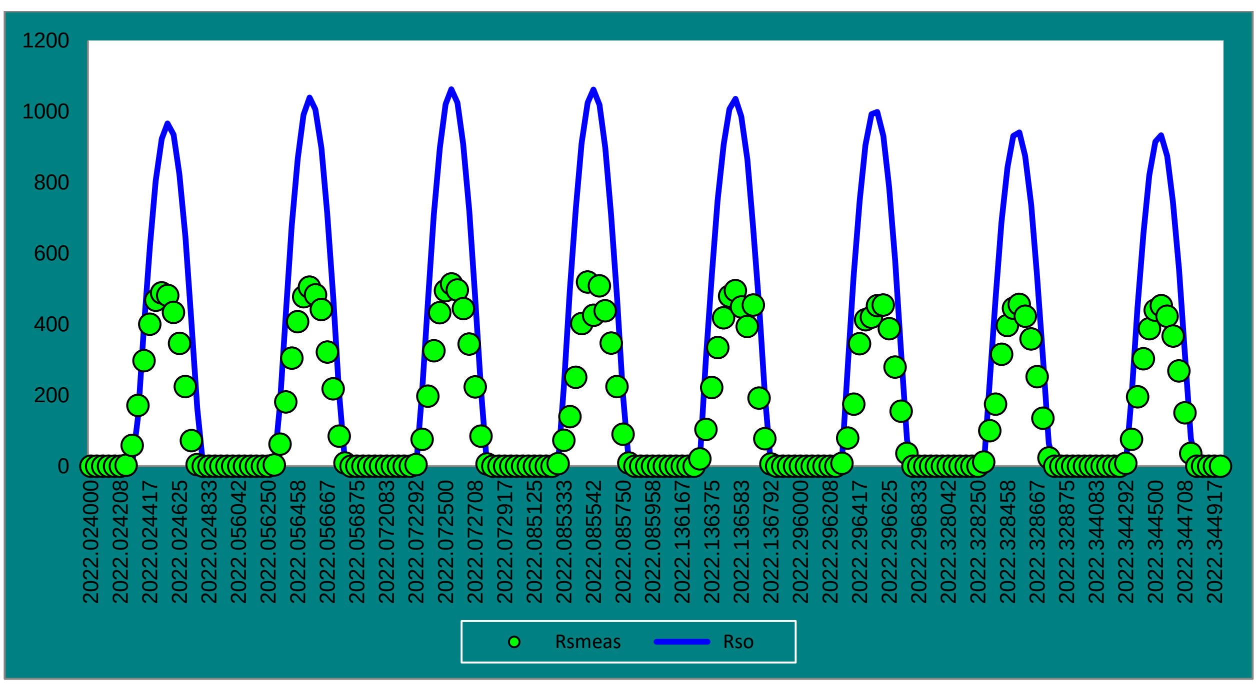

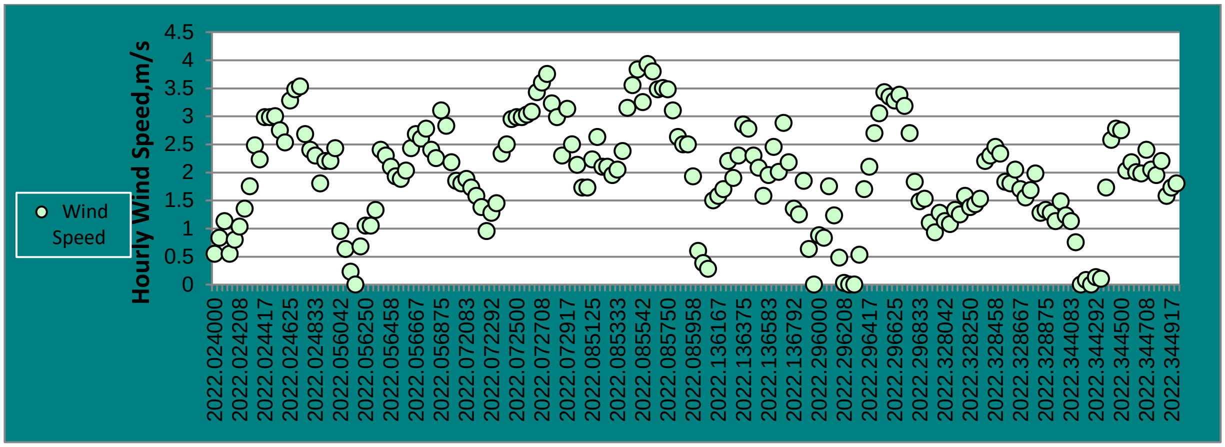
Wind Speed
Hourly Wind Speed,m/s

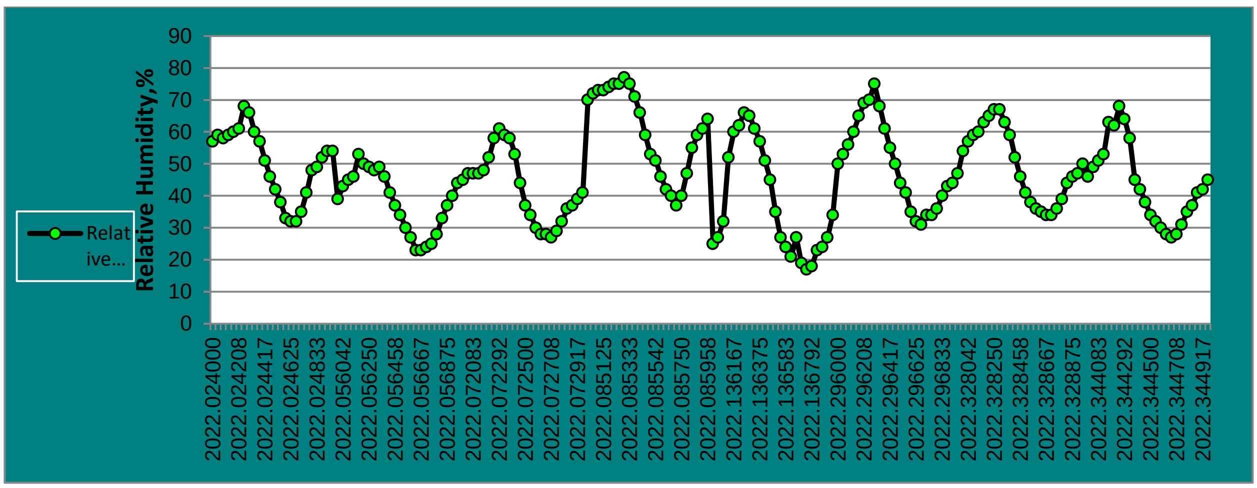
Relative...
Relative Humidity,%

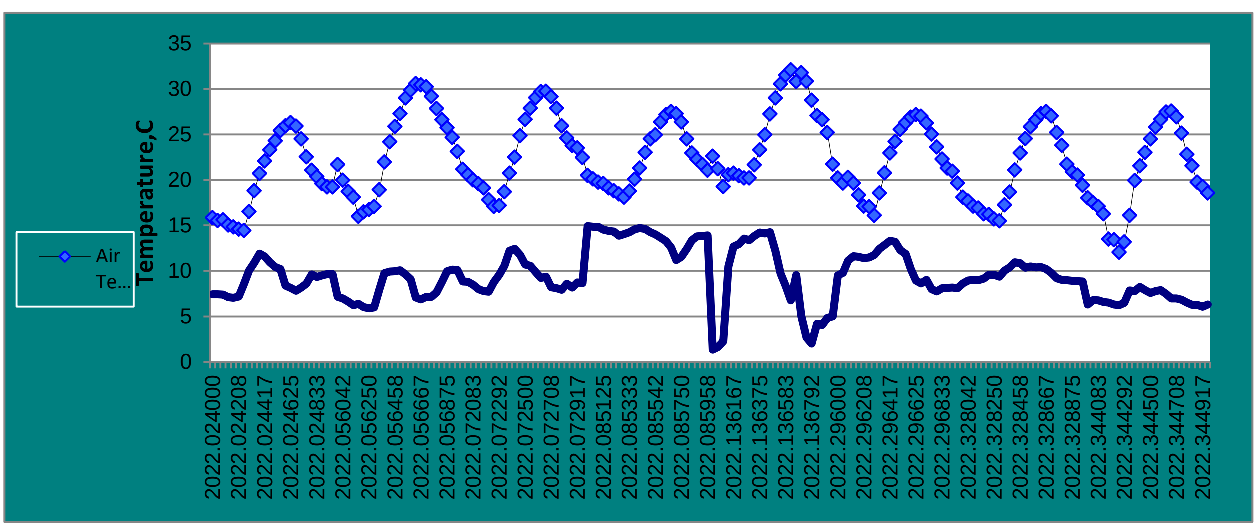
Air Te...
Temperature,C

Table7. 2 Calclation of satellite overpass time, instantanious evapotranspiration, and windspped

$$t1 = int[\frac{\left(10 + \frac{40}{60} + \frac{34}{3600}\right)}{1} + \frac{1}{2} - 0.5](1) + 0$$

t1= int[10.67](1)+0 = 10 hours

t1 - t2 – t1 =1

t2 = t1+1 = 11hours

Therefore, the two weather data periods used to determine the wind speed and ETr at the image time are 1000 and 1100 hours, Mountain Standard Time recommendation

ETo refers to grass reference ET (e.g., “short” reference) and ETr refers to alfalfa reference ET (e.g., “tall” reference). The calculation is done with REF-ET software and the procuder obtain in figure 7.1 and 7.2 from appendicses.

Mon	Day	Year	DoY	HrMn	Tmax	Tmin (	Rs (W/n	Wind (	DewP	stPM Etr (mm/	stPM Eto (mm/				
1	24	2022	24	0	15.85	15.85	.00	0.55	7.44	0	0	6			
1	24	2022	24	100	15.53	15.53	.00	0.83	7.44	0.01	0	7			
1	24	2022	24	200	15.58	15.58	.00	1.13	7.38	0.02	0.01	8			
1	24	2022	24	300	15.03	15.03	.00	0.55	7.12	-0.01	-0.01	9			
1	24	2022	24	400	14.8	14.8	.00	0.8	7.05	0	0	10			
1	24	2022	24	500	14.58	14.58	.00	1.03	7.2	0.01	0.01	11			
1	24	2022	24	600	14.43	14.43	.00	1.35	8.56	0.01	0.01	12			
1	24	2022	24	700	16.5	16.5	.00	1.75	10.04	0.07	0.04	1			
1	24	2022	24	800	18.78	18.78	141.00	2.48	10.88	0.19	0.14	2			
1	24	2022	24	900	20.7	20.7	610.39	2.23	11.91	0.28	0.22	3		Etr	U
1	24	2022	24	1000	22.05	22.05	821.37	2.98	11.57	0.42	0.33	4	Data t1=@1000 hr	0.330	2.980
1	24	2022	24	1100	23.3	23.3	958.60	2.98	10.95	0.51	0.4	5	Data t2=@1100 hr	0.400	2.980
1	24	2022	24	1200	24.28	24.28	1001.62	3	10.41	0.56	0.44	6	Δt=	1	
1	24	2022	24	1300	25.4	25.4	987.28	2.75	10.22	0.56	0.44	7	t image(local time)=	10:40:34AM	10.676
1	24	2022	24	1400	25.93	25.93	888.96	2.53	8.39	0.54	0.42	8	FlagDST=	0	
1	24	2022	24	1500	26.28	26.28	710.76	3.28	8.15	0.54	0.4	9	Flag period=	0.5	
1	24	2022	24	1600	25.9	25.9	460.87	3.48	7.81	0.47	0.32	10			
1	24	2022	24	1700	24.5	24.5	149.53	3.53	8.18	0.34	0.21	11			
1	24	2022	24	1800	22.53	22.53	10.24	2.68	8.58	0.11	0.08	12			
1	24	2022	24	1900	21.05	21.05	2.05	2.4	9.6	0.09	0.06	1			
1	24	2022	24	2000	20.33	20.33	.00	2.3	9.33	0.08	0.06	2			
1	24	2022	24	2100	19.55	19.55	.00	1.8	9.51	0.07	0.05	3			
1	24	2022	24	2200	19.2	19.2	.00	2.2	9.65	0.07	0.05	4			
1	24	2022	24	2300	19.2	19.2	.00	2.2	9.65	0.07	0.05	5			
										Average Eto per day	3.73				

$$t_1 = \text{int}\left[\frac{t_{\text{image (local time)}}}{\Delta t} + \frac{1}{2} - \text{Flag}_{\text{period}}\right]\Delta t + \text{Flag}_{\text{DST}}$$

$$t_2 = t_1 + \Delta t$$

where;

t_1 = time identifier for the first weather period in hours

t_2 = time identifier for the second weather period in hours

Δt = length of weather period in units consistent with t_1 and t_2 (i.e., hours)

$t_{\text{image (local time)}}$ = the satellite image time (local time, with no adjustment for daylight savings)

$\text{Flag}_{\text{period}}$ = a flag for the way that the weather data period is represented by its "time label". $\text{Flag}_{\text{period}}$ = 0 if the time label is the endpoint of the weather data period; = 1 if the time label is the beginning of the weather data period; = 0.5 if the time label represents the midpoint of the weather data period.

Flag_{DST} = a flag for use of DST in the weather data set. Flag_{DST} = 0 if no DST is used and Flag_{DST} = 1 hour if DST is used in the weather data set.

(3) Estimate the instantaneous wind speed applying a simple linear interpolation assumption.

Δt=	1	
t image(local time)=	10:40:34	10.68
FlagDST=	0	
Flag period=	0.5	

Data t1=@1000 hr	0.330	10 t1
Data t2=@1100 hr	0.400	11 t2

$$\text{Data}_{\text{image}} = \text{Data}_{t_1} + \frac{\left(\text{Data}_{t_2} - \text{Data}_{t_1}\right)}{\Delta t}\left[t_{\text{image (Local time)}} - \left(t_1 - \text{Flag}_{\text{DST}} + \Delta t\,\text{Flag}_{\text{period}} - \frac{\Delta t}{2}\right)\right]$$

where;

Data_{t1} = the average value for the specific data parameter (i.e., wind or ET_r) for the t_1 time period

Data_{t2} = the average value for the specific data parameter (i.e., wind or ET_r) for the t_2 time period

Datat1	((Datat2-Datat1)/Δt)	local time	t1	FlagDST	ΔtFlagperiod	Δt/2
0.330	0.07	10.68	10	0	0.5	0.5
			10			
		0.68				
		0.047328				

Etr@10:40:34 local time	0.38	mm/hr

$$t_1 = \text{int}\left[\frac{t_{image(local\,time)}}{\Delta t} + \frac{1}{2} - Flag_{period}\right]\Delta t + Flag_{DST}$$

$$t_2 = t_1 + \Delta t$$

where;

t_1 = time identifier for the first weather period in hours

t_2 = time identifier for the second weather period in hours

Δt = length of weather period in units consistent with t_1 and t_2 (i.e., hours)

$t_{image\ (local\ time)}$ = the satellite image time (local time, with no adjustment for daylight savings)

$Flag_{period}$ = a flag for the way that the weather data period is represented by its "time label". $Flag_{period}$ = 0 if the time label is the endpoint of the weather data period; = 1 if the time label is the beginning of the weather data period; = 0.5 if the time label represents the midpoint of the weather data period.

$Flag_{DST}$ = a flag for use of DST in the weather data set. $Flag_{DST}$ = 0 if no DST is used and $Flag_{DST}$ = 1 hour if DST is used in the weather data set.

Δt=	1	
t image(local time)=	10:40:34	10.68
FlagDST=	0	
Flag period=	0.5	
Data t1=@1000 hr	2.980	10 t1
Data t2=@1100 hr	2.980	11 t2

$$Data_{image} = Data_{t_1} + \frac{\left(Data_{t_2} - Data_{t_1}\right)}{\Delta t}\left[t_{image(Local\,time)} - \left(t_1 - Flag_{DST} + \Delta t\, Flag_{period} - \frac{\Delta t}{2}\right)\right]$$

where;

$Data_{t1}$ = the average value for the specific data parameter (i.e., wind or ET_r) for the t_1 time period

$Data_{t2}$ = the average value for the specific data parameter (i.e., wind or ET_r) for the t_2 time period

(3) Estimate the instantaneous wind speed applying a simple linear interpolation assumption.

Datat1	((Datat2-Datat1)/Δt)	local time	t1	FlagDST	ΔtFlagperiod	Δt/2
2.980	0	10.68	10	0	0.5	0.5
			10			
		0.68				
		0				

Wind speed @10:40:34 local time	2.98	m/s

Image 7. 3Albedo value for deferent land use feature in a given six month (October-march)

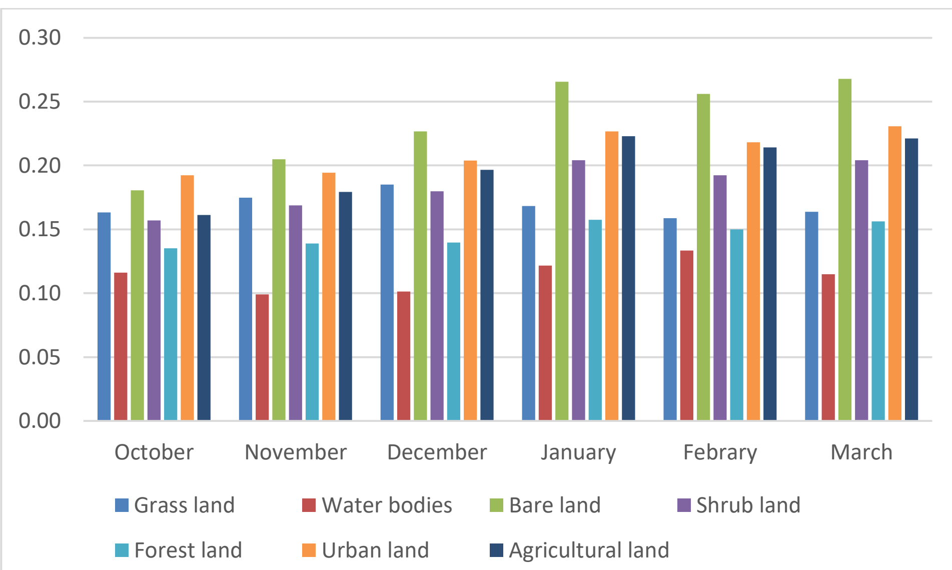

Image 7. 4 Incoming short wave radiation value for deferent land use feature in a given six month (October-march)

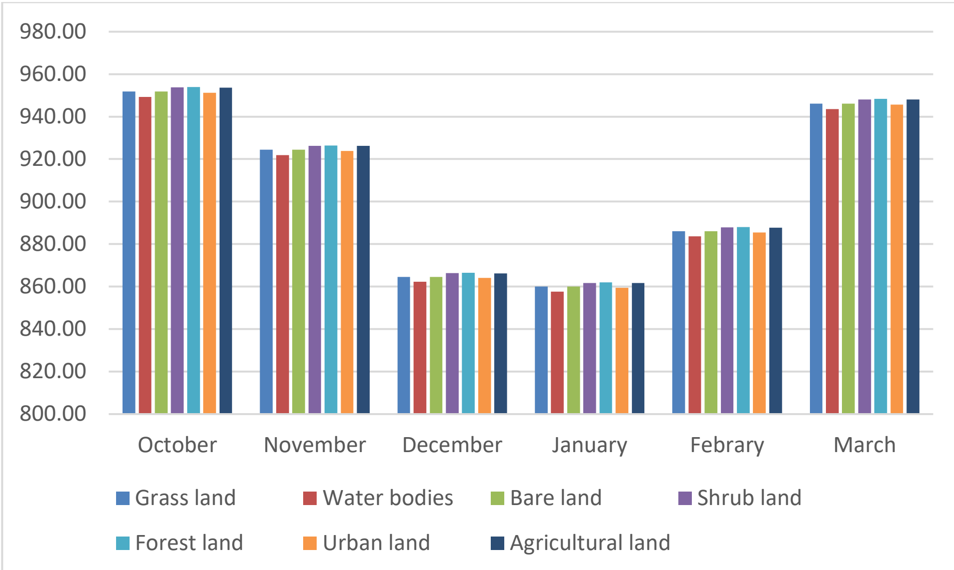

Image 7. 5 Outgoing long wave radiation value for deferent land use feature in a given six month (October-march)

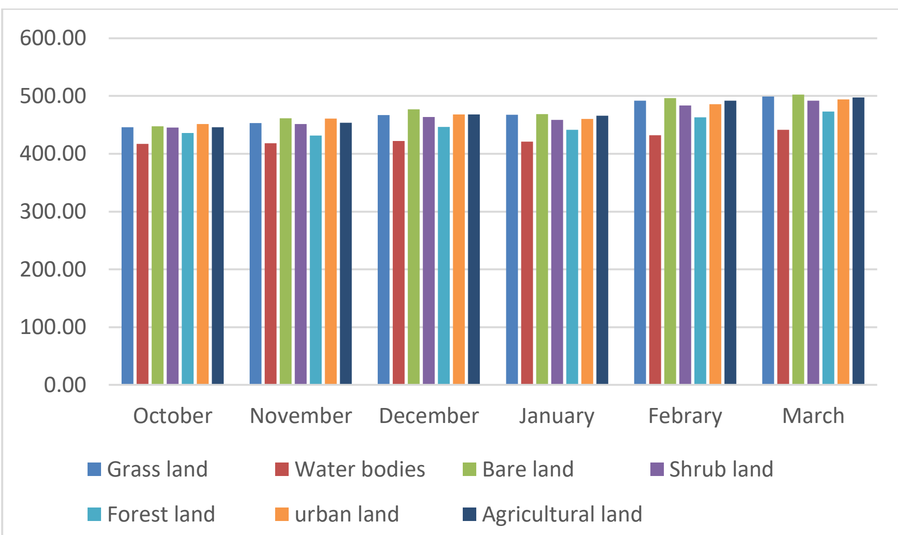

Image 7. 6 Normalize difference vegetable index value for deferent land use feature in a given six month (October-march)

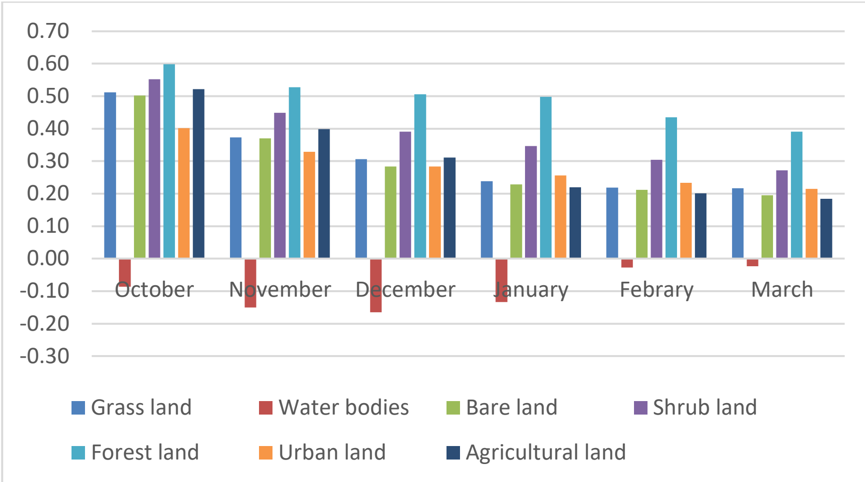

Image 7. 7SAVI Value for deferent land use feature in a given six month (October-march)

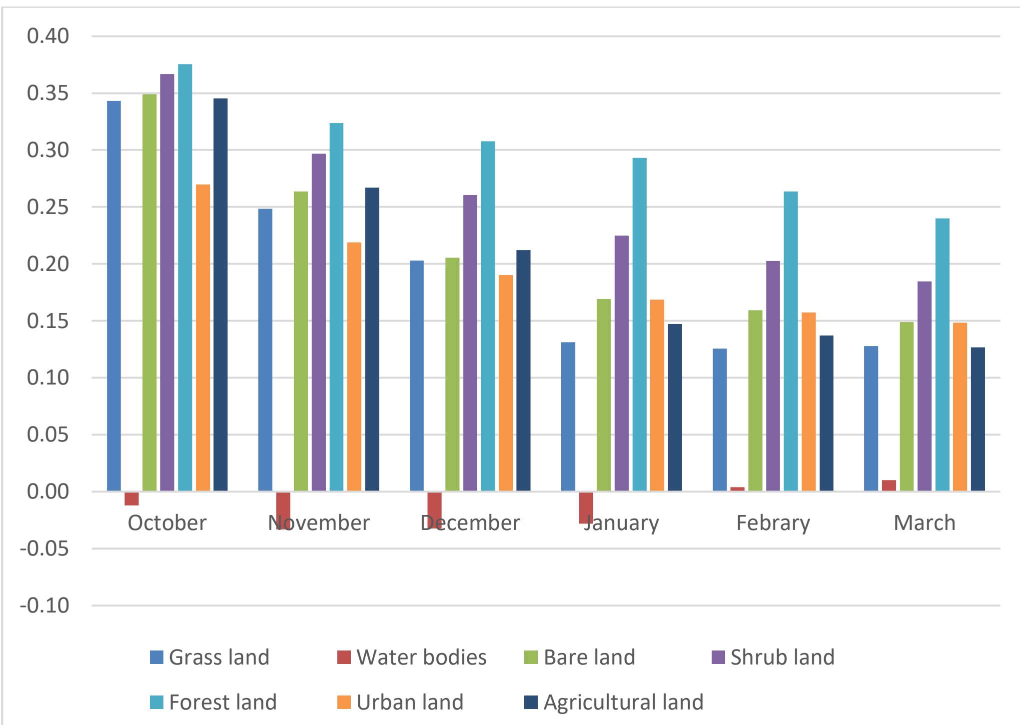

Image 7. 8 LAI value for different land use feature for mojo catchment for the period of 2022 (October- March)

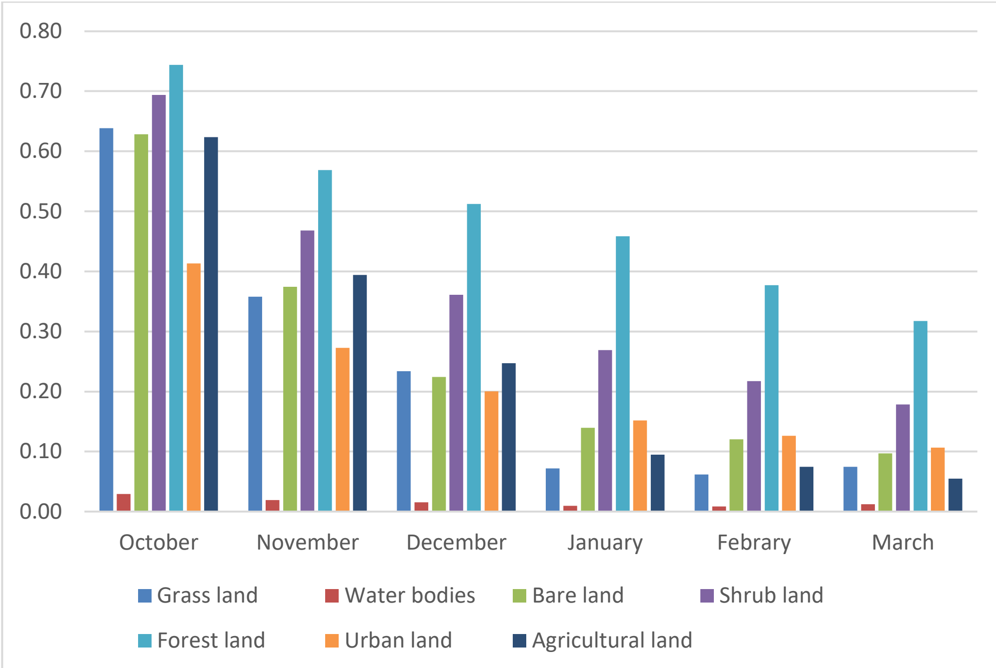

Image 7. 9 Surface temperature Value for deferent land use feature in a given six month (October-march)

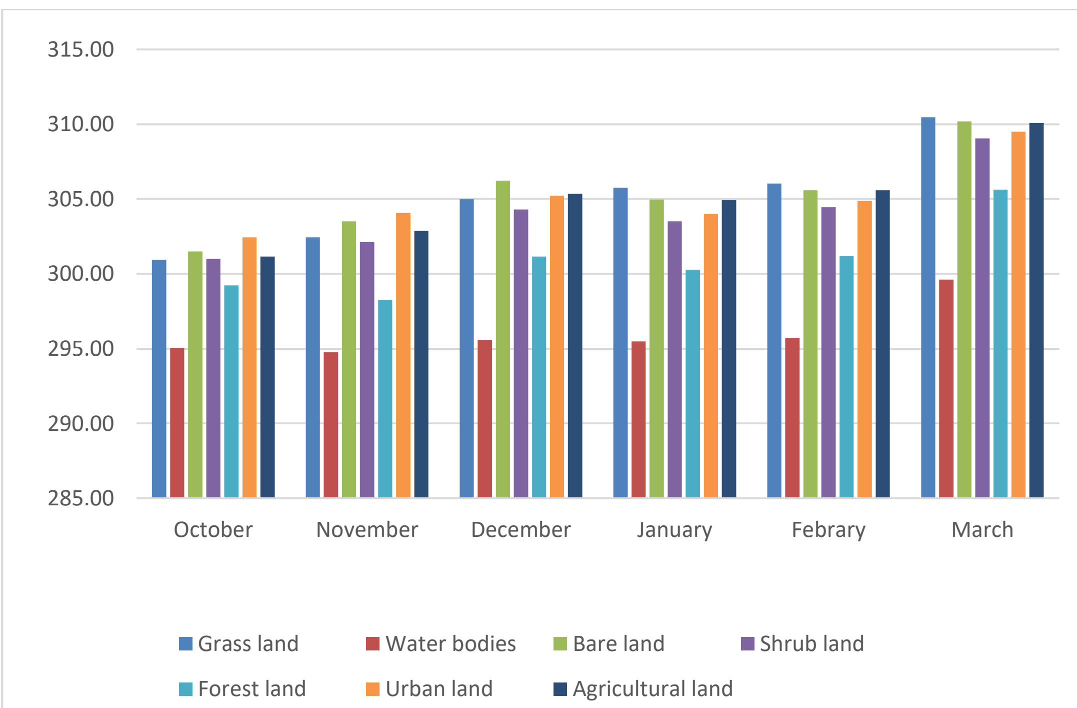

Image 7. 10 Incoming longwave radiation Value for deferent land use feature in a given six month (October-march)

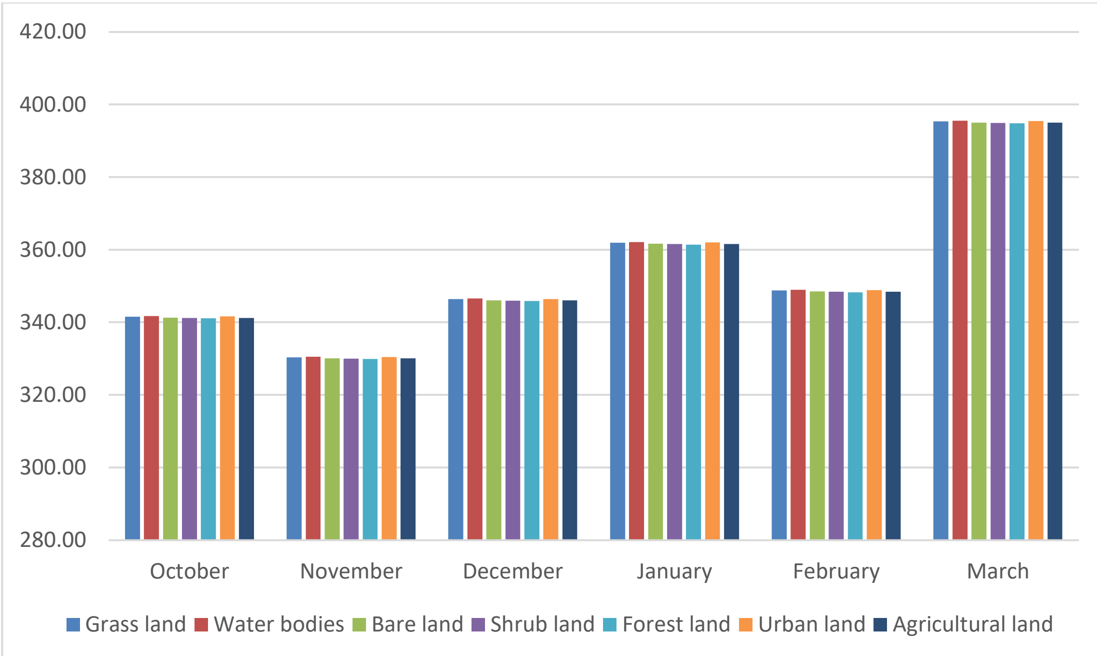

Image 7. 11 Net Radiation Value for deferent land use feature in a given six month (October-march)

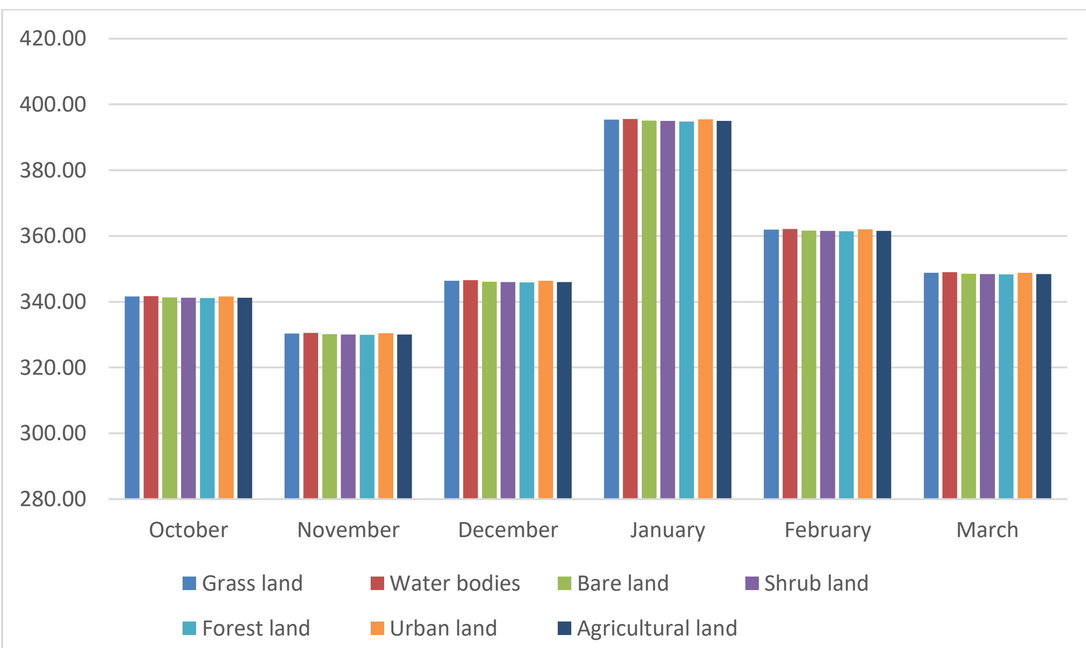

Image 7. 12 Ground heat flux Value for deferent land use feature in a given six month (October-march)

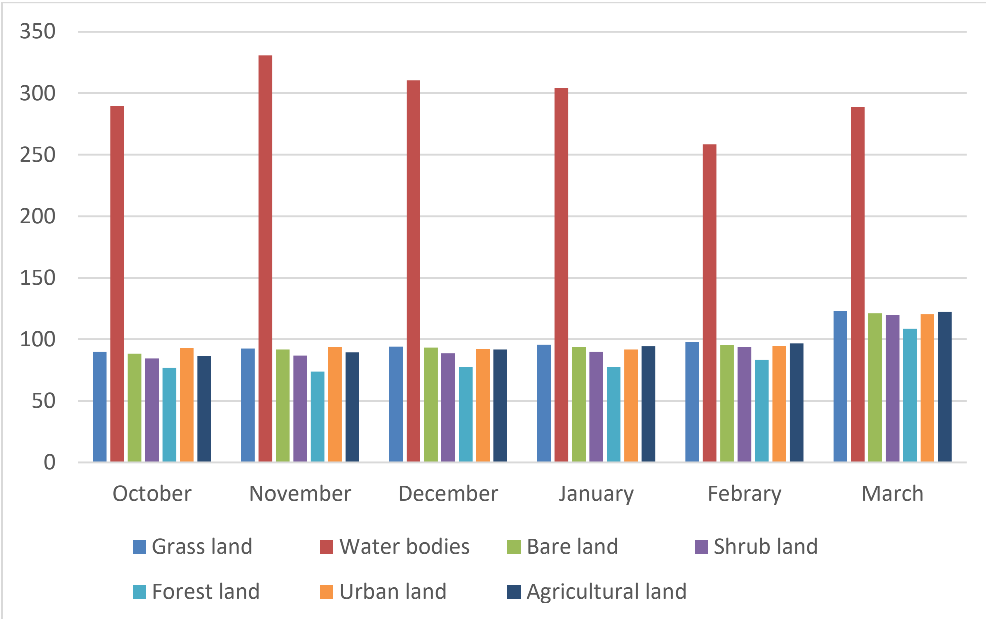

Image 7. 13 Sensible heat flux value for deferent land use feature in a given six month (October-march)

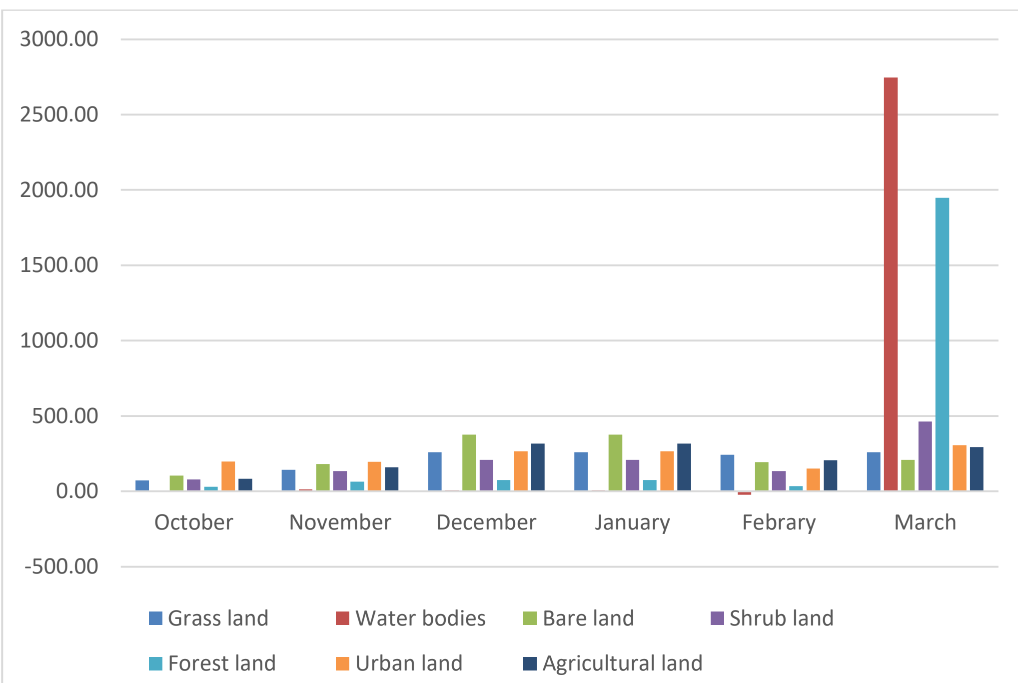

Image 7. 14 Latent heat flux value for deferent land use feature in a given six month (October-march)

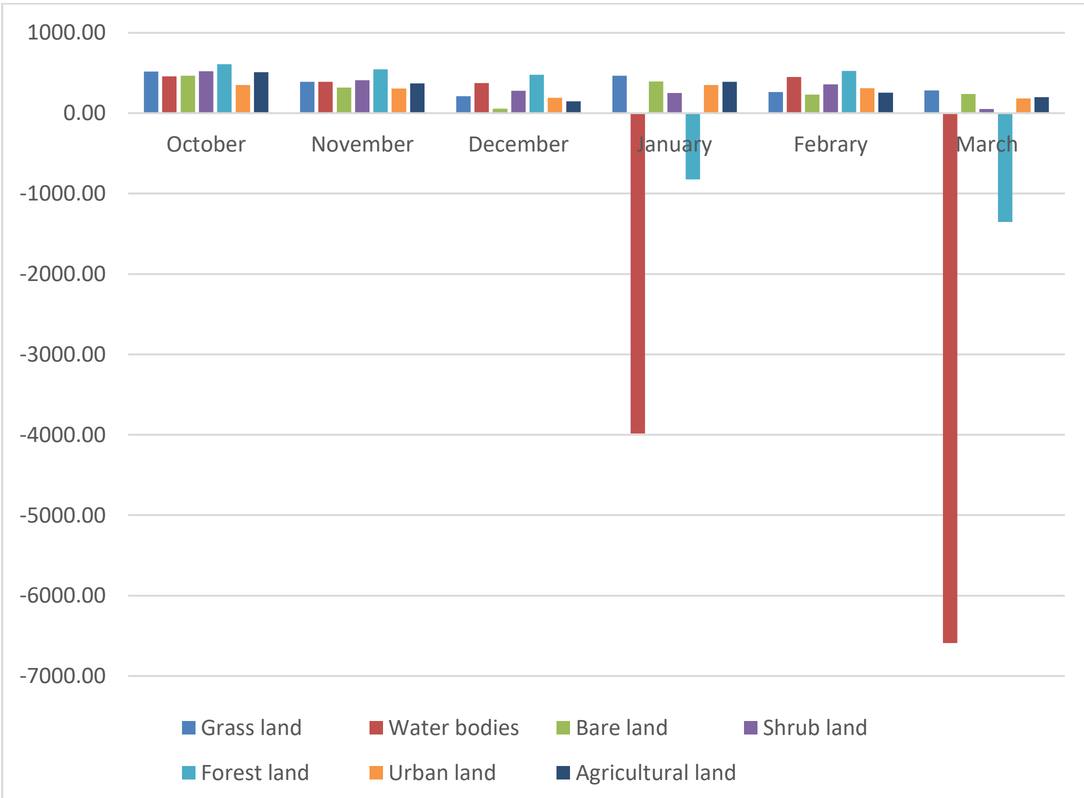

Image 7. 15 Monthly ETa spatial-temporal distribution of 2022 over mojo catchment

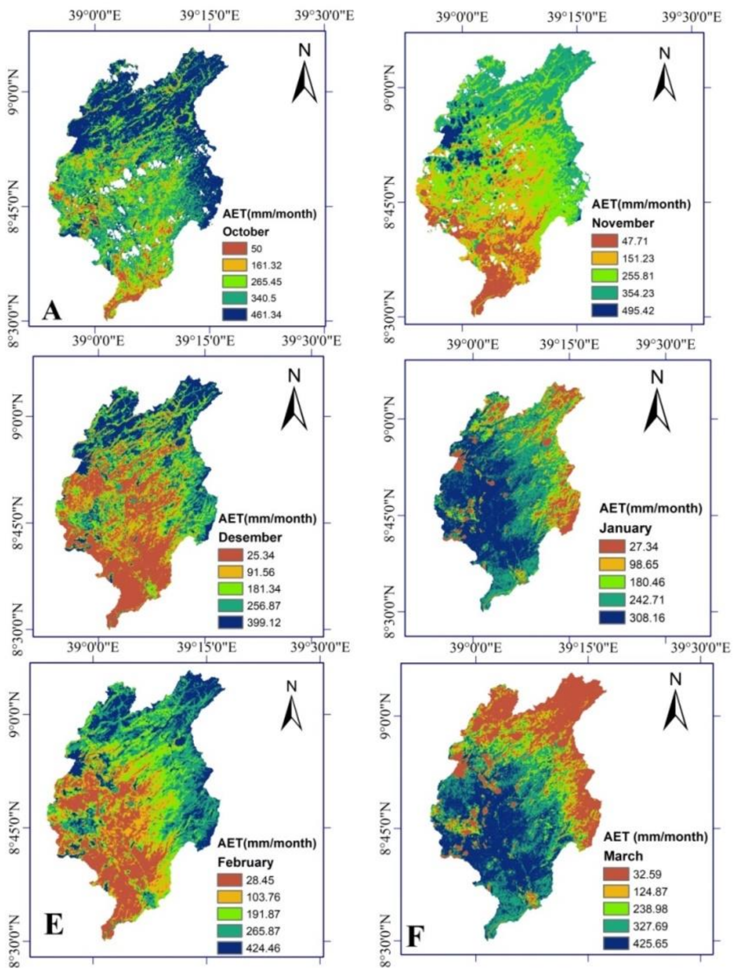

Table7. 3 Mean monthly ETa spatial-temporal distribution of 2022 over mojo catchment

CLASS_NAME	October	November	December	January	February	March
Grass land	325.60	248.64	153.99	267.63	173.41	311.78
Water bodies	293.99	249.55	233.44	30.28	283.03	65.14
Bare land	298.99	208.91	101.84	223.14	154.60	236.09
Shrub land	328.90	262.76	191.64	196.88	227.03	217.14
Forest land	382.64	346.74	297.33	111.08	331.03	114.87
Urban land	238.87	199.92	150.22	208.90	200.59	219.18
Agricultural land	323.52	240.47	148.95	225.13	171.34	241.73

Table7**. 4** Values obtained from SEBAL model of the mojo catchment in 2022

Image date	NDVI	LAI	Albedo	Ts (^{0}C)	RN (W/m2)	H (W/m2)	G (W/m2)	λET (W/m2)	ETrF	ET24 (mm/day)
Oct23	0.51	0.62	0.16	28.15	677.3	88.86	87.83	500.60	2.33	4.99
Nov08	0.40	0.39	0.18	29.73	618.9	17.04	590.9	370.72	1.63	4.26
Dec10	0.32	0.26	0.20	32.13	557.	296.96	92.57	167.71	1.08	4.63
Jan24	0.24	0.13	0.22	31.57	569.5	157.94	94.42	317.18	1.53	5.01
Feb09	0.22	0.11	0.21	32.26	562.2	189.98	96.80	275.37	1.15	5.91
Mar13	0.20	0.08	0.22	36.72	617.8	389.39	122.6	105.73	1.26	6.43